

Nanoscale Torsional Optomechanics

by

Paul Ho-Choong Kim

A thesis submitted in partial fulfillment of the requirements for the degree of

Master of Science

Department of Physics

University of Alberta

©Paul Ho-Choong Kim, 2014

Abstract

Torsional oscillators are well known for their extensive applications ranging from measuring gravity to detecting angular momentum of light. When these torsional resonators scale down, through advanced nanofabrication techniques, the applications extend to measuring quantum effects such as the superfluidity in ^4He film and Casimir forces. The benefits of torsional resonators will only increase with smaller structures, provided that they are supplied with a sensitive detection mechanism. The popular choice of interferometric scheme, for example, does not scale down well with nanoscale on-chip devices and requires a separate detection platform.

Fortunately, there have been recent successes in on-chip cavity optomechanics where the mechanics can be sensitively measured through a high quality optical resonator. By increasing the coupling between the mechanical oscillator and the optical cavity, mechanical detection can be highly enhanced while the device is miniaturized. I have implemented, for the first time, an optomechanical platform using an optical microdisk evanescently coupled to torsional oscillators to demonstrate high torque sensitivities. The results have shown that optomechanics is highly desirable for nanoscale torsion devices opening doors for vast applications: we have achieved angular displacement sensitivity of $4 \text{ nrad}/\sqrt{\text{Hz}}$, displacement sensitivity of $7 \text{ fm}/\sqrt{\text{Hz}}$, and torque sensitivity of $0.8 \text{ zNm}/\sqrt{\text{Hz}}$.

To obtain high-quality silicon-on-insulator microdisks with gaps in the order of $\sim 100 \text{ nm}$, we have chosen a commercial foundry to fabricate our sensitive devices which uses state-of-the-art photolithography procedures. The benefit of deep UV optical lithography is that

many chips on a single 8-inch wafer are available that are cost-efficient over the electron beam lithography method. This thesis highlights the custom made optomechanical apparatus using a dimpled tapered fibre to sensitively probe commercially fabricated torsional devices, demonstrating the compatibility of optomechanics to nanoscale torsional platforms.

Preface

I was with Dr. John Davis since he started his lab in the Fall of 2010 when I was a fourth year undergraduate mature student, recently married, and had a young child. His offer to let me work in his lab was one of the highlights of my life. I have learned much and contributed much since the past three years. From the beginning, our group wasted no time in concentrating on an optomechanical platform, which was a recent trend in sensors for on-chip devices. I was instrumental in five main areas for my masters project: designing optomechanical devices using a commercial foundry (Chapter 2), post-processing nanofabricated chips (Chapter 2, Appendix C), building an optomechanical chamber (Chapter 3), fabricating dimpled tapered fibres (Chapter 3), and constructing the low-temperature optomechanical apparatus (Chapter 5).

Being new in this field, our group first considered the option of using a foundry to fabricate sensitive optomechanical devices that require sub-micron features. With three other collaborating groups, I led the designing processes for each year to collect all the GDS files and ensure that they were error-free from the design rules and that they all fit within the design areas. As a result, these optomechanical torsional designs were highly successful in demonstrating higher sensitivity over the previous work by Dr. Davis, resulting in a publication in APL. Portions of this thesis were taken from my published work, “Nanoscale Torsional Optomechanics,” *Applied Physics Letters*, 102(5): 053102, 2013. Other designs on the same chip were also published with the cantilever-based structure by Doolin *et al*, “Multidimensional optomechanical cantilevers for high-frequency force sensing,” *New Journal of Physics*, 16(3), 035001, 2014 - where I assisted in taking the measurements. From the

same design, nonlinear second-order coupling was observed and submitted by Doolin *et al*, “Nonlinear optomechanics in the stationary regime”, arXiv:1402.3596. I am now working on cleanroom recipes to fabricate sensitive optomechanical structures myself.

The most significant time was spent on optimizing the dimpling procedure of tapered fibres. Although the dimpled fibre was first developed by the Painter group in 2007, the methodology was not widely known. I worked on it for six months to optimize this process, and now can consistently reproduce dimpled tapered fibres whenever I need them. The procedure for dimpling was added to a recent technical paper published in EPJ by Hauer *et al*, “On-chip cavity optomechanical coupling,” *EPJ Techniques and Instrumentation*, 1:4, 2014. In addition to the dimpling procedure, I have designed and custom-machined various parts of our lab’s first optomechanical chamber which was also included in the technical paper. Recently, I have been heavily involved in constructing low-temperature optomechanical apparatus in a dilution refrigerator.

It was hard at times to balance my family time to accommodate my desire for physics research. However, I did work hard during the two years of my masters project and it has been very fruitful. The overall progress accelerated during the two years by working as a team, where I was happy to do my part to keep the momentum. This thesis summarizes my efforts and centres around my first published paper on torsional optomechanics, which was highlighted in an article by nature, “Measuring Twist with Light”, *Nature*, 494, 151, 2013.

To my dear wife Starlayne and my lovely children Hannah and Paul-Anthony.

A moment of Academic History

Zeno's Thesis' Paradox

Around 465 BC, a young Zeno of Elea formulated this paradox in response to interactions with his advisor, Parmenides:

"If for every n number of errors you correct on your thesis, your Professor discovers $n/2$ number of new errors, the number of revisions reaches infinity."

Timeline illustrating the paradox:

- You correct n errors
- Your advisor discovers $n/2$ new errors
- You correct $n/2$ errors
- Your Advisor discovers $n/4$ new errors
- You correct $n/4$ errors...
- Your Advisor discovers $n/8$ errors...
- ∞
- You will never graduate.
- Publish

Back then, they used real blood as ink.

JORGE CHAN © 2013

WWW.PHDCOMICS.COM

Acknowledgements

I am greatly indebted to my supervisor, Dr. John Davis for his kind and endless support during my graduate studies. I consider Dr. Davis my greatest academic mentor from during three years I have known him. His unusual optimism, unique vision, and unfaltering dedication helped me to stay motivated during the three years. It is my hope and desire to steadfastly contribute as much as I am capable of to keep the momentum of our work. Dr. Davis has created a lab environment where we truly work as a team, helping and lifting each other without any form of competition. His leadership certainly attracted many students where I foresee great experiments and projects to flow unceasingly. There are many great things to say about this man of stature but the best thing I learned was how to be an experimentalist. Dr. Davis is the best experimentalist I know, and I want to follow his footsteps to be a great researcher. I look forward to getting my Ph.D. degree with him and to focus my research in low-temperatures.

I appreciate my colleagues, my true friends, that helped me along the path. They are all worthy of admiration for their strong dedication, deep knowledge, and amazing skills. I firstly acknowledge our optomechanics team: Callum Doolin, Bradley Hauer, Allison MacDonald, and Hugh Ramp, where we worked together as a team. I specifically thank Callum for his programming skills that made a lot of our procedure possible in a click of a button, Bradley for the theoretical work on calibrating the data, Allison for her deep knowledge in optics, and Hugh for his quantum-mindedness. I would also like to thank Tushar Biswas for his helpful knowledge and experience in nanofabrication techniques, Abdul Suhel for experimental tips and being my lab neighbour, Dr. Xavier Rojas and Yikai Yang for their expertise in low temperatures, and all the summer students who brought their ambition and dedication to our lab.

Special thanks go to our collaborators, Dr. Mark Freeman, Dr. Paul Barclay, and Dr. Wayne Hiebert, for their helpful insights and inputs during the experiment. Additional thanks goes to my supervisory committee, where they provided thoughtful feedbacks and

comments each year. I would like to thank Greg Popowich, our experienced technical staff, who also contributed much to our lab. He was very helpful whenever we had some issues with the equipment and he always found a way to solve them. The machinists in the physics department as well as the nanofab staff were all incredibly helpful. Although I cannot name them one by one, I truly appreciate all their patience and training.

I have deep-felt appreciation for my parents for their trust and support during my studies. My parents are always interested in my well-being and I could count on them whenever I need extra wisdom and guidance. Equally, my appreciation also goes to my in-laws for their love and support. I express my gratitude to my dear friends and neighbours for their interest in my family and work.

My greatest thanks goes to my family, especially to my eternal love, Starlayne. My dear wife has shown a great example of faith and patience. If it was not for her, I would not have survived during my graduate studies. Taking care of three children, including myself, is not an easy task. I am grateful and will forever cherish our marriage. Thank you for your unconditional love towards me and our children. Thank you Hannah and Paul-Anthony, my beloved children, for your smiles and laughter that lifts my heart. I cherish everyday as I see you grow. I am simply blessed to be surrounded by loving family and wonderful people. Thank you all.

Contents

1	Introduction	1
1.1	Overview of torsion sensors	1
1.2	A brief introduction to cavity optomechanics	3
1.3	Torsional optomechanics	6
2	Post-Processes for Commercially Fabricated Chips	7
2.1	Commercially fabricated on-chip optomechanics	7
2.1.1	Optical resonator designs	10
2.1.2	Mechanical oscillator designs	12
2.2	Post-processing	14
2.2.1	Recipe for piranha cleaning	15
2.2.2	Recipe for photolithography	16
2.2.3	Wet-etching the sacrificial layer, SiO ₂	19
2.2.4	Recipe for drying process without stiction	21
2.2.5	Plasma cleaning	23
3	Experimental Apparatus for Optomechanics	24
3.1	Experimental schematic	25
3.1.1	VOA	27
3.1.2	FPC	27
3.1.3	Microscope objective	27

3.2	Optomechanical vacuum chamber	28
3.2.1	Vacuum parts	28
3.2.2	Electrical ports	30
3.2.3	Fibre through-port	31
3.2.4	Nanopositioning stages	31
3.2.5	Fibre-holder	32
3.2.6	Tapered-fibre apparatus	34
3.3	Dimpled tapered fibres	34
3.3.1	Producing tapered fibres	34
3.3.2	Dimpled fibre procedure	37
4	Experimental results and discussions	41
4.1	Thermomechanical calibration procedure for torsion mechanics	41
4.1.1	Johnson noise	42
4.1.2	Equations of motion	42
4.1.3	Power spectral densities	43
4.1.4	Simulation	46
4.1.4.1	Mode identification	46
4.1.4.2	Moment of Inertia	48
4.1.4.3	Effective constants	49
4.2	Experimental data	50
4.2.1	Optical resonator	52
4.2.2	Optimization of mechanical data	54
4.2.3	Mechanical spectrum for the most sensitive device	56
4.3	Discussion	58
4.3.1	Torque sensitivity	58
4.3.2	Out-of-plane mode	59
4.3.3	Third mode	59

4.3.4	Second order coupling	61
4.3.5	Experimental calculation for G	62
4.3.6	Air data	63
4.4	Smaller moment of inertia devices	63
4.4.1	SEM	63
4.4.2	Simulations and optimizations	64
4.4.3	Best device from the trimmed paddles	66
5	Conclusion and Outlook	68
5.1	Summary	69
5.2	Outlook	69
5.2.1	Exploring other materials for optomechanical systems	70
5.2.2	Upgrades on the apparatus	71
5.2.3	Low temperature apparatus	71
A	Small dimpling procedure	73
B	New optomechanical torsion design	75
C	Deposition	76
C.1	Magnetic nanoparticles	76
C.2	Pt dots	77
C.3	Gold Deposition	78
C.3.1	Post-alignment recipe for EBL	78
C.4	Thermal evaporation for thin film deposition	85

List of Tables

2.1	Inconsistent etch rates obtained using HF vapour from averaging five trials for etch times of one, two, and three minutes.	21
2.2	Various solvents with experimentally measured surface tensions near room temperature (46). The lightest solvent, n-Pentane, was used to dry the chip as an alternative method to avoid stiction	23
4.1	Tabulated experimental results for all nine devices of the torsion paddle with torsion rod length of $\sim 5 \mu\text{m}$	55
5.1	List of Young's modulus for various robust materials (38) and corresponding index of refraction near 1550 nm (77).	70

List of Figures

1.1	Historical examples of torsion sensors and their miniaturization for many applications. The torsion rods were used to determine the a) gravitational constant (1), and the b) quantum plasticity of solid ^4He (6). In addition, c), g) chip-scale torsion sensors allowed sensitive applications such as a torque magnetometer (12), (14), and d) electrometer (15). Further torsional devices were able to detect e) electrical spins (16), and f) observe the Casimir effect (17).	2
1.2	A simple sketch of the Fabry-Pérot optomechanical system (left) with high reflecting mirrors separated by the length L forming an optical resonance coupled to the mechanical spring. The central idea for this project is to develop a torque-based optomechanical system modelled after the angular form of Hooke's law demonstrated on the right.	4
1.3	a) Illustration of optomechanical transduction mechanism where the time-varying signal (inset) occurs at the side of an optical resonance (indicated by a star) due to the cavity length changes from the dynamics of the spring as shown in Fig. 1.2. b) An example of a Fourier transformed data, showing the mechanical peak resonance in the frequency spectrum.	4
1.4	Gallery of developed sensors of various optomechanical platforms. There are WGM-type optomechanical structures designed for a) a force sensor (33), b) a magnetometer (34), and c) an atomic-force-microscope (AFM) (35). Examples of photonic-crystals also provides extensive applications in building d) an accelerometer (32) and e) a small mass ($\sim \text{fg}$) displacement sensor (19).	5
2.1	a) Rendered image of the optomechanical torsion platform. A dimpled tapered fibre couples light into a microdisk WGM resonator, which is evanescently coupled to a mechanical torsion oscillator. b) Basic description of the geometry used for the optomechanical torsional design.	8

2.2	An angled SEM image of a commercially fabricated optomechanical chip, which was post-processed to etch away the buried oxide layer (SiO_2). There are vast number of different optomechanical devices and their parameterizations. The left inset shows a top view illustrating the void space ($100 \mu\text{m} \times 150 \mu\text{m}$) surrounding the device to give enough room for dimpled tapered-fibre alignment. The right inset shows the typical SOI platform where the top layer was $\sim 220 \text{ nm}$ on top of a sacrificial layer (SiO_2) of $2 \mu\text{m}$, suited for photonic devices near 1550 nm	9
2.3	Some of the optomechanical devices in the first-year designs are shown in SEM images with false green colour: a) an optical microdisk coupled to a doubly-clamped beam, b) a slot ring resonator with its cross-section optical mode profile (inset), and c) a racetrack resonator coupled to a torsion device.	11
2.4	Fully released optomechanical torsion devices are shown in SEM micrographs used in this project. a) The first-year batch of torsional designs consist of a simple paddle attached to a torsion rod hanging at the edge of the posts. The bending of the torsion rod is evident where the designed gap of 130 nm got closer to 100 nm after the drying step processed at the cleanroom. b) In the second-year designs, the torsion rods are straighter by introducing an offset from the end-posts ($\sim 1.5 \mu\text{m}$) to enhance the rigidity of the torsion rod supporting trimmed torsion paddles.	12
2.5	Magnified SEM images showing different curvature of the end paddle matching the curvature of the $5 \mu\text{m}$, $10 \mu\text{m}$, and $20 \mu\text{m}$ diameter disks, respectively, from left to right.	13
2.6	The diamond saw at the Nanofab was used to precisely dice the commercially made wafers into individual chips of $1 \text{ cm} \times 1 \text{ cm}$ shown in a). A photograph of the fully post-processed chips prior to the experiment is shown in b) where the left two chips are the first year designs and the right two chips are the second year designs.	13
2.7	a) To maintain a certain uniform etch-density throughout the wafer, tiles are patterned by the foundry in empty spaces (typically outside the design area), presented in the SEM image. b) During the $2 \mu\text{m}$ deep SiO_2 etch process, tiles that are $1.5 \mu\text{m} \times 1.5 \mu\text{m}$ detach completely and land on random areas on a chip - which can damage critical devices.	14
2.8	A full processflow performed at the Nanofab after receiving commercially patterned chips to etch-release mechanical devices while simultaneously mask unwanted structures via photolithography. The main steps include piranha cleaning, optical lithography patterning, and wet-etching the SiO_2 layer.	15
2.9	A zoom-out SEM image of a fully post-processed chip which a photolithography step was included to perserve all the thin ring structures (green inset) while masking all unwanted areas such as tiles (yellow) and other group designs (orange). Both large and small alignment marks are clearly visible in the image where the large alignment mark ($100 \mu\text{m} \times 100 \mu\text{m}$), indicated by the white arrow, was primarily used for alignment during the photolithography step.	16

2.10	Illustrations of two methods for achieving good contact during a photolithography process. A vacuum contact was typically used, seen in a), if the travel range of the chuck can be aligned with the mask. Otherwise a hard contact, shown in b), was used by mounting the chip on a bare silicon wafer utilizing a wafer chuck. The real image of these two mounts are shown in c) and the chromium photomask that was used in d).	18
2.11	Demonstration of SiO ₂ wet-etch on a patterned SOI chip using BOE. The top and the side views of a square and a circular geometries are illustrated in a), where the BOE process removes the sacrificial layer (dark blue) isotropically (SiO ₂) as shown in b). A SEM image of a fully BOE processed device is displayed in c).	19
2.12	a) The HF vapour etcher (Idonus VPE150) at NINT. I have attempted to avoid stiction using this equipment, but the outcome in b) shows an undesirable anisotropic etch in contrast to the wet-etch.	20
2.13	The left figure shows the general phase diagram where the problem of stiction is outlined on the right during the phase change of 2). A strong capillary force from the solution in the small gap attracts the optical and the mechanical devices causing stiction. There are two ways to avoid the stiction problem either by 1) freezing the liquid and applying sublimation or 3) critical drying the liquid to completely bypass the phase change. The latter method is by far more popular and effective.	21
2.14	Straight forward procedure for solvent method to replace the water to a light solvent (n-Pentane) adiabatically to minimize the capillary force.	22
3.1	An overhead layout and a photograph of the optical table shows the optical table consisting the fibre-puller set-up, the CO ₂ laser, and the optomechanical chamber.	24
3.2	Schematic of the experimental setup centred around the optomechanical vacuum chamber (left). The fibre-based system has a dimpled tapered fibre inside the chamber together with the post-processed chip where the alignment is done through the viewport on top using a microscope. The image on the right shows a photograph of the apparatus.	25
3.3	An extruded acrylic fibre-panel installed to display the fibre-based apparatus, which conserves space and provides working area in the floating optical table	26
3.4	An optical bistability, or a non-linear resonance, is observed in a silicon WGM microdisk from the heating effect in silicon for high measurement power. Therefore, a VOA is necessary to adjust the laser power to avoid any non-linearity since the optomechanical transduction comes from the slope of the resonance.	26
3.5	The two necessary components of the dimpled tapered fibre to control the a) power (VOA) and the b) polarization (FPC) are part of the fibre-based apparatus.	27

3.6	a) Zoomed picture of Fig. 3.2 centred on the microscope system showing the glass view-port for imaging. Captured image from the microscope-camera is shown in b), where the dimple region can be clearly located from the out-of-focused region. The scale bar is 100 μm	28
3.7	Rendered image of the arrangement inside the OVC, showing the Attocube stacks (green) and a fibre-holder mounted on I-beam (grey) and goniometer (black).	29
3.8	Pictures of the vacuum system. a) The turbo pump is connected to the chamber via metal bellows but the vibration is quite noticeable. b) Therefore passing through a heavy concrete block damps the vibration caused by the turbo pump.	29
3.9	a) Two electrical ports are displayed, where three adapters were used to power the positioners inside the OVC. The extra adapter, connected with an attenuator in the picture, is wired to a piezo-actuator that is under the chip. b) For the fibre port, there are total eight holes (~ 1 mm diameter) but only two are used for fibre input and output. They are held in place using vacuum compatible epoxy, and covered with heat shrink tubing for stress-relief. . . .	30
3.10	Tapered fibres in a) u-shaped and b) dimpled-shaped structures to approach micron-scale devices on a 2D-chip with three possible methods illustrated below.	32
3.11	a) A CAD illustration of the computer-controlled motorized stage to taper an optical fibre using H_2 torch. b)The setup can also accomodate a microscope to monitor during the dimpling procedure precisely. c),d) Instead of the H_2 torch. the CO_2 laser can also be used to taper and dimple fibres where a ZnSe lens is used to focus the laser.	33
3.12	Different kinds of tips for a hydrogen torch are shown in a), where the single hole torch tip (OX-0), circled in orange, was mainly used for tapering the fibre. The graph in b) shows the typical tapering profile to reach single mode in using the OX-0 stub.	35
3.13	The overview of the dimpling process. First, the centre of the thinnest part of the taper is located in a) by retracting the clamps and the mould is positioned directly under it. Raising the mould while retracting the clamps is shown in b) where the bottom inset shows the ideal configuration for annealing. In c) I used a small flame upside down to mould the tapered fibre. After lowering the mould while simultaneously tensioning the fibre, the mould is brought to a point levelled with the rest of the tapered fibre. To release the mould from the tapered fibre, a small hydrogen flow from the torch was used. The mounting is depicted in e) where 5-minute epoxy was applied to attach the fibre to the fibre-holder. During the entire dimple process, the transmission was monitored in f) where 92 % was recovered after the dimple.	36

3.14	Zoomed picture of Fig. 3.11b. The setup in a) includes a dimple mould, or a cleaned stripped fibre, taped orthogonally to the tapered fibre. Raising this mould using manual positioner while detensioning the tapered fibre results in b) (with a scale bar of $125 \mu\text{m}$). Using a small flame, from the HT-1 torch-tip, the annealing process is done by dabbing the mould manually with a flame for 1 second as shown in c) and Fig. 3.13c.	37
3.15	a) Rendered image of the gluing process with the 5-minute epoxy applied on the fibre-holder placed upside down. The inset show the top-view of the fibre-clamps, fibre-holder, and the dimpled tapered fibre in a simplified manner. Monitoring in real-time, the fibre-holder was raised until the epoxy touched the tapered fibre as shown in b) and c) [47].	38
3.16	Image of the fully fusion spliced dimpled fibre assembled together with the commercially made chip awaiting pumping and optomechanical measurement.	39
4.1	Raw data for the mechanical frequency spectrum observed for a torsional device using the optomechanical transduction obtained at the side of the optical resonance.	44
4.2	The first four eigenmodes of the torsion paddle system simulated from COM-SOL with a) out-of-plane torsional mode, b) flexural mode, c) in-plane torsional mode, and d) in-plane mode with frequencies of 9.04 MHz, 13.62 MHz, 17.40 MHz, and 17.72 MHz respectively.	47
4.3	a) SEM images of the fabricated devices with $5 \mu\text{m}$ (purple), $10 \mu\text{m}$ (green), and $20 \mu\text{m}$ (red) diameter disks. b) The predicted frequencies calculated through FEM (dashed lines) and measured frequencies (markers, solid lines are linear fits) of devices with varying sized optical disks are plotted against the change in moment of inertia calculated from the modelled geometries.	48
4.4	Based on the eigenfrequency and moment of inertia simulations, the peaks in Fig. 4.1 are identified as the torsional mode (left) and the flexural mode (right).	49
4.5	FEM simulations used to apply a torque to find the effective torsion spring constant. a) The edge load of $\pm F/2$ was applied at opposite ends of the paddle, b) resulting in a torque.	49
4.6	The data from the lock-in technique, where the wavelength is scanned over the whole tunable range ($1550 \text{ nm} \sim 1630 \text{ nm}$), with optical resonances shown as a dip in the transmission (orange) while the fundamental mechanical frequency is locked near 9 MHz with 100 Hz bandwidth (black). The optical data were normalized to the background scan (without coupling). The three plots correspond to a) $5 \mu\text{m}$, b) $10 \mu\text{m}$, c) and $20 \mu\text{m}$ diameter disks coupled to torsional oscillators with the smallest gap of $\sim 130 \text{ nm}$. During the measurement, the dimpled tapered fibre was touching the optical disk.	51

4.7	Three devices, each with a 10 μm diameter disk but with varying gaps between the disk and the mechanical structure, show the variation of the optical resonance near 1577 nm. The red resonance is the smallest gap (100 nm) with Q_{opt} of 19,990, yellow having gap of 180 nm with Q_{opt} of 25,500, and green resonance having the largest gap (230 nm) having 37,780. Therefore we conclude that an increase in the gap between the optical and the mechanical resonator increases the Q_{opt} .	52
4.8	SEM micrograph of the optomechanical torsion designs overlaid with a simulation of the optical mode showing evanescent coupling between the two oscillators (optical and mechanical).	53
4.9	Fine wavelength scan (orange) of the optimized optical resonance near 1577 nm based on Fig. 4.6b. The numerically calculated slope (lavender) of the optical resonance qualitatively agrees well with the locked mechanical amplitudes (black).	54
4.10	Comprehensive plots for all nine optomechanical torsion devices presented to show a trend in a) optical disk diameter and the b) gap between the optical cavity and torsional oscillator. Lines are guides to the eye and trends are explained in the text.	56
4.11	a) Calibrated plot of the most sensitive torsional mode (9.04 MHz) from the 10 μm diameter microdisk resonator coupled to the torsion paddle with 100 nm gap. The calibrated noise-floor obtained from the fit parameter (S_v^{nf}) translates to linear displacement sensitivity (S_z^{nf}) of 7 fm/ $\sqrt{\text{Hz}}$ and corresponding angular sensitivity (S_θ^{nf}) of 4 nrad/ $\sqrt{\text{Hz}}$ (36). b) Taken at a later date, plotting the same device but scanning at a wider frequency range confirms that the noise-floor does reach the calibrated values.	57
4.12	Torque sensitivity plot where S_τ was minimum near the torsional resonance.	58
4.13	The experimental apparatus in a) (56) was used to test the out-of-plane actuation. These mechanical peaks were not thermally resolved, where small peaks only start to appear with piezo-buzzer driving at 10 mV (light green). The dark green in b) is driven at 100 mV and the corresponding phase is observed in c) showing the efficient driven mode at 9.3 MHz in contrast to the 9 MHz peak.	60
4.14	The third peak (suspected in-plane mode) appearing near 12 MHz on a linear scale for the 10 μm diameter disk with 100 nm gap.	61
4.15	a) Optical FEM simulation of the straight side wall and its uniform field for second order coupling. b) An angled image of the optomechanical torsion design with sidewall angles of 10 degrees from vertical.	61
4.16	The plot is similar to Fig. 4.9 where orange is the optical transmission showing the cavity resonance but plotted against optical frequencies to determine the slope ($\Delta V/\Delta\omega$) at the location of the highest mechanical amplitude of a torsional mode (black). This slope is found by a linear fit (purple line) and is an important quantity to determine the experimental G based on the optomechanical transduction mechanism tuned at the side of an optical resonance.	62

4.17	Thermally resolved raw data for the optimized torsional device in air with Q_{mech} of 150.	63
4.18	SEM images of three small mass torsion paddles with increasing coupling length towards the right (0.13 μm , 1 μm , and 2 μm , respectively).	64
4.19	From the skinny torsion paddle structure (T677), one major torsional peak was observed near 8 MHz. Other mechanical resonances have very small amplitudes due to the asymmetry in the torsion paddle where the weight is primarily on one end.	64
4.20	FEM simulations of the T677 device showing some of the structural modes in a) 6.61 MHz, b) 17.97 MHz, c) 20.61 MHz, and d) 27.64 MHz. Due to the added mass on the paddle close to the microdisk, it has smaller mechanical amplitudes for modes b), c), and d), compared to the torsional mode a). From the experimental data, shown in Fig. 4.19, a single large torsion peak near 8 MHz was observed.	65
4.21	The change in the moment of inertia plotted for the three different devices in Fig. 4.18 where the drastic changes in the moment of inertia was observed compared to Fig. 4.3. The simulation (hollow squares) agrees well qualitatively with the experimental data (solid red squares). Lines are guides to the eye.	66
4.22	Optimization process to maximize the peak mechanical amplitude at 7.85 MHz (the torsional mode), where the optical resonance near 1587 nm was used.	67
4.23	The frequency spectrum of the device T677 of the torsional mode in log scale. This device is slightly better in sensitivity compared to the C10 device but has lower Q_{mech} of 625.	67
5.1	A photograph of our current progress with the low-temperature optomechanical apparatus. The components are similar as the room temperature OVC where a microscope, nanopositioning stages, and a fibre holder are present.	72
A.1	The same procedure from Section 3.3 was used to produce smaller dimpled tapered fibres where a half-tapered fibre is used as a mould with diameter $\sim 65 \mu\text{m}$. a) The typical tapering profile with 78 % efficiency down to a single mode fibre near 1 μm in diameter. b) After the dimple procedure, the transmission was recovered (99.5 %) where the optical image of a fully fabricated tapered fibre is shown in c).	74
B.1	An example of a possible design for the next generation of torsional device. The gaps are drastically reduced to $\sim 35 \text{ nm}$ and the coupling length are increased by a triangular paddle to increase G . The holes are inserted to reduce the mass of the torsion device and the device is highly symmetric. This design is currently used to optimize the recipes for EBL patterning and plasma etching (ICP-RIE).	75

C.1	Depositing small magnetic nano-particles (maghemite) on the chip using the pick-and-place method in the fibre-puller setup. The spot on the letter A (right) shows the deposited particle, placed from the tip of the tapered fibre. Due to a floppy tapered fibre, I was not able to aim and deposit precisely. The scale-bar is 10 μm	76
C.2	a) Exposure test of Pt dot depositions with varying exposures from 1 to 9 seconds. b) Throughout the devices we have exposed ~ 4 seconds on each dots giving dots of ~ 100 nm in size.	77
C.3	Successful patterned gold film (~ 15 nm thickness) deposited on the paddles as shown in a) and b) with smallest feature size of ~ 80 nm in b).	78
C.4	Post-alignment includes aligning all three different coordinate systems in the equipment. The stage movement (X, Y) should first be aligned with the design coordinates (U, V) (coarse alignment) and the electron beam should be adjusted (fine alignment) to account for the actual coordinates in a real chip (u, v).	79
C.5	Illustration of the bilayer structure of PMMA. The lighter PMMA 495k is underneath the heavier PMMA exposing more with the same dose, where it creates a nice contact-less window compared to the single layer case. Bilayer method is required for very thin layer or a small feature size.	80
C.6	A layout of the IMEC chip where the green area is the location of optomechanical torsional devices. Based the alignment marks as shown in a), a separate layer (63) having eight rectangles inside the $100 \mu\text{m} \times 100 \mu\text{m}$ write-field box was prepared to do fine-alignment as shown in b). Coarse alignments were done by a 3-point alignment, where the origin in c) and the other two alignment marks (marked by arrows in the layout) were used. I have made patterns on torsional paddles as shown in gold colour (layer 92) with an example demonstrated in d). Note in a), a gold box in the corner was also patterned to confirm how well the alignment was done after the exposure of bi-layer PMMA.	81
C.7	A high-vacuum evaporator system located at the thin film lab (UAlberta). a) A photograph of the bell jar used for thermal deposition of chrome and gold. Some of the components are displayed such as b) an electrical contact used to pass high-current to heat the deposition material and c) valves used to pump out the bell jar using a diffusion pump.	86

List of Abbreviations

BOE	Buffered-oxide etch	14
CMOS	Complementary metal-oxide-semiconductor	7
DAQ	Data-acquisition	25
EBL	Electron beam lithography	7
FEM	Finite-element method	41
FIB	Focused ion beam	77
FPC	Fibre polarization controller	25
HMDS	Hexamethyldisilazane	15
HSQ	Hydrogen silsesquioxane	70
LIGO	Laser interferometer gravitational-wave observatory	3
NEMS	Nanoelectromechanical systems	2
OVC	Optomechanical vacuum chamber	25
PD	Photodetector	25
PDH	Pound-Drever-Hall	71
PMMA	Polymethyl methacrylate	79
PSD	Power spectral density	43
SEM	Scanning electron micrograph	10
SOI	Silicon-on-insulator	8
SQL	Standard quantum limit	3
VOA	Variable optical attenuator	25
WGM	Whispering-gallery-mode	5

CHAPTER 1

Introduction

There's no such thing as small science, only small scientists.

-Cloudy with a chance of meatballs 2

1.1 Overview of torsion sensors

Torsional mechanical oscillators, modelled after the angular form of Hooke's law,

$$\tau = \kappa\theta \tag{1.1}$$

are typically designed to have small torsional spring constants (κ) in order to observe small torques (τ). These small torques can be easily related to fundamental physics that make it desirable for researchers to use these types of devices. Starting with the famous Cavendish experiment, torsion rods were used to measure an accurate value for the gravitational constant (1) and the constant was further refined using a similar but improved apparatus (2). They are even used as galactic-models to test the equivalence principle using a rotating torsion balance (3). In contrast, extremely small angular momentum of light was detected by a set of torsion paddles (4). Moreover, torsion rods were used in low temperature experiments to investigate the superfluid transition in ^4He films (5) and attempted to discover a new phase of supersolidity in ^4He (6).

Magnetic systems are especially entwined with torque measurements where sensitive magnetometers were built based on torsional oscillators (7), (8). The de Haas - van Alphen effect was observed using a torsion balance, where the magnetic moments in a pure metal oscillates with applied magnetic field (9). This quantum effect, sensitive to temperature, was applied

in cryogenic systems to accurately read temperatures below 1 K (10). The Barkhausen effect, or the magnetization jumps occurring in ferromagnetic systems, were also reported and controlled in a torsion paddle platform fabricated on a silicon nitride chip (11).

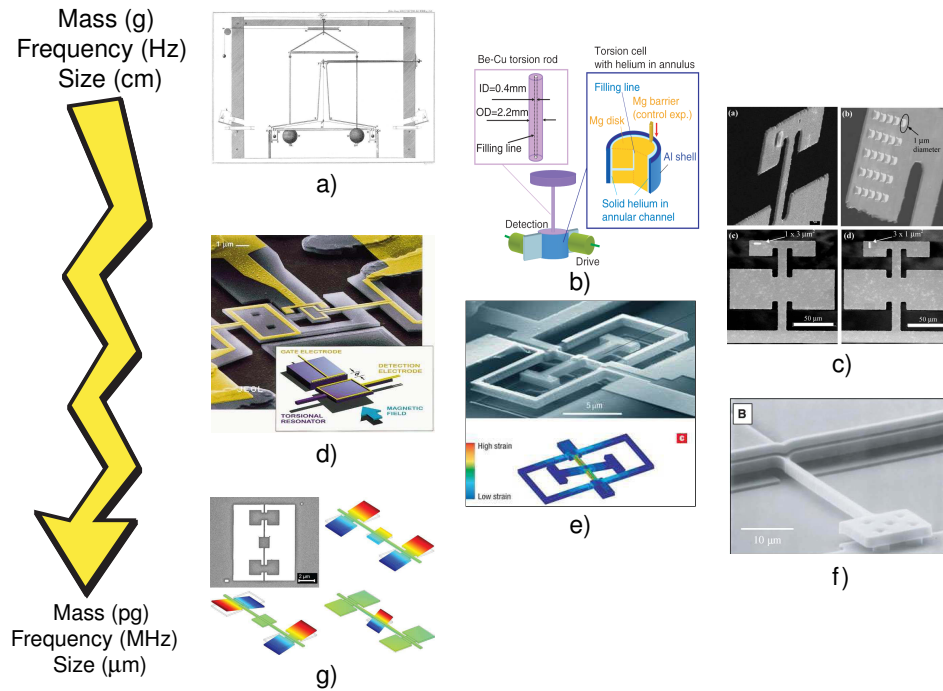


Figure 1.1: Historical examples of torsion sensors and their miniaturization for many applications. The torsion rods were used to determine the a) gravitational constant (1), and the b) quantum plasticity of solid ^4He (6). In addition, c), g) chip-scale torsion sensors allowed sensitive applications such as a torque magnetometer (12), (14), and d) electrometer (15). Further torsional devices were able to detect e) electrical spins (16), and f) observe the Casimir effect (17).

As with other nanoelectromechanical systems (NEMS), these torsional devices have been scaled down to be more sensitive to their nanoscale environment. Fig. 1.1 illustrates the decrease in the mass of torque sensors made possible by rapidly developing nanofabrication technology. On-chip torsion devices have been utilized to inspect nanoscale magnetic properties (13),(14), to build an effective electrometer (15), to measure electron spin flips (16), and to detect Casimir forces (17). The torsional devices are constantly being challenged and improved by reducing the mass further based on the available nanofabrication techniques where the quantum mechanical phenomena could be more accessible.

However the technology to miniaturize torsion-based system is only half of the story, which becomes complete if and only if the device is complemented with a highly sensitive detection scheme. Torsional devices were historically measured via interferometry (18), direct measurements of the laser deflecting off of highly-reflective surfaces (3), or capacitive measurements on metal-deposited paddles (15). All of these conventional methods are undoubtedly sensitive, however they do not scale down well with sizes smaller than the laser beam spot size ($< 1 \mu\text{m}$) or require added complexity in the circuit to minimize the electrical noise. With the available fabrication techniques, I have been exploring ways to improve sensitivity while reducing the size of these torsional oscillators in a simplified manner. Cavity optomechanics has recently demonstrated extremely high sensitivities for on-chip devices (19)-(21), and therefore became my primary focus to implement optomechanics to torsional resonators.

1.2 A brief introduction to cavity optomechanics

One of the prime examples of optomechanical displacement sensors is the laser interferometer gravitational-wave observatory (LIGO) where displacement sensitivities on the order of $\sim 10^{-19}\text{m}/\sqrt{\text{Hz}}$ were achieved for the mirror near 100 Hz by engineering the Fabry-Pérot cavity (22). These unprecedented sensitivities were ultimately limited by the shot noise at low laser power, arising from the fluctuations of the electrons in the detector, and the radiation pressure noise at high laser power, induced by the fluctuations in the photon flux to the mirrors. These limitations define the standard quantum limit (SQL), or Heisenberg limit, where the sensor is now faced with the quantum nature of light making it harder to go beyond the atto-metre scale sensitivities. More recently squeezed states of light were implemented, where one quadrature of light is squeezed from passing through a nonlinear crystal (PPKTP crystal), to improve the sensitivity in the same quadrature by 2.15 dB (23). Shrinking this sensitive gravitational wave detector to fit on an optical table has also been successful to reach sensitivities below the shot noise using the squeezed states of light (24).

Inspired by the principles of cavity optomechanics - demonstrated from the quantum-limited gravitational wave detectors, a natural progression towards on-chip scale detection was desirous to probe other nanoscale phenomena with equivalent sensitivities. In early 2005, it was shown that on-chip toroidal resonators, intrinsically having a high optical quality factor (Q_{opt}), possess mechanical breathing mode that is highly-coupled to the optical mode, and thus demonstrate high sensitivity to displacement of $\sim 10^{-17} \text{ m}/\sqrt{\text{Hz}}$ (25), (26). Since then vast number of different optomechanical cavity systems have been flourished, demonstrating the powerful transduction scheme for on-chip devices where squeezed light

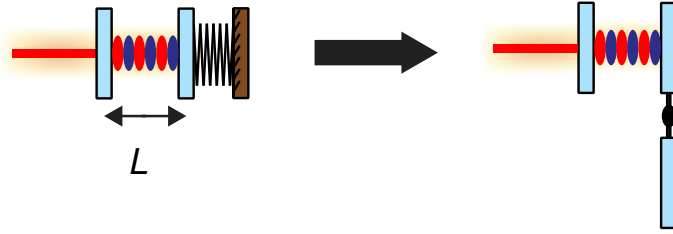


Figure 1.2: A simple sketch of the Fabry-Pérot optomechanical system (left) with high reflecting mirrors separated by the length L forming an optical resonance coupled to the mechanical spring. The central idea for this project is to develop a torque-based optomechanical system modelled after the angular form of Hooke's law demonstrated on the right.

were also recently implemented (27),(28). It is remarkable that on-chip pico- and femto-gram scale devices can also have sensitivities comparable to the diameter of a proton (~ 1.6 fm) by utilizing the coupling between the optical cavity and the mechanical resonators.

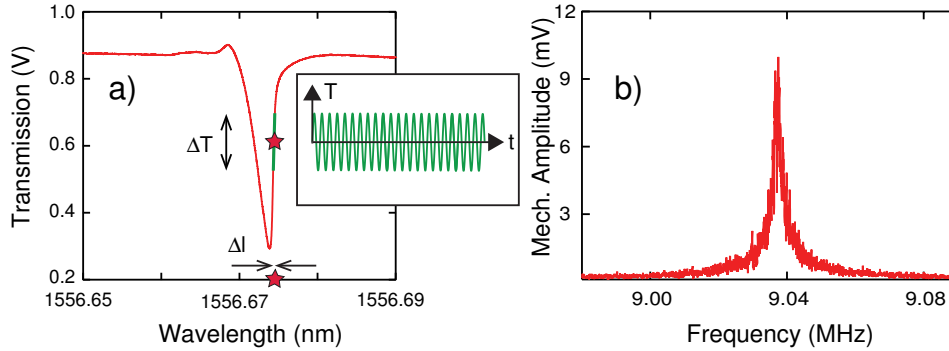


Figure 1.3: a) Illustration of optomechanical transduction mechanism where the time-varying signal (inset) occurs at the side of an optical resonance (indicated by a star) due to the cavity length changes from the dynamics of the spring as shown in Fig. 1.2. b) An example of a Fourier transformed data, showing the mechanical peak resonance in the frequency spectrum.

The demonstration of optomechanics can be done by a simple illustration with the Fabry-Pérot cavity with two high-reflecting mirrors separated by length, L , where one mirror is fixed and the other is connected to a spring (See Fig. 1.2). Fixing the wavelength at the side of the optical resonance (marked by the star in Fig. 1.3a), any optical resonance shifts will result in a time-varying signal where the dynamics of the spring are encoded. Applying the Fourier transform, mechanical frequency spectrum of the moving mirror can be attained

(Fig. 1.3b). The coupling between the moving mirror and the optical resonance is therefore described via G , the optomechanical coupling coefficient, by the following equation:

$$\omega(z_0 + z) = \omega(z_0) + Gz \quad (1.2)$$

$$G = \frac{\partial\omega(z_0)}{\partial z} \quad (1.3)$$

where $\omega(z_0 + z)$ is the shifted optical frequency from the cavity resonance, $\omega(z_0)$, due to a coupled small mechanical displacement z . Therefore G is defined as the change in the optical frequency per mechanical displacement in units of (Hz/m) in which for a simple Fabry-Pérot system, it can be expressed as ω_0/L where ω_0 is the optical resonance frequency (29). Similarly, whispering-gallery-mode (WGM) cavities have G expressed as ω_0/R for the radial breathing mechanical displacement where R is the radius of the cavity. However more simulations and experiments may be required to obtain the G for different complex geometries (30), (31).

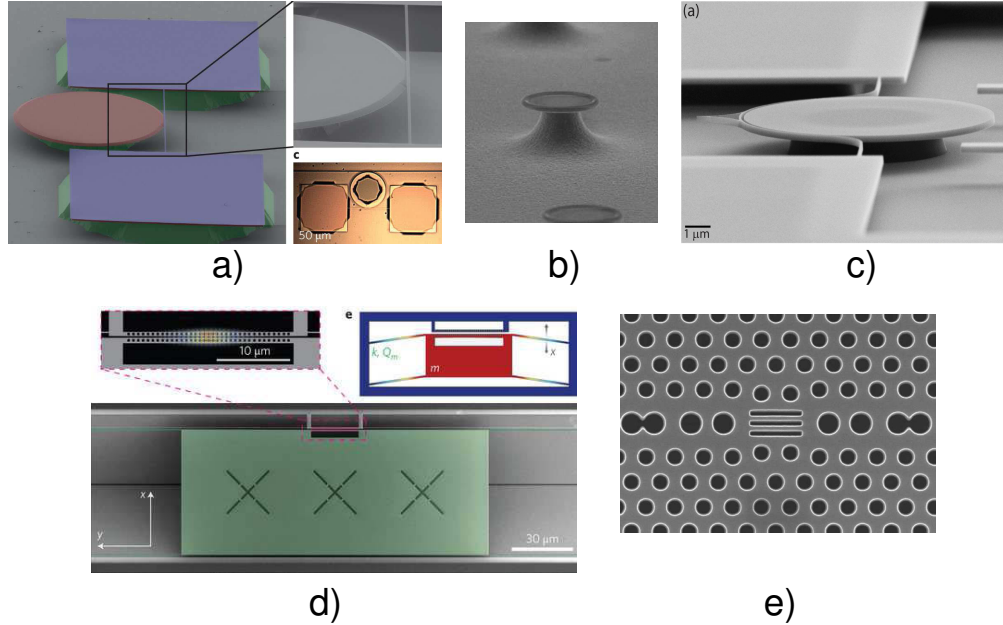


Figure 1.4: Gallery of developed sensors of various optomechanical platforms. There are WGM-type optomechanical structures designed for a) a force sensor (33), b) a magnetometer (34), and c) an atomic-force-microscope (AFM) (35). Examples of photonic-crystals also provides extensive applications in building d) an accelerometer (32) and e) a small mass (\sim fg) displacement sensor (19).

A large G , or large optical resonance shifts, in a Fabry-Pérot cavity is desired for high sensitivity - which in general L should be small. However, the cavity length cannot be infinitesimally small because of the optical resonance condition requiring half-wavelength of the laser source. Optical losses in a optical cavity is generally large with small L , or R , and must be optimized for highest sensitivity achievable.

Many groups have used cavity optomechanics in various sensing applications including on-chip accelerometers, force sensors, and magnetometers with demonstrated sensitivities of $10 \mu\text{g}/\sqrt{\text{Hz}}$, $15 \text{ aN}/\sqrt{\text{Hz}}$, and $400 \text{ nT}/\sqrt{\text{Hz}}$, respectively - shown in Fig. 1.4 (32)-(34). From all the accomplishments in on-chip cavity optomechanics, this relatively new platform is rapidly growing as one of the best experimental tools for nanoscale science (29). In this competitive field of optomechanics, I have taken the initiative to base my project in experimenting torsion-based optomechanical systems to further reduce the size than previously reported paddles while increasing the sensitivities.

1.3 Torsional optomechanics

With all the successes that cavity optomechanics devices have achieved in on-chip platforms, it was highly desirable to get a comparable displacement sensitivity in on-chip torsional devices. If small torque sensitivities can be reached, it will open doors of probing various torque-related systems in the nanoscale regime - for example magnetism, superconductors, and superfluid films. The purpose of this thesis is to improve the sensitivity over previously reported torsional devices (14) using cavity optomechanics. The outline of this thesis consists of first, introducing the optomechanical geometry designed for the chip with post-processing to release the mechanical structures. I then describe all the construction details for the apparatus for obtaining high-sensitivity in optomechanical devices, including some of the challenges I faced in dimpled tapered fibres to inject light into WGM microdisks. From the success in obtaining the optomechanical torsion data, my first paper was published in Applied Physics Letters (36) - which this thesis was based on. I also included some on-going projects with these torsional devices for applications as part of Chapter 5 and Appendix C. In short, my project confirms that optomechanics is a viable platform for high-sensitivity torque measurements and can be used for other applications that involve smaller torsion devices.

CHAPTER 2

Post-Processes for Commercially Fabricated Chips: Optomechanical Designs and Cleanroom Recipes

Let us cleanse ourselves from all filthiness of the flesh.

- 2 Corinthians 7:1

Single-crystal silicon has been highly favoured in complementary metal-oxide-semiconductor (CMOS) industries based on its excellent optical properties to combine compact photonic devices to integrated circuits. Silicon also has an additional advantageous feature in the form of its mechanical properties (37) - which is highly elastic (Young's modulus), suffering very little mechanical dissipation, and is extremely stable in frequency (38). This thesis is dedicated solely to single-crystal silicon that excels in both optical and mechanical properties and hence is well-suited for optomechanical platforms.

2.1 Commercially fabricated on-chip optomechanics

Similar to the demonstration of optomechanics using high-reflecting mirrors as shown in Fig. 1.2, I have designed a whispering-gallery optical disk evanescently coupled to a mechanical torsion paddle rendered in Fig. 2.1. The design of evanescent optomechanical structures requires consideration of two important criteria: the smoothness in the whispering-gallery-mode (WGM) cavity, related to Q_{opt} , and the gap between the optical and the mechanical resonators, related to G . To fulfil both requirements of having smooth sidewalls and small gaps, lithography for patterning and plasma for etching must be highly optimized.

The two mainstream lithography methods, optical and electron-beam lithography (EBL), each have their merits and disadvantages. Optical lithography is highly cost-efficient since

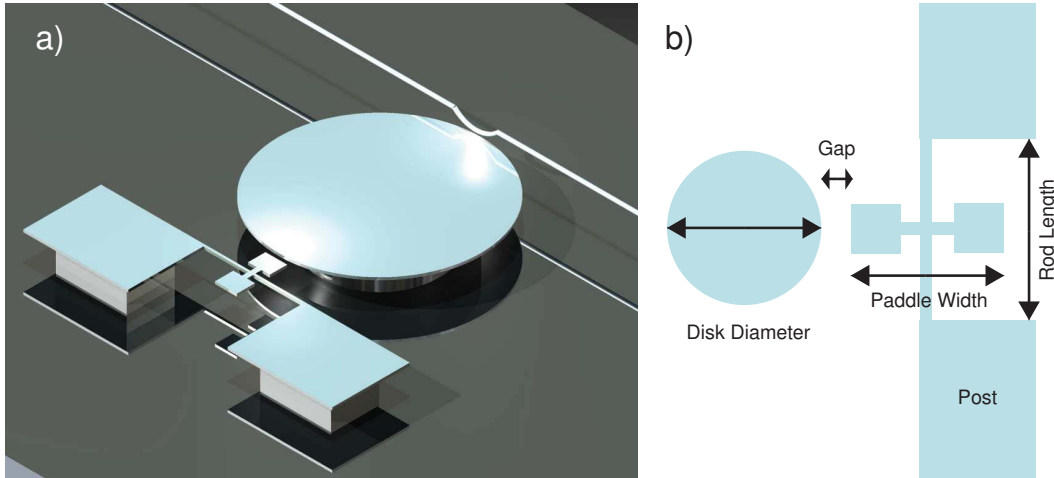


Figure 2.1: a) Rendered image of the optomechanical torsion platform. A dimpled tapered fibre couples light into a microdisk WGM resonator, which is evanescently coupled to a mechanical torsion oscillator. b) Basic description of the geometry used for the optomechanical torsional design.

the use of a photomask enables mass-printing of devices, but generally suffers from feature resolution due to the diffraction limit of the UV source and non-uniformity of the photoresist from mask contact. For example, optical lithography done at our local cleanroom (UAlberta-Nanofab) was limited to $1.5 \mu\text{m}$ using a 365 nm UV source. To go to sub-micron features EBL provides a solution for small batch sizes; however, the overall process can be very slow and costly in comparison to photolithography. Fortunately, industry have been heavily utilizing a 220 nm thick silicon-on-insulator (SOI) platform, specialized for developing silicon photonic devices, which have a high index of refraction (3.42) and negligible absorption in the telecom wavelength band ($1300 \sim 1630 \text{ nm}$). A deep-ultraviolet (DUV) photolithography method uses excimer lasers (193 nm or 248 nm) and high-definition photomasks to produce large volumes of devices with small features down to 130 nm (39). The cost for acquiring commercially patterned SOI wafers can be quite high but in our case, the cost was opportunely subsidized through CMC Microsystems - an organization that linked us to the Interuniversity Microelectronics Center (IMEC) foundry, where the devices were actually fabricated.

The costs were further reduced by sharing the purchased area of $6 \text{ mm} \times 6 \text{ mm}$ square block between four collaborating groups. Our allotted design area was $\sim 6 \text{ mm} \times 2 \text{ mm}$, which offered ample room to design numerous micron-scale optomechanical devices while varying several key parameters. For this, we used the GDS layout software (DW-2000), which has the unique capability to check customized design-rules set by IMEC, making it

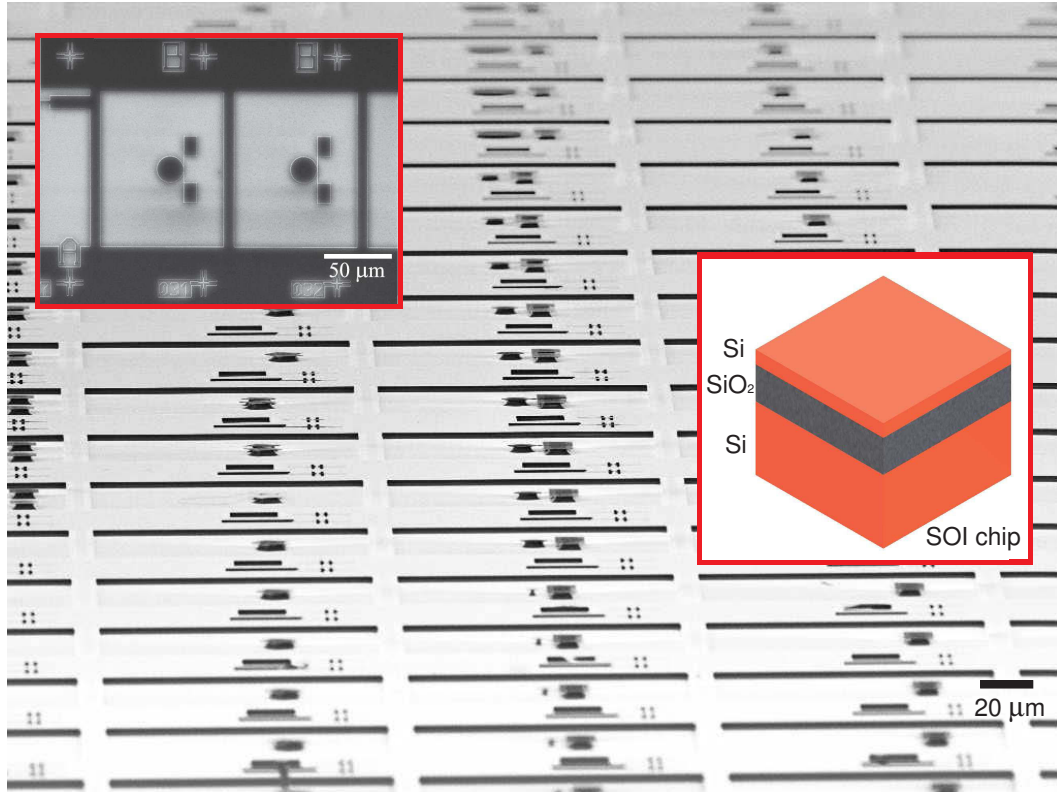


Figure 2.2: An angled SEM image of a commercially fabricated optomechanical chip, which was post-processed to etch away the buried oxide layer (SiO_2). There are vast number of different optomechanical devices and their parameterizations. The left inset shows a top view illustrating the void space ($100 \mu\text{m} \times 150 \mu\text{m}$) surrounding the device to give enough room for dimpled tapered-fibre alignment. The right inset shows the typical SOI platform where the top layer was $\sim 220 \text{ nm}$ on top of a sacrificial layer (SiO_2) of $2 \mu\text{m}$, suited for photonic devices near 1550 nm .

possible to submit error-free designs. For example, acute angles under 85° or width below 100 nm were rejected from IMEC where DW-2000 software pointed out all the areas that needed fixing.

Once the error-free designs were submitted, the turnaround time for the fabrication process was eight months - which could be a major disadvantage for implementing commercially fabricated devices in research-based projects. This is because the foundry collects all the designs from various groups to be cost-efficient with the mask design, which results in lengthier waiting time. During the two years of my graduate studies, I was able to design two sets of commercially fabricated devices. The first batch was primarily designed to conclude which optomechanical platform provides the best sensitivity for different optical and mechanical systems and the second run consisted of improving the parameters based on the first batch. I efficiently used the waiting period to improve our optomechanical coupling setup, develop a systematic approach for dimpled tapered fibre fabrication, and optimize the post-processing recipe using EBL.

Despite the long delay, I was very pleased with the finished product, characterized with scanning electron microscope (LEO 1430) shown in Fig. 2.2. We requested and received two different exposures, a high and a low dose, for each 8-inch wafer - which was then diced and divided among the collaborated groups. The high exposure dose was basically optimized for photonic crystal holes to match the designs precisely, while low exposure dose (standard dose) are optimized for waveguides structures. Since I did not have any photonic crystal designs, the high-dose chip was mainly used for testing recipes and standard dose were primarily used for collecting torsional data. The metrology of the silicon layer thickness, provided by IMEC, was 227 nm on average from one edge of the wafer to the other, with the minimum being 222 nm and maximum being 233 nm - making it fair to assume uniformity in an individually diced chip ($1\text{ cm} \times 1\text{ cm}$).

2.1.1 Optical resonator designs

An optical cavity is at the heart of all optomechanical platforms, which any mechanical mode that modifies the optical pathlength can be measured. Properties of optical resonators are highly important during the designing process to achieve high Q_{opt} and small optical mode volumes. The Q_{opt} is related to the dissipation in optical resonators which is affected by the surface roughness from the fabrication. Since the fabrication is optimized from the foundry and is consistent within the wafer, I have considered many types of optical cavities in search for high Q_{opt} device. I particularly focused on the WGM family of resonators including

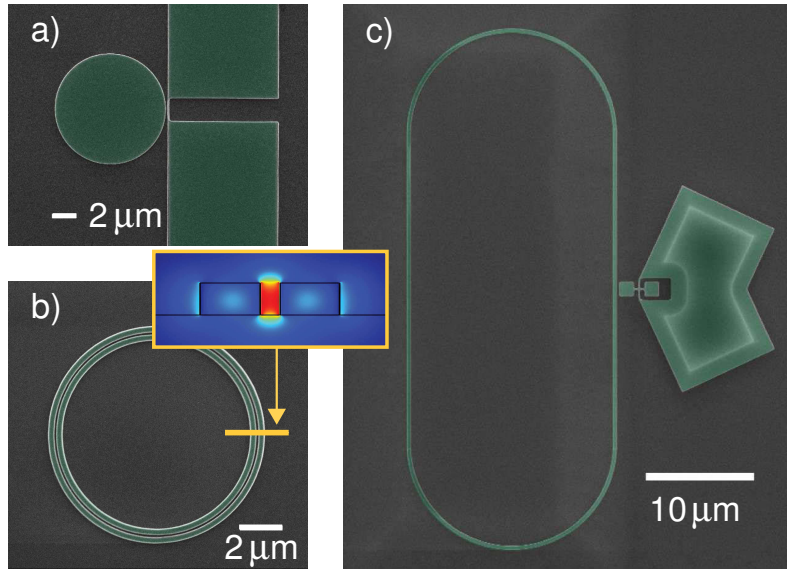


Figure 2.3: Some of the optomechanical devices in the first-year designs are shown in SEM images with false green colour: a) an optical microdisk coupled to a doubly-clamped beam, b) a slot ring resonator with its cross-section optical mode profile (inset), and c) a racetrack resonator coupled to a torsion device.

rings, racetracks, slots, and disks to avoid design-overlaps with other groups. In particular, ring and racetrack cavities were first implemented because they support single mode in telecom wavelengths making it favourable (40). Slot resonators are unique where the light is guided in the gap (air) between the structures (41) (Fig. 2.3b inset) providing a higher energy density in the gap. Lastly the disk resonators were incorporated to have higher order modes, providing more resonances to work with but can be difficult to analytically identify each mode shapes. From all these designs, I also varied the size of the cavities, or optical mode volumes, to experimentally find the best data achievable for torsion devices.

After submitting these designs to the foundry I have worked on dimpling a tapered fibre as to have a low spot necessary for accessing each optical resonators on a 2D chip illustrated in Fig. 2.1a. The dimpled tapered fibre is a highly efficient coupler, being a direct coupler, rather than going through a lossy Bragg-gratings typically used for silicon photonics (42). Using dimpled fibre-taper also conserves design space without having to design large photonic circuits with waveguides. The only design requirement is a void space around the device ($100 \mu\text{m} \times 150 \mu\text{m}$), shown in the left inset of Fig. 2.2, for fibre alignment. Although it took about six months to optimize the dimpled tapered fibre procedure, the fibres are now systematically reproducible (Section 3.2.2).

From my naïve approach to couple light from the dimpled fibre-taper directly to the WGM cavities such as ring, race-track, and slot resonators were found experimentally incompatible due to a large modal mismatch between a resonator and fibre-taper. Tapered fibres typically have diameter near $1\ \mu\text{m}$, which is large compared to a thin ring resonators. To increase the coupling efficiency - either making thinner fibres comparable to the photonic waveguide thickness of $\sim 500\ \text{nm}$ or adiabatically tapering the silicon waveguides, will increase its efficiency. The former was experimentally difficult to mould a dimple out of a smaller fibre diameter than $1\ \mu\text{m}$, and the latter work was recently done by the Painter group using tapered waveguides to achieve an efficiency of 85 % (43). I instead investigated a significant number of microdisks in which the fibre-coupling was successful.

2.1.2 Mechanical oscillator designs

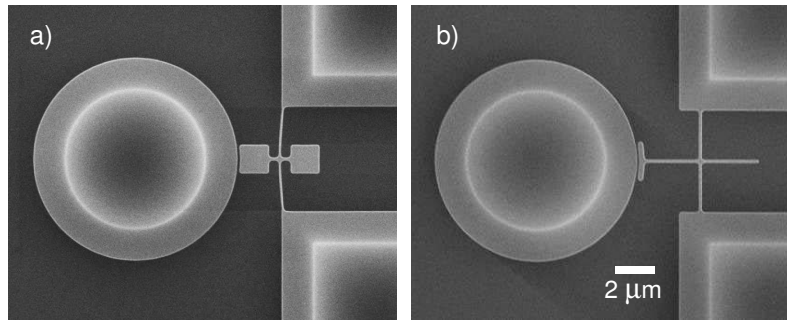


Figure 2.4: Fully released optomechanical torsion devices are shown in SEM micrographs used in this project. a) The first-year batch of torsional designs consist of a simple paddle attached to a torsion rod hanging at the edge of the posts. The bending of the torsion rod is evident where the designed gap of 130 nm got closer to 100 nm after the drying step processed at the cleanroom. b) In the second-year designs, the torsion rods are straighter by introducing an offset from the end-posts ($\sim 1.5\ \mu\text{m}$) to enhance the rigidity of the torsion rod supporting trimmed torsion paddles.

Taking advantage of the large design area, along with the optical cavity designs, I have also made different mechanical devices coupled to microdisks. Examples include doubly-clamped beams, cantilevers, and torsional devices - where I focused primarily on the simple paddle designs shown in Fig. 2.4. The mass for these torsion devices are $\sim 25\ \text{pg}$ (Fig. 2.4a), computed from the volume integral of the density of silicon in COMSOL using exact geometries obtained from a SEM image, and was further reduced to $\sim 0.7\ \text{pg}$ in the second IMEC batch - where the paddles are significantly trimmed (Fig. 2.4b).

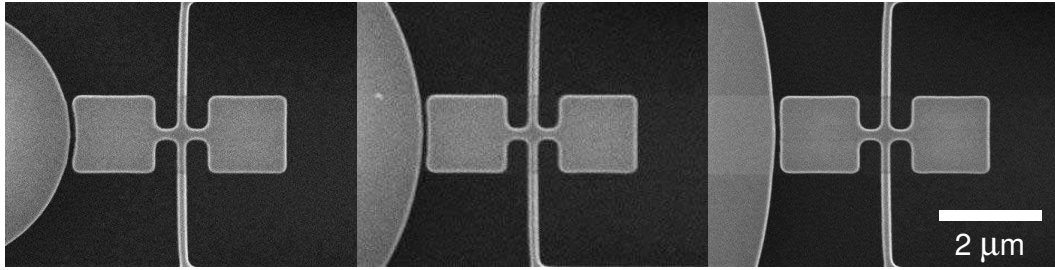


Figure 2.5: Magnified SEM images showing different curvature of the end paddle matching the curvature of the 5 μm , 10 μm , and 20 μm diameter disks, respectively, from left to right.

One of the differences observed in the first and the second year designs, other than the shape of the paddles as shown in Fig. 2.4, is the bending of a torsion rod due to wet-etch/drying procedures performed at the Nanofab. The capillary force during the dry-step resulted in a curved torsion rod as shown in Fig. 2.4a and this bending was avoided in the second year designs by placing the rod towards the centre, or an offset from the edge, increasing its rigidity (Fig. 2.4b). Other design observation from Fig. 2.5 is the curvature at the end of the paddle to match the disk it is coupling to, illustrated in Fig. 2.5. The 5 μm diameter disk, for example, results in larger curvature of the paddle. These slight differences in the curvature resulted in the change in the moment of inertia for these paddles where optomechanics was able to resolve these small changes (Section 4.1.4.2).

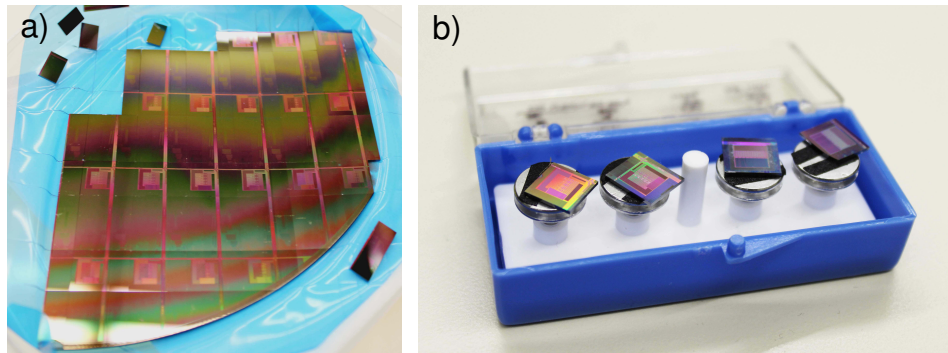


Figure 2.6: The diamond saw at the Nanofab was used to precisely dice the commercially made wafers into individual chips of 1 cm \times 1 cm shown in a). A photograph of the fully post-processed chips prior to the experiment is shown in b) where the left two chips are the first year designs and the right two chips are the second year designs.

2.2 Post-processing

The 8-inch wafers were diced quarterly for both high and low doses from the foundry, which made it easy to divide among the four groups. The quarter wafers were further diced into individual small chips with sizes $\sim 1 \text{ cm} \times 1 \text{ cm}$ including the extra spaces around the edges ($\sim 3 \text{ mm}$) to give freedom for mounting and handling the chip with tweezers (visible in Fig. 2.6b). The dicing procedure was done at the Nanofab using the diamond saw (Disco DAD 321). Before dicing, wafers were coated with a protective resist by the foundry to shield the devices. Without the protection layer, small chipped silicon pieces on devices from dicing can be difficult to remove later and could possibly damage the delicate structures. The dicing is usually done automatically if the spacings are known accurately, but I performed them manually to avoid any mistakes. These $1 \text{ cm} \times 1 \text{ cm}$ chips were then ultrasonically cleaned with acetone and rinsed with isopropyl alcohol (IPA) to remove the protective layer but resist residues still remain, which requires additional cleaning at the cleanroom.

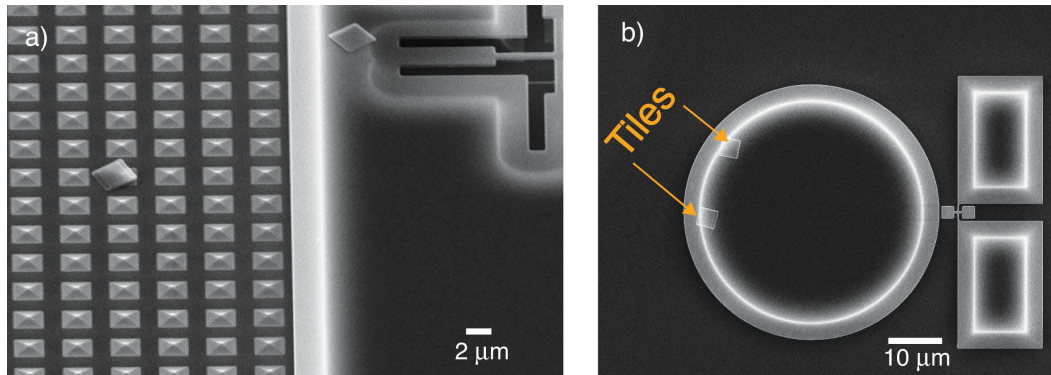


Figure 2.7: a) To maintain a certain uniform etch-density throughout the wafer, tiles are patterned by the foundry in empty spaces (typically outside the design area), presented in the SEM image. b) During the $2 \mu\text{m}$ deep SiO_2 etch process, tiles that are $1.5 \mu\text{m} \times 1.5 \mu\text{m}$ detach completely and land on random areas on a chip - which can damage critical devices.

Although the hard part of patterning and etching was done by the foundry, there were still steps to take in the local cleanroom for post-processing. The optomechanical devices include mechanical structures that must be released via wet-etching. One immediate concern with that was the tiles present in all the void spaces throughout the chip shown in Fig. 2.7a. These $1.5 \mu\text{m} \times 1.5 \mu\text{m}$ dummy structures are inserted by the foundry to maintain a certain etch density throughout the wafer for optimum results. The problem arises when a buffered-oxide etch (BOE) is performed to remove the SiO_2 layer, allowing these structures to be

completely released and land on devices where it is impossible to remove them as shown in Fig. 2.7b. These tiles thus needed to be masked properly by an optical lithography step prior to the wet-etching SiO_2 .

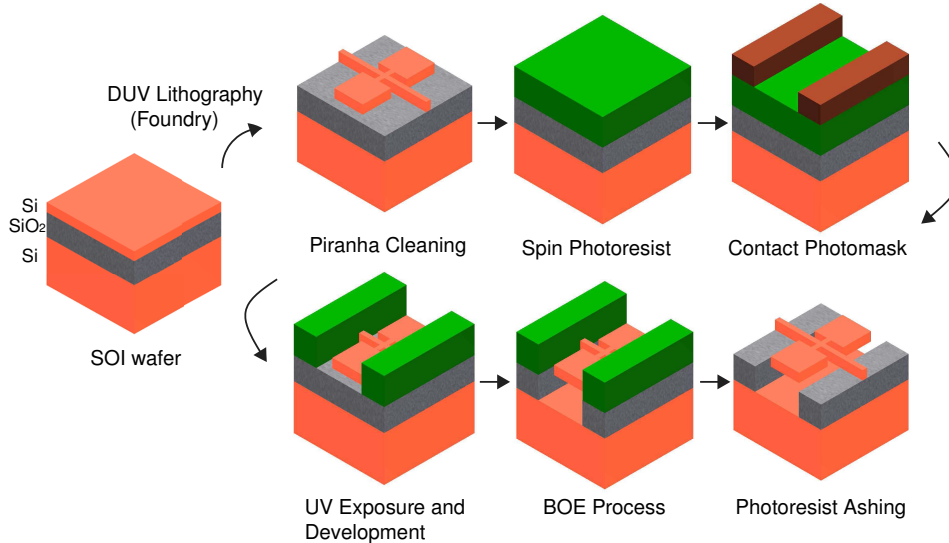


Figure 2.8: A full processflow performed at the Nanofab after receiving commercially patterned chips to etch-release mechanical devices while simultaneously mask unwanted structures via photolithography. The main steps include piranha cleaning, optical lithography patterning, and wet-etching the SiO_2 layer.

The overall process-flow in Fig. 2.8 highlights the steps required for chip preparation that includes successive cleaning, masking, and wet-etching. All of the above steps were processed carefully at the Nanofab cleanroom to properly handle hazardous chemicals namely piranha, hexamethyldisilazane (HMDS), and hydrofluoric acid (HF) solutions. The final result of piranha cleaned, photolithography patterned, and wet-etched chips are shown in Fig. 2.6b prepared for testing in the optomechanical vacuum chamber.

2.2.1 Recipe for piranha cleaning

As mentioned earlier the recipes for cleaning and wet-etching require extra caution for handling harmful chemicals. The piranha solution, typically a 3 to 1 mixture of sulphuric acid and hydrogen peroxide, produces an exothermic reaction near 120°C and actively strips any organic material and many metals (44). Therefore the piranha wet-deck is specially isolated from other wet-benches to prevent any organic or other chemicals from mixing with this aggressive piranha solution. Chemical gear including protective apron, latex gloves, and

face shields must be worn at all times during the process. For an individual chip, a mixture of 150 mL of sulphuric acid and 50 mL of hydrogen peroxide was used for a 30-minute cleaning cycle. Half way during the process, small amounts of hydrogen peroxide (~ 10 mL) were added to maintain the high temperature. After completion the chip was thoroughly rinsed with distilled water and was dried with a nitrogen-gun followed by a dehydration cycle on a hotplate (110°C) for 10 minutes.

Although the public beakers at the Nanofab cleanroom are generally cleaned and maintained, I found a few instances where the devices ended up dirty and I had to redo the process. We have our own private lab beakers now at the Nanofab in my storage, totalling about 10 beakers, reserved for each specific chemicals and their processes. When using private beakers, I had to make sure to aspirate the piranha solution myself after waiting about 2 \sim 3 hours to sufficiently cool the piranha solution.

2.2.2 Recipe for photolithography

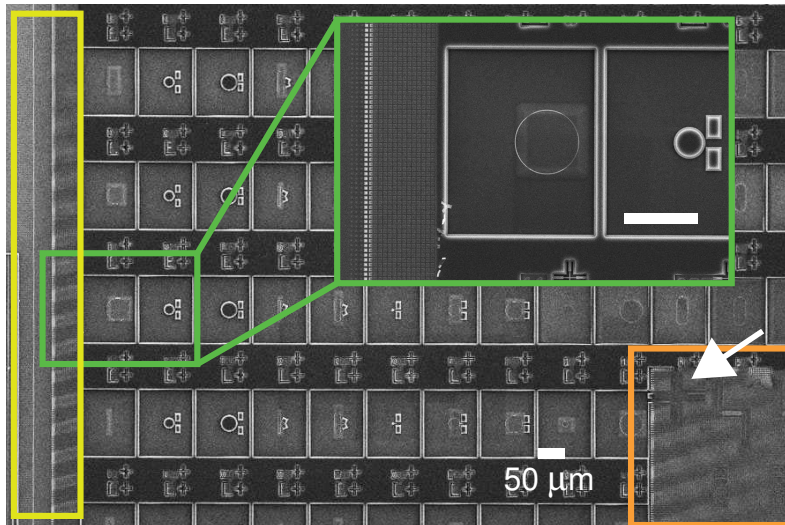


Figure 2.9: A zoom-out SEM image of a fully post-processed chip which a photolithography step was included to preserve all the thin ring structures (green inset) while masking all unwanted areas such as tiles (yellow) and other group designs (orange). Both large and small alignment marks are clearly visible in the image where the large alignment mark ($100\ \mu\text{m} \times 100\ \mu\text{m}$), indicated by the white arrow, was primarily used for alignment during the photolithography step.

When wet-etching was first performed to release the torsional structures on a piranha cleaned chip, I immediately realized that the tiles were very damaging to the structures (Fig. 2.7).

Therefore an intermediate step was inserted between the cleaning and the wet-etch processes to mask all unwanted structures properly using photolithography. To perform photolithography, a photomask is first required. Designed by DW-2000 software, a Cr photomask was produced from the pattern generator (DWL-200) at the Nanofab. The minimum guaranteed feature size of the mask was limited to $1.5 \mu\text{m}$ which is sufficient for masking unwanted areas while perserving the ring, racetrack, and slot cavities shown in Fig. 2.9. During the waiting period for the Cr mask to finish, I have attempted a different approach to minimize the tiles landing on random areas. I have clamped the chip on a plastic tweezer faced-down with a slight angle such that the design area is at the highest point. This approach gave a temporary solution leaving many devices unharmed; however, proceeding with the photolithography was the best method.

The patterned Cr mask was installed in the mask aligner (ABM) for alignment and the chip was prepared by spinning the photoresist. The chip was first placed in an oven (YES HMDS) to produce a thin adhesion layer for the photoresist (HPR 504). HMDS is a dangerous chemical and one must be cautioned not to inhale this vapour while opening and closing the oven. After the 30-minute cycle for applying a adhesion layer, HPR 504 resist was spun for 10 seconds at 500 RPM and 40 seconds at 4500 RPM followed by a hard bake (Soitec) at 120°C for 90 seconds providing a uniform $\sim 1.25 \mu\text{m}$ layer ready for mask alignment. There are alignment marks designed and patterned in the 4 corners of the chip with dimensions $100 \mu\text{m} \times 100 \mu\text{m}$ in size for coarse alignment and there are also smaller alignment marks throughout the chip for fine alignment ($5 \mu\text{m} \times 5 \mu\text{m}$) shown in Fig. 2.9. The aligner can move in 4 translation axes (x, y, z , and θ) including the rotation to align the chip carefully using an optical microscope. After careful alignment the chip is exposed for 2.3 seconds under a UV source with the measured intensity of $11.4 \text{ mW}/\text{cm}^2$. The chip is then placed in a developer (SPR 354) for 19 seconds followed by a final bake of 15 minutes at 90°C . The resist can be re-patterned if it is not satisfactorily seen in a microscope objective where the chip can be simply washed with acetone and IPA rinse to redo the entire above process. The HMDS coating step can be skipped at this point and the rest of the procedure above is reprocessed.

To successfully translate the features patterned in the photomask onto a photoresist-spun chip, good contact, either vacuum or hard contact, must be attained to minimize the diffraction error. Although the vacuum contact was preferred to eliminate the gap between the mask and the chip, it was not always possible due to the small chuck that was used to hold the chip (Fig. 2.10c). The travel distance of the stage did not allow the chip to map all the areas of the 5 inch \times 5 inch photomask illustrated in Fig. 2.10a where the hard contact method should be used. This is done by attaching the chip on a blank Si wafer at

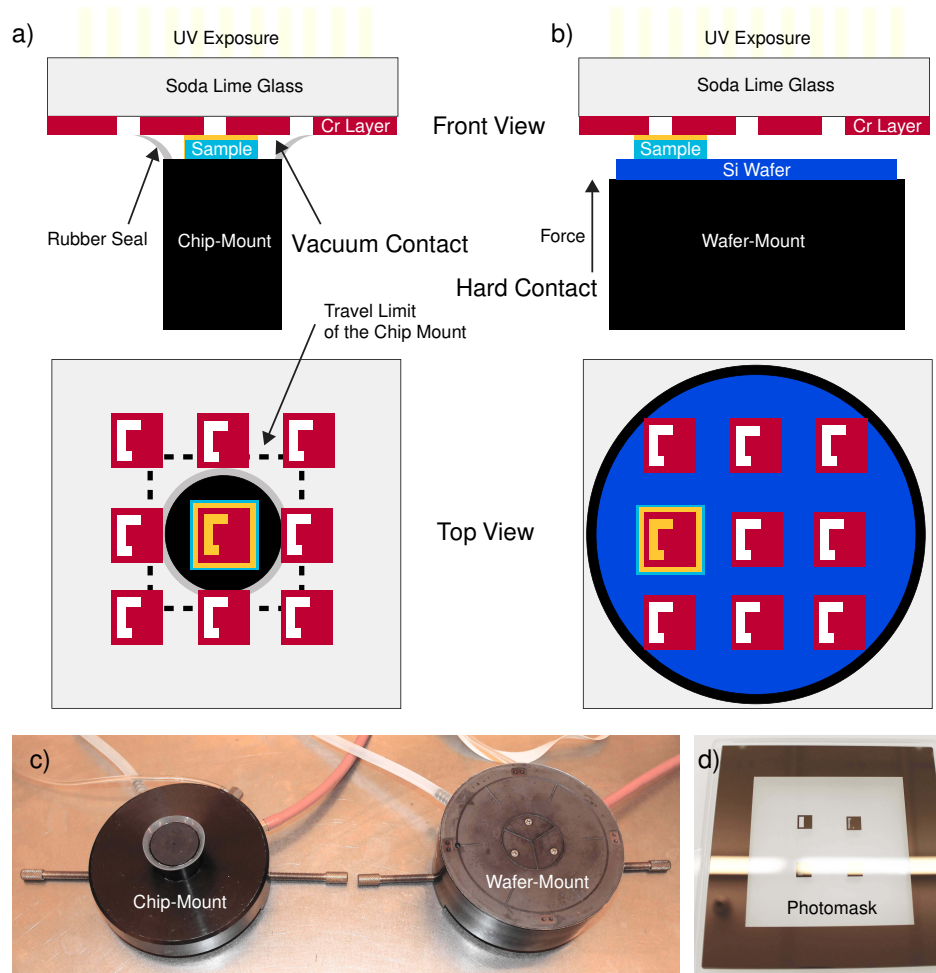


Figure 2.10: Illustrations of two methods for achieving good contact during a photolithography process. A vacuum contact was typically used, seen in a), if the travel range of the chuck can be aligned with the mask. Otherwise a hard contact, shown in b), was used by mounting the chip on a bare silicon wafer utilizing a wafer chuck. The real image of these two mounts are shown in c) and the chromium photomask that was used in d).

a desired location using a removable adhesive (Crystalbond 509) and applying a significant force upwards after alignment. The Crystalbond 509 adhesive responds to heat where the silicon wafer was placed in a hotplate briefly and applied the adhesive stick to create a small droplet to attach the chip. The glue hardens when cooled and can be removed by placing it onto the hotplate again. The remaining glue can be removed by acetone and IPA using soaked Q-tips.

After performing optical lithography with the same photomask numerous times, the mask inevitably collects residues from the resist from multiple contacts. When the acetone and IPA fail to clean the photomask, a cold piranha can ensure the mask is as clean as if it is brand new. The cleaning process is same as the previous section, with the difference of letting the solution cool down to room temperature. The hot piranha does etch the chrome slowly (45) so the piranha solution must absolutely be cooled prior to mask cleaning. The cleaning is done typically for 45 minutes depending on the condition of the mask.

2.2.3 Wet-etching the sacrificial layer, SiO_2

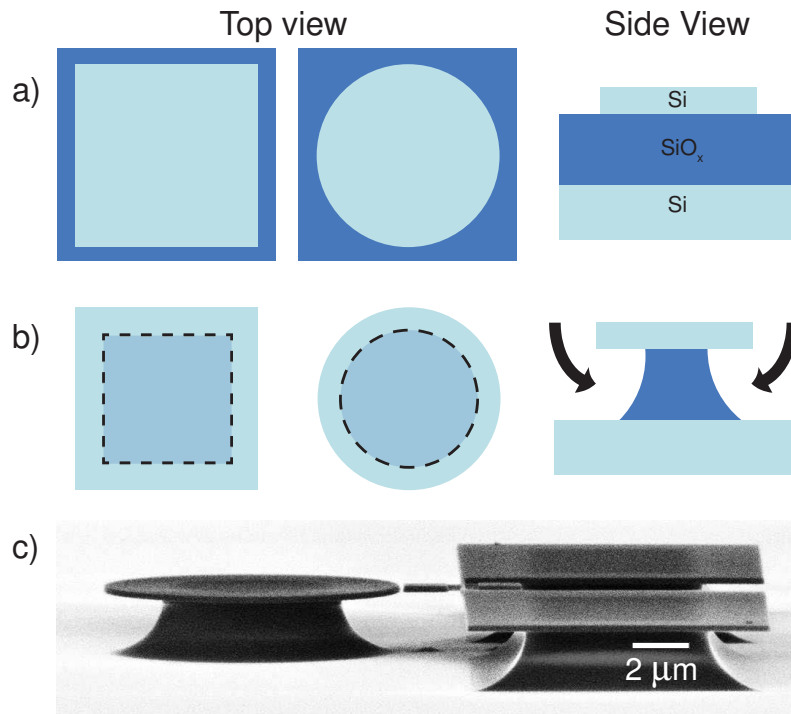


Figure 2.11: Demonstration of SiO_2 wet-etch on a patterned SOI chip using BOE. The top and the side views of a square and a circular geometries are illustrated in a), where the BOE process removes the sacrificial layer (dark blue) isotropically (SiO_2) as shown in b). A SEM image of a fully BOE processed device is displayed in c).

Once the devices are properly masked with a photoresist, as confirmed through an optical microscope, a BOE process is performed to remove the sacrificial layer of SiO_x without harming the single crystal silicon as illustrated in Fig. 2.11. Hydrofluoric acid (HF) etches the SiO_x layer isotropically, creating an undercut as shown in Fig. 2.11, and is resistant to photoresists; however, the etch rate is often difficult to control (44). The BOE comprises a

10:1 mixture by volume of dilute HF and ammonium bifluoride ($\text{NH}_4\text{F}\cdot\text{HF}$), which acts as buffering agent, stabilizing the pH and controlling the etch rate. The etch rate was found to be ~ 55 nm/min where the total time for BOE process was determined to be 36 minutes to etch the $2\ \mu\text{m}$ thick SiO_x layer. The BOE process was performed with extreme caution using plastic beakers (polymethylpentene) and tweezers to immerse the chip in the solution. I was equipped with a chemically resistive gear, to avoid any exposures that are difficult to detect.

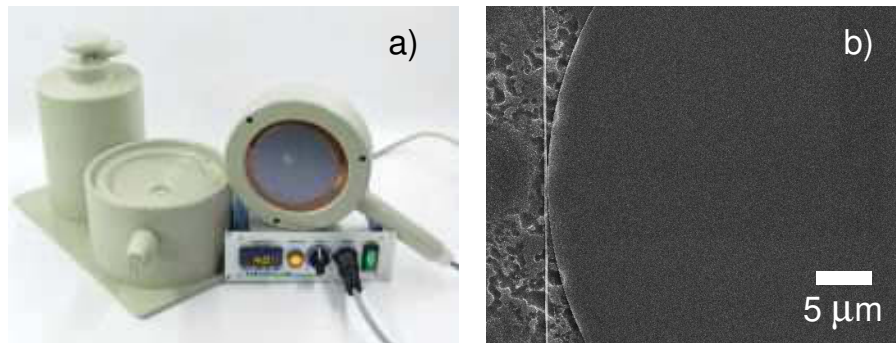


Figure 2.12: a) The HF vapour etcher (Idonus VPE150) at NINT. I have attempted to avoid stiction using this equipment, but the outcome in b) shows an undesirable anisotropic etch in contrast to the wet-etch.

The BOE is a popular and a powerful method; nonetheless being a wet-etch - it poses another problem, called stiction, where the strong capillary force from the surface tension of water makes any devices that are close together stick. One method of avoiding this is the HF vapour method. The vapour etcher is located at the National Institute for Nanotechnology (NINT) cleanroom where the vaporized HF etches the SiO_x to skip the wet-etch step. The sealed HF container is boiled to produce HF vapour to etch the chip mounted on the bottom lid via electrostatic force. Handling HF vapour is extremely dangerous even under a fume hood and requires extra safety precautions. During my training with this equipment, I found that these etch-rates were not at all consistent. I have attempted to come up with a steady recipe for HF vapour and failed after several attempts since it was highly dependent on the chip location, the temperature, and the time. Each test had very different etch rates, where on average the etch rate increases with time (table 2.1) and is highly dependant on the location of the chip. Perhaps longer etch-time at a marked location might stabilize the etch-rate but I have not pursued vaporized HF-etch further as it is an extremely harmful chemical and I have not found a great need for this method. There are more conventional ways to avoid stiction in combination with wet-etching, described in the following subsection. The HF vapour is worthy of revisitation if smaller gaps should be present in the device (< 50

Minutes	Average Etch-rate (nm/min)
1	16
2	51
3	75

Table 2.1: Inconsistent etch rates obtained using HF vapour from averaging five trials for etch times of one, two, and three minutes.

nm).

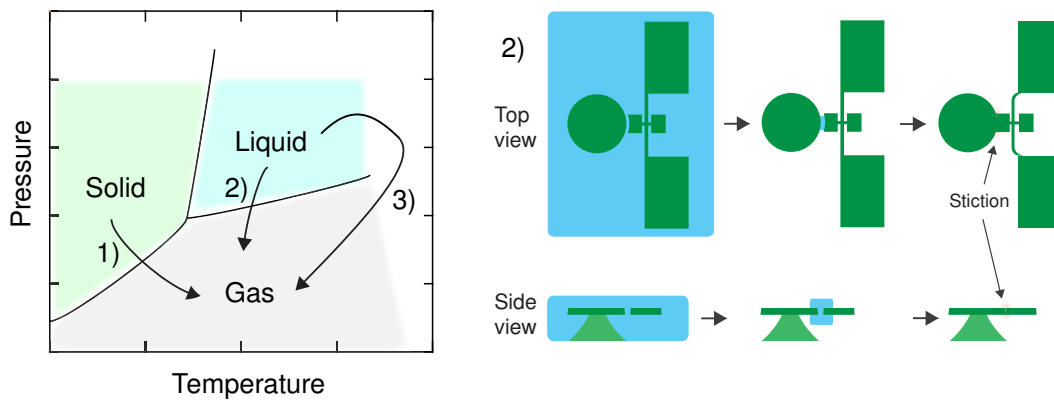


Figure 2.13: The left figure shows the general phase diagram where the problem of stiction is outlined on the right during the phase change of 2). A strong capillary force from the solution in the small gap attracts the optical and the mechanical devices causing stiction. There are two ways to avoid the stiction problem either by 1) freezing the liquid and applying sublimation or 3) critical drying the liquid to completely bypass the phase change. The latter method is by far more popular and effective.

2.2.4 Recipe for drying process without stiction

As mentioned earlier, the BOE process poses a problem called stiction where the strong capillary force from the surface tension of water makes devices that are close proximity stick together. In the case of on-chip optomechanics, shown in Fig. 2.13, where a mechanical oscillator lies outside an optical cavity coupled via very small gaps (~ 100 nm) - the stiction certainly comes into play and must be resolved. A common phase diagram in Fig. 2.13 illustrates the problem in normal drying processes and shows two alternative solutions to avoid the phase change from liquid to solid: 1) sublimation and 3) critical drying; in this work, the latter method was primarily used. The objective of this method is to replace the water in the gaps to aqueous CO_2 because of the low critical temperature (T_c) of 31°C and

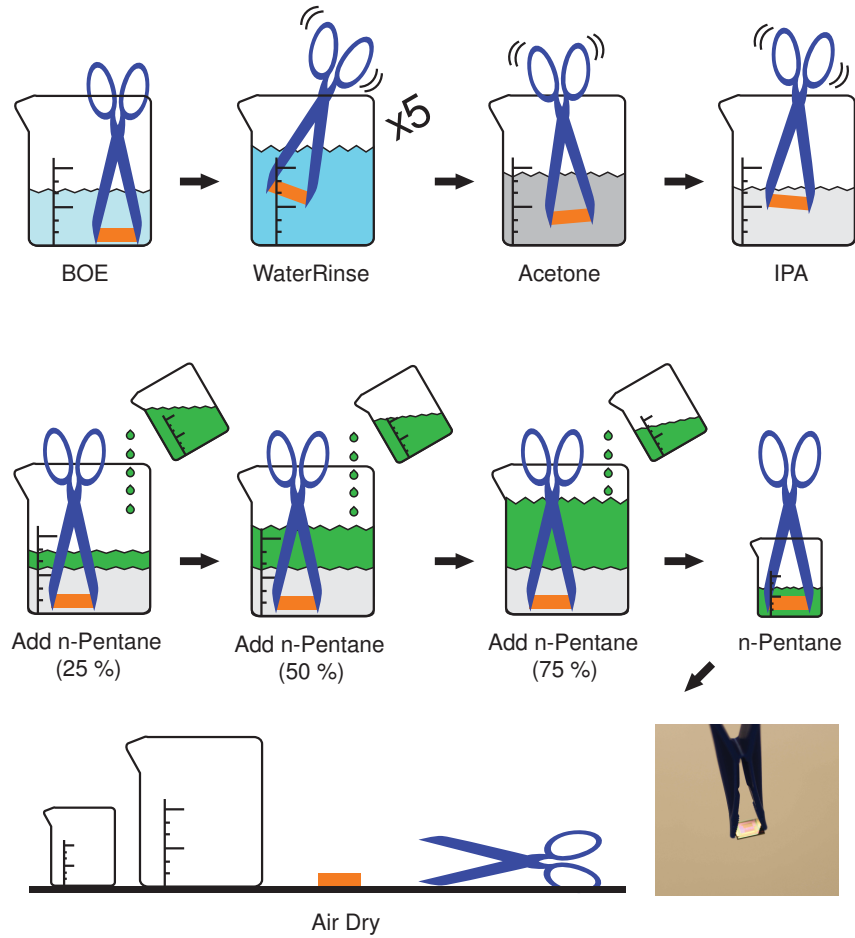


Figure 2.14: Straight forward procedure for solvent method to replace the water to a light solvent (n-Pentane) adiabatically to minimize the capillary force.

pressure (P_c) of 72 atm making it possible to easily access the supercritical phase where the liquid and gaseous phases coexist. The water-rinsed chip was quickly transferred to a solvent, IPA, and underwent critical drying process at the Nanofab. It is an automated process 45 minutes in duration with no stiction observed in SEM.

Solvent	Surface Tension (mN/m)
n-Pentane	15.49
n-Hexane	19.20
n-Heptane	21.53
n-Octane	23.25
Water	75.64

Table 2.2: Various solvents with experimentally measured surface tensions near room temperature (46). The lightest solvent, n-Pentane, was used to dry the chip as an alternative method to avoid stiction

There is an alternative method called the solvent method that was used instead of the critical point drier for equivalent results and quick processing. Table 2.2 refers to the properties of n-Pentane, n-Hexane, n-Heptane, and n-Octane, where n-Pentane was primarily used to avoid stiction (46). Instead of using the critical point of liquid CO_2 I have used a very light molecule of n-Pentane (C_5H_{12}) to replace the water - where the stiction was remarkably avoided in a simple process. A schematic of this solvent method is shown in Fig. 2.14, each step has taken 5 minutes per addition of n-pentane solution. I have not observed any noticeable differences regarding stiction by comparing these two methods, critical point drier and ultralight solvents. However I suspect that devices with gaps smaller than 100 nm should require critical point drying because the principle of bypassing phase change completely is a cleaner process. With these commercially made chips, I have mainly used the solvent method for convenience and the outcomes have been satisfactory. However, an additional plasma dry cleaning using O_2 is necessary to passivate the surface of the chip.

2.2.5 Plasma cleaning

The chip is rinsed in acetone immediately after the BOE process but the surface may not be clean as residue of photoresist may remain. Introducing another wet-solution to clean is again faced with the stiction problem and is therefore discouraged. The best way to do final cleaning is a dry plasma ashing using an O_2 recipe. A small amount of O_2 gas with high energy plasma allows the oxygen to react with most particles, allowing it to clean without any wet solution. The plasma descum process is used for 30 minutes where the chip was brought to the chamber as soon as possible.

CHAPTER 3

Experimental Apparatus for Optomechanics: Technical Details and Construction

A person who never made a mistake never tried anything new.

- Albert Einstein

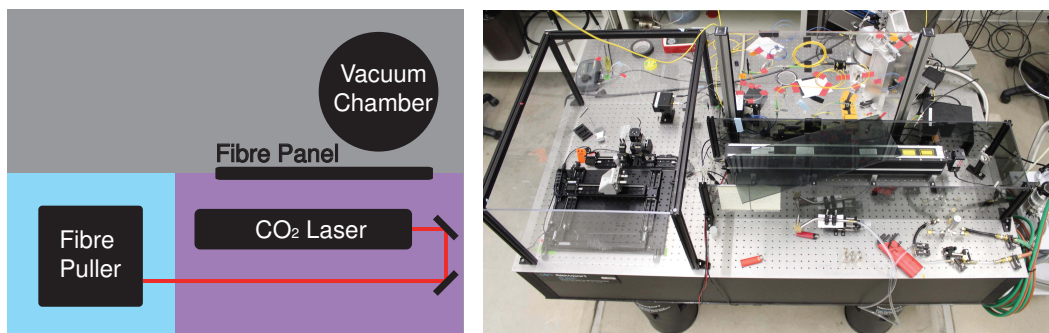


Figure 3.1: An overhead layout and a photograph of the optical table shows the optical table consisting the fibre-puller set-up, the CO₂ laser, and the optomechanical chamber.

In Chapter 1, I briefly introduced optomechanics as a powerful detection platform for on-chip devices and the possibility to integrate miniaturized torsional oscillators were highly desirable for various applications. I have chosen commercial foundries for custom chip fabrication with some post-processing done at the local Nanofab, resulting in a small-scale torsional devices shown in Chapter 2. To measure the Brownian, or thermal, motion of these torsional devices, the experiment must be free from vibrational noise. The first thing to note from Fig. 3.1 is the floating optical table placed on a vibration isolation pad, where the floor is separated from the foundation of the building to minimize any source of mechanical vibrations.

This chapter is dedicated to include all technical details involved in sensitively detecting the Brownian motion of the torsional resonator. Some of the figures and portions are based on the recently published technical paper (47).

3.1 Experimental schematic

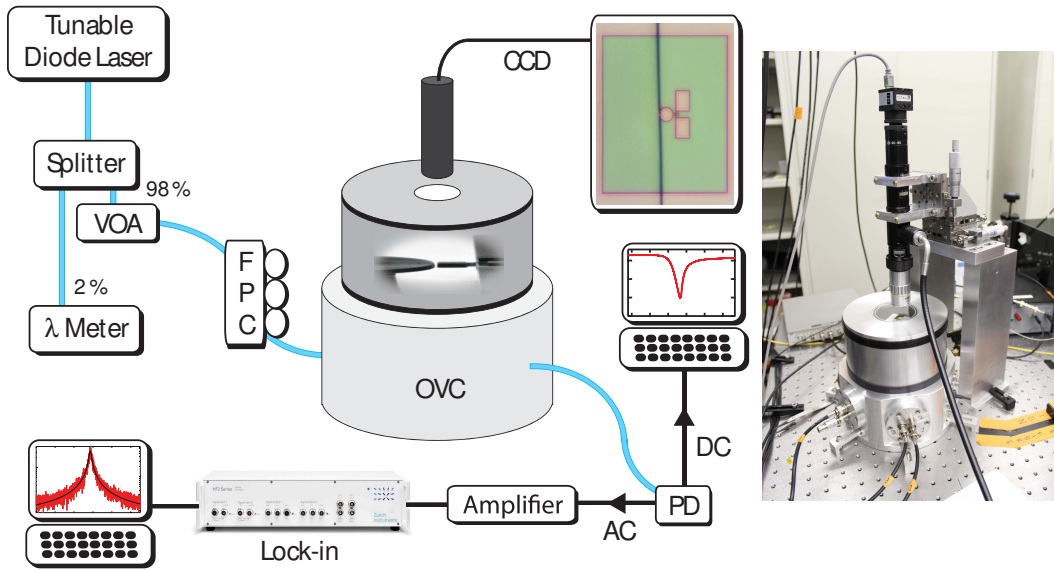


Figure 3.2: Schematic of the experimental setup centred around the optomechanical vacuum chamber (left). The fibre-based system has a dimpled tapered fibre inside the chamber together with the post-processed chip where the alignment is done through the viewport on top using a microscope. The image on the right shows a photograph of the apparatus.

The apparatus, illustrated in Fig. 3.2, gives an overview of the fibre-based detection. A tunable diode laser (NewFocus TLB-6330) is guided through a variable optical attenuator (VOA), fibre polarization controller (FPC), and the optomechanical vacuum chamber (OVC), where the dimpled tapered fibre is located, to a photodetector (NewFocus 1811). The photodetector low-pass filters the DC transmission to the data-acquisition (DAQ) device monitored by the computer and high-pass filters the AC signal, which is amplified five times and directed to either a network analyzer (HP 3577A Network Analyzer) or a high-frequency lock-in amplifier (Zurich Instruments HF2LI) to optimize the amplitude of torsional mechanical signal motion. A very short BNC cable (10 cm) was used to connect the detector (AC) to the preamplifier to minimize the noise from the cable. A glass window on top of the OVC allows careful and accurate alignment of the dimpled tapered fibre as it hovers over and touches the disk, using nanopositioning stages (Attocube) to manipulate

the chip. Optical resonances are observed by monitoring the transmission while sweeping the wavelength of the laser over its whole tunable range (1550 nm \sim 1630 nm) and corresponding mechanical peaks are found in each optical resonance. A simple schematic implementing a lock-in amplifier provided powerful results on the optical and mechanical spectrums, which are analyzed in Chapter 4.

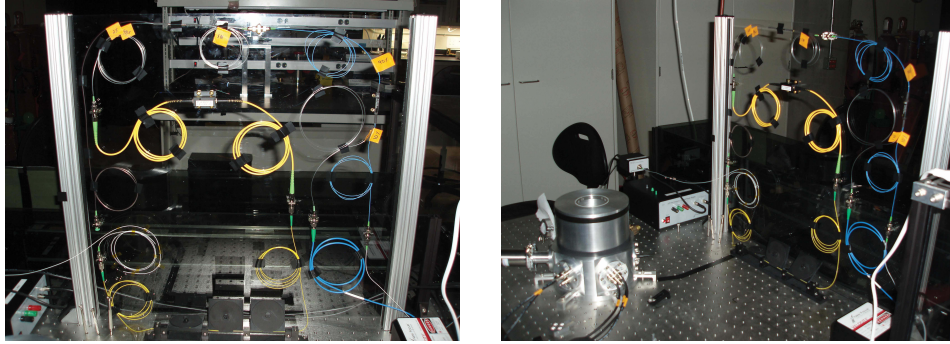


Figure 3.3: An extruded acrylic fibre-panel installed to display the fibre-based apparatus, which conserves space and provides working area in the floating optical table

To avoid fibre traffic on a limited spaces on the optical table, which often caused confusions and mishaps of the fibre, a vertical acrylic panel was installed to organize all the fibres shown in Fig. 3.3. The fibre connectors are hot-glued onto the panel that made our schematic easy to the eye. The space created on the optical table was used to fusion splice dimpled fibres, mount IMEC chips, and solder Attocube wires without difficulty.

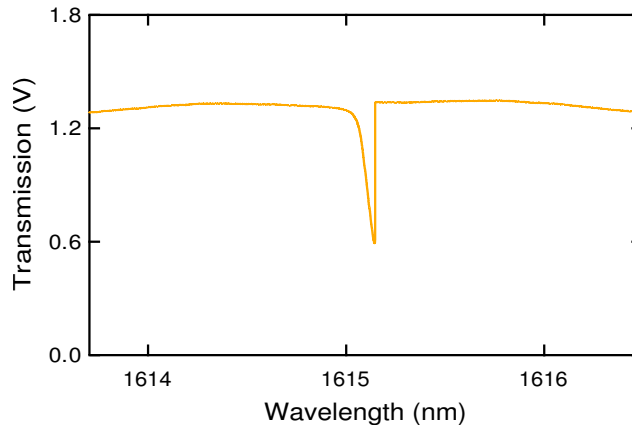


Figure 3.4: An optical bistability, or a non-linear resonance, is observed in a silicon WGM microdisk from the heating effect in silicon for high measurement power. Therefore, a VOA is necessary to adjust the laser power to avoid any non-linearity since the optomechanical transduction comes from the slope of the resonance.

3.1.1 VOA

During the experiment, we generally want low laser power to avoid any non-linearities in the optical resonances. For example, the bistability in optical resonances occurs from the two-photon absorption resulting in the thermo-optic effect of silicon in high Q_{opt} resonators (48) and is easily avoided by controlling the power through the fibre. Also the laser operates optimally for power over 10 mW, therefore the VOA (Fig. 3.5a) was necessary to attenuate the laser power outside the laser to the desired fibre transmission.

3.1.2 FPC

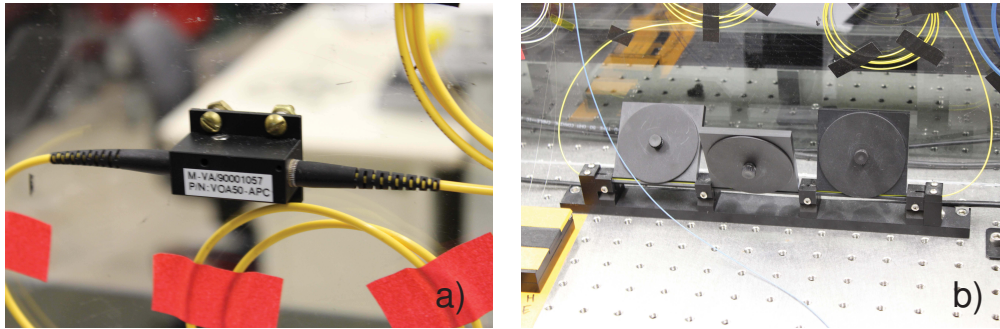


Figure 3.5: The two necessary components of the dimpled tapered fibre to control the a) power (VOA) and the b) polarization (FPC) are part of the fibre-based apparatus.

In optomechanical systems where the optics are strongly correlated with mechanics, the polarization (Fig. 3.5b) is also an important knob to optimize the mechanical signal. The FPC (Thorlabs - FPC560) uses a stress-induced birefringence of the fibre consisting of three independent waveplates and was frequently adjusted along with the wavelength and VOA to maximize the mechanical amplitude - monitored from the network analyzer (HP 3577A Network Analyzer).

3.1.3 Microscope objective

A microscope objective, capable of $\times 70$ magnification, is mounted on a xyz translation stage with custom machined legs that account for the focal length of the microscope (Fig. 3.2). Diffused LED light (Metaphase MP-LED-150) was used for illumination where the dimpled region was observed from adjusting the microscope focus shown in Fig. 3.6b. Being able to monitor the dimpled-region of a tapered fibre and the optomechanical device in real

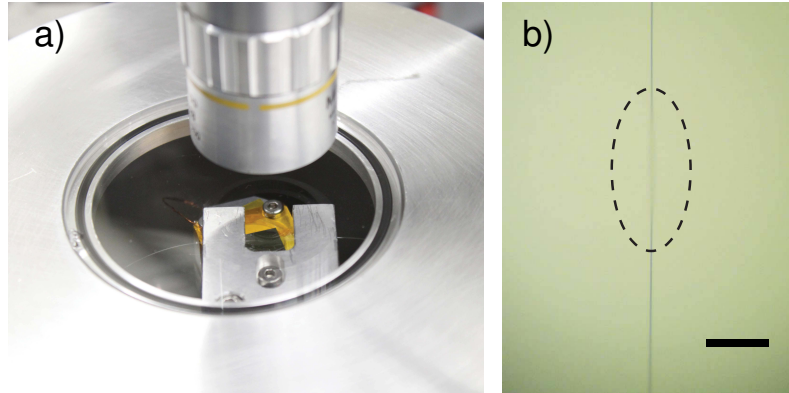


Figure 3.6: a) Zoomed picture of Fig. 3.2 centred on the microscope system showing the glass view-port for imaging. Captured image from the microscope-camera is shown in b), where the dimple region can be clearly located from the out-of-focused region. The scale bar is $100 \mu\text{m}$

time, coupling can be easily achieved with nanopositioning stages. After the fibre-dimple is properly aligned to the optical disk, the LED light must be turned off during measurements - where heating from the light induces a thermo-optic effect, or an unwanted shift in an optical resonance.

3.2 Optomechanical vacuum chamber

I have described previously the general fibre-based components where this section focuses on the main OVC chamber. This custom-designed vacuum chamber was machined at the University of Alberta physics machine shop shown in Fig. 3.2 that holds vacuum on the order of 10^{-6} Torr. There is a circular plate with periodic mountable holes inside the chamber, making it possible to arrange parts together illustrated in Fig. 3.7. In addition to the description inside the OVC, the external 6 ports, designed to accommodate a valve, a ventilation, a vacuum gauge, two electrical adapters, and an optical fibre feed-through will be explained.

3.2.1 Vacuum parts

The main purpose of constructing a vacuum chamber is to reduce mechanical damping in air so that the intrinsic Q_{mech} of the device is preserved. The vacuum environment also prolongs the tapered fibre against degradation (49) and protects the SOI chip against dust particles. To ensure these advantages, I have applied silicone vacuum grease (Dow Corning[®] - high

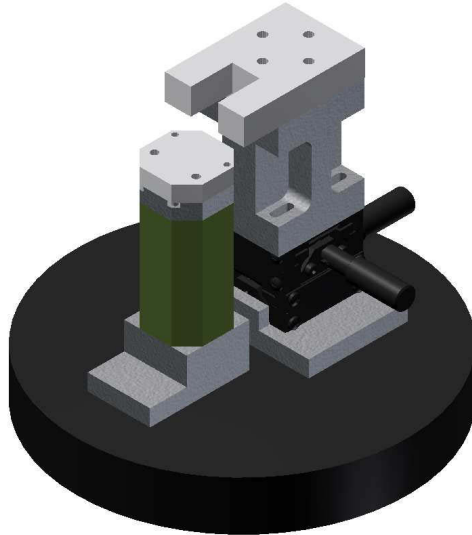


Figure 3.7: Rendered image of the arrangement inside the OVC, showing the At-tocube stacks (green) and a fibre-holder mounted on I-beam (grey) and goniometer (black).

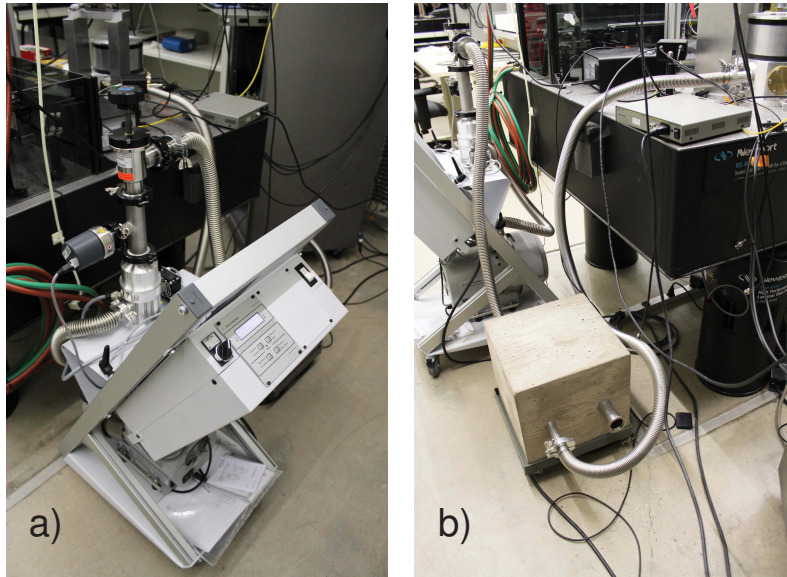


Figure 3.8: Pictures of the vacuum system. a) The turbo pump is connected to the chamber via metal bellows but the vibration is quite noticeable. b) Therefore passing through a heavy concrete block damps the vibration caused by the turbo pump.

vacuum grease) on L-gaskets (Duniway-VBJG-7) and O-rings - where all the ports and parts were assembled and leak-checked the OVC confirming that there were no significant leaks at sensitivities near 10^{-8} atm cm³/s using ⁴He gas. Excessive grease on a L-gasket must be removed by dabbing Kim-wipes to prevent outgassing and contamination on the sample. The minimum pressure reached was $\sim 10^{-6}$ Torr equipped with the dry-vacuum system (Agilent Scroll-SH-110 and Turbo-V81-AG) and KF-25 flanged metal bellows. A thick heavy block of concrete was installed to terminate all the vibration coming from the vacuum pump shown in Fig. 3.8b. I have also installed a fine mesh inside the vacuum port to protect the pump from pieces which might fall in. A thin fibre may sometimes break upon rough pumping the chamber too quickly, therefore a valve was installed to slowly evacuate the OVC. Another port had a vacuum gauge (Kurt J. Lesker - 972B Cold Cathode Pirani) attached to monitor vacuum levels of the OVC. Unfortunately, this gauge is currently not working and has been discontinued, so the gauge attached to the turbo pump (Agilent FRG-700) was used.

3.2.2 Electrical ports

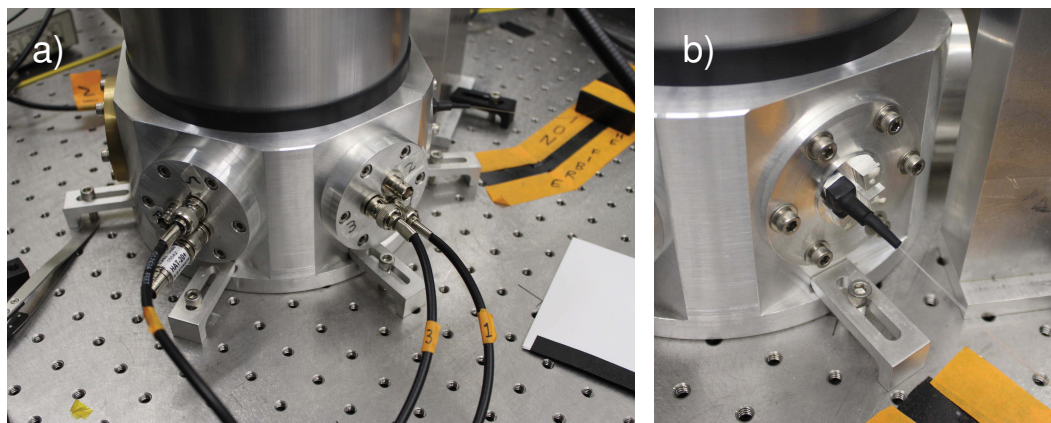


Figure 3.9: a) Two electrical ports are displayed, where three adapters were used to power the positioners inside the OVC. The extra adapter, connected with an attenuator in the picture, is wired to a piezo-actuator that is under the chip. b) For the fibre port, there are total eight holes (~ 1 mm diameter) but only two are used for fibre input and output. They are held in place using vacuum compatible epoxy, and covered with heat shrink tubing for stress-relief.

There are two ports responsible for electrical connections mainly used to power the nanopositioning stages, all hermetically sealed female BNC adapters placed in each. The inside of three BNC adapters are soldered carefully to 2-pin copper wires to connect to the three Attocube positioning stages connected to the piezo controller (ANC300) and an extra BNC adapter is wired to a piezoelectric buzzer to drive the sample out-of-plane.

During the alignment of the nanopositioning stages, electrical connections are made through a clean power source, specifically installed in our lab using an isolation transformer to filter out electrical noises into sensitive equipment, indicated by orange outlets. After successful alignment to a microdisk, it is a good practice to replace the BNC cables with an attenuator carefully to avoid any electrical noise going into the positioning stages where the chip is attached.

3.2.3 Fibre through-port

Since the experiment is centred on fibre-detection, a leak-free fibre port is necessary in the chamber. This port was custom-machined to have ~ 1 mm diameter holes for a fibre to go through, totalling 8 holes shown in Fig. 3.9b. The apparatus only requires two holes for the fibre into and out of the OVC, so the other 6 holes were sealed with vacuum compatible epoxy (Torr Seal[®]). The two holes used were also permanently fixed with the epoxy so that the fully fabricated dimpled tapered fibre can be transferred inside the chamber with the fusion-splicer (Ericsson - FSU 995 FA). The fibres inside the chamber should be long enough to give room for fusion splicing. It took about a full day for Torr Seal to completely harden, after which I covered the opening with heat-shrink tubing to reduce the stress on the fibres. The final sealed fibre-port is shown in Fig. 3.9b.

3.2.4 Nanopositioning stages

After explaining the external parts of the OVC, the first thing to mention is the critical component inside the chamber - a precise xyz stage using piezo-positioners (Attocube). A dimpled tapered fibre, having a diameter of $1 \mu\text{m}$, must meet the smallest optical disk of $\sim 5 \mu\text{m}$ where this commercial product, although expensive, provides the necessary resolution (sub-nm) in a travel range of 5 mm for all three stacks (ANPz101, $2 \times$ ANPx101). Moreover, these positioners are vacuum compatible and compact, suitable for the current size of the OVC. The travel range did not cover the whole chip (~ 6 mm) but enabled access to all the torsional devices without having to re-adjust the chip.

I also mention a design flaw in the beginning, where I poorly arranged the setup such that the fibre-holder was on top of the 3-attocube stacks - making the coupling very difficult to the stationary chip due to vibrations of the fibre-taper with each piezo-step. It often landed on the substrate (void spaces) rather than the device itself due to a heavier fibre-holder (70 g) and odd geometry providing a constant small torque (not shown). Although the weight of the fibre-holder should not be an issue, being under the maximum load of 200

g, the nanopositioners performance seemed to have degraded over time. From this lesson, the Attocube stacks have been rearranged from xyz to zxy , from top to bottom, supporting the chip (5 g) while the fibre-holder stays rigid using an I-beam. Alignments were far better with this configuration where a dimpled fibre-taper could hover over a disk for evanescent coupling.

3.2.5 Fibre-holder

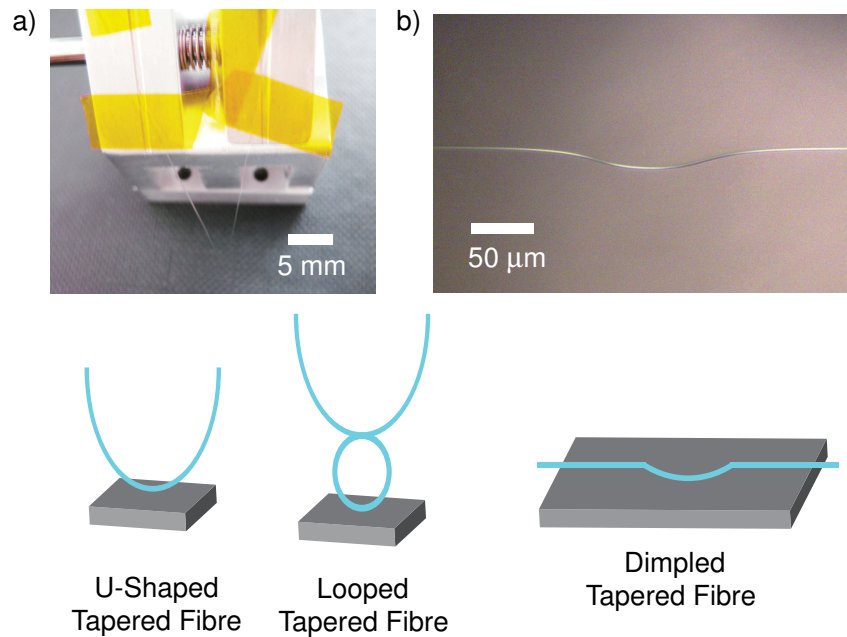


Figure 3.10: Tapered fibres in a) u-shaped and b) dimpled-shaped structures to approach micron-scale devices on a 2D-chip with three possible methods illustrated below.

The first generation of fibre-holder was a u-holder which has a lowest spot from a u-shaped fibre for on-chip coupling, partially shown in Fig. 3.10a. It was an extremely difficult task to pick up the fibre by hand, place the fibre in the u-holder groove, and mount it with Kapton tape. In most cases, the fibre broke as soon as I tried to handle them; however, I have managed to put a tapered fibre in a u-shaped form upon many iterations and practices. The depressing part was that this fibre was no good for commercially made optomechanical experiments since the fibre was mechanically unstable, making it hard to couple into any optical structures. The lowest spot was also very broad to do any coupling since the lowest-region of the tapered fibre is much larger than the void space around a device ($\gg 100 \mu\text{m}$). All I managed to do with this u-shaped fibre was finding optical resonances of a $80 \mu\text{m}$

diameter disk which was not particularly interesting (no mechanical structures present). To overcome the floppiness and the long lowest-spot region, I needed to learn how to mould a dimple since it provides both the mechanical stability and a small lowest-region on the order of $50\ \mu\text{m}$. Working on the procedure for six months, I have developed a systematic way to fabricate dimpled tapered fibres - which is reported in the next section.

Consequently, a separate fibre-holder was needed to mount a dimpled fibre shown in Fig. 3.7, where I custom-machined fibre-holder shape of a tuning-fork to adapt the flat tensioned dimpled fibre shown in Fig. 3.7. The fibre-holder, together with I-beam, is mounted on top of the goniometer (KOHZU SH03B-DS), which provides extra degrees of freedom to ensure that the dimple is indeed the lowest spot although it is sparsely used.

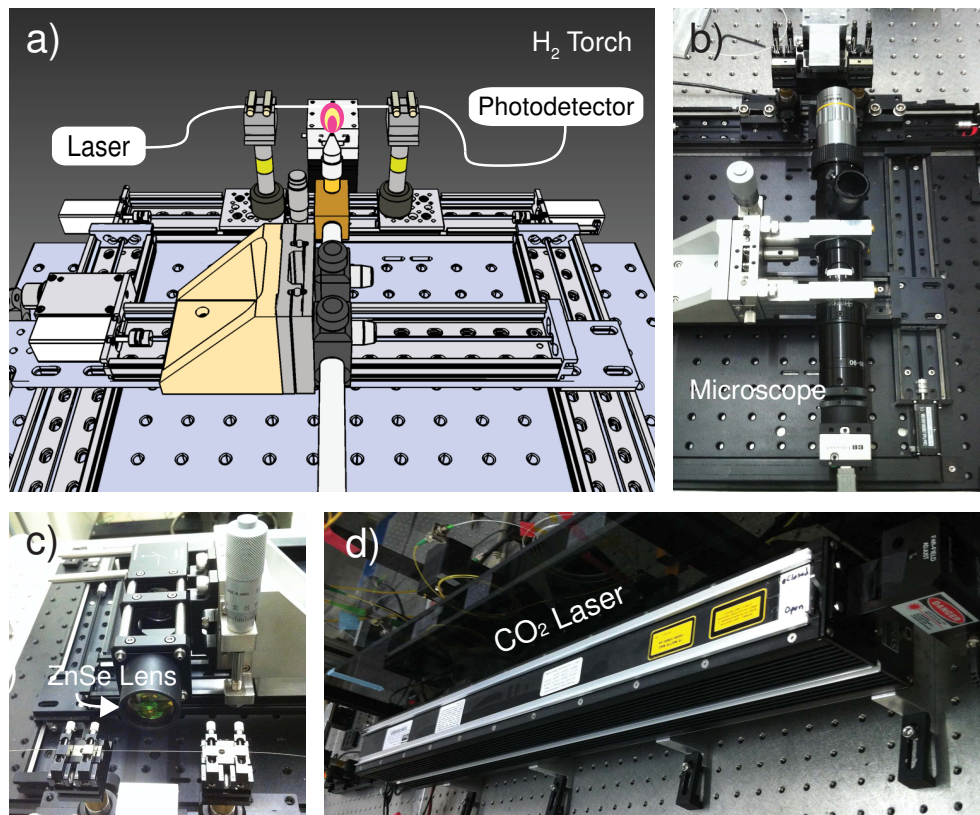


Figure 3.11: a) A CAD illustration of the computer-controlled motorized stage to taper an optical fibre using H₂ torch. b) The setup can also accommodate a microscope to monitor during the dimpling procedure precisely. c), d) Instead of the H₂ torch, the CO₂ laser can also be used to taper and dimple fibres where a ZnSe lens is used to focus the laser.

3.2.6 Tapered-fibre apparatus

Fabricating dimpled tapered fibres requires an independent setup as shown in Fig. 3.1, where half of the optical table is occupied by the fibre-puller apparatus including the CO₂ laser. The fibre-puller includes three motorized stages for various configurations shown in Fig. 3.11, where a clamped fibre can be tapered via hydrogen torch or CO₂ laser, and a fibre can be levelled prior to tapering using a microscope - taken from the OVC apparatus. The microscope is especially useful during the dimpling procedure to monitor the mould at all times. After aligning the mould to a tapered fibre, my first ever success in dimpling tapered fibres was done through a flameless CO₂ laser, shown in Fig. 3.11c, for annealing by focusing focusing carefully with the ZnSe lens (Fig. 3.11c). Although it was useful at first, I was not able to reproduce dimpled fibres as desired. Using a similar approach as above, but replacing the CO₂ laser with a small hydrogen flame and graphite, turned out to be a much better fabrication method, described in the following section.

3.3 Dimpled tapered fibres

Tapered fibres, having large evanescent fields outside the tapered region, are ideal waveguides to interact with high Q_{opt} WGM systems such as optical spheres, bottles, and toroids (50)-(52). These fibre-tapers have further been engineered, either in u-shaped (53), looped (54), or dimpled (42), to accommodate on-chip devices illustrated in Fig. 3.10 for efficient coupling. As mentioned previously (Section 3.2.5), dimple structures are superior to the u-shaped or looped fibre based on mechanical stability and small low-spot region. Following the approach in Ref. (42), the fabrication methods have been refined and optimized to reproduce dimpled tapered fibres with a high success rate.

3.3.1 Producing tapered fibres

The optical fibre must first be adiabatically tapered down to a sub-micron diameter prior to the dimpling procedure. The method of tapering fibres is obtained in a similar method to commercially fabricated optical fibres by heating and pulling. The difference is in localizing the heat to a tiny region using a one-hole stub (OX-0) in Fig. 3.12a which softens and stretches the fibre along the small taper length. We experimentally found a trend in which the multiple-holes stubs in Fig. 3.12 resulted in a very adiabatic, and long tapered region with minimum insertion losses ($< 1\%$) while the single-hole stubs gave a shorter tapered length but were more lossy (55). Although a long adiabatic taper was desirable, the single-hole stub (OX-0) was experimentally found suited for the dimpling procedure. A shorter

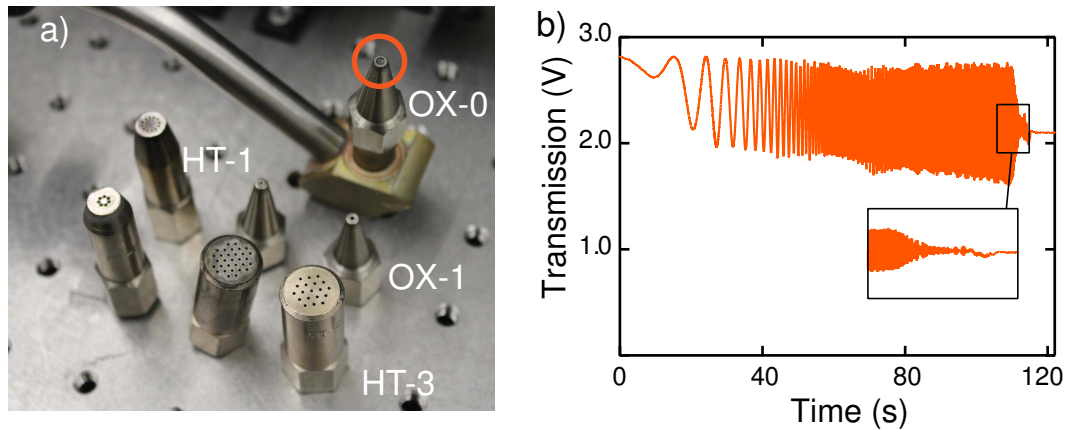


Figure 3.12: Different kinds of tips for a hydrogen torch are shown in a), where the single hole torch tip (OX-0), circled in orange, was mainly used for tapering the fibre. The graph in b) shows the typical tapering profile to reach single mode in using the OX-0 stub.

tapered region is helpful for wrapping the tapered fibre around the mould and mounting the fibre on the fibre-holder - which still has good transmission as shown in Fig. 3.12b (26 % loss). The pulling system with translation motors (Zaber T-G-LSM200A200A) was constructed with a custom controller (programmed by C. Doolin) allowing independent controls of the stage and two clamps.

The first step is to prepare an optical fibre (SMF-28e) of \sim one meter in length by stripping the coating from, and cleaving both ends, to enable mechanical splicing and stripping the middle section for tapering (\sim 1 cm). All stripped regions must be cleaned thoroughly using a triple-combination of acetone, IPA, and methanol prior to mechanical splicing and clamping. An index-matching gel aids the mechanical splicing process as the fibre ends are adjusted until a good transmission is obtained. The tapering process is highly dependent on the alignment of the fibre, such that any torque applied from a misaligned fibre will destroy the tapering process. This crucial alignment can be done using a microscope stand to view the top and the front (Fig. 3.11b) assuring a straight profile. Prior to pulling, pre-heating the fibre (until a white glow) for \sim ten seconds is a good way to clean a fibre. It is also a test to see if any noticeable bending occurs from a softened fibre without stretching. If the bending is clear, it should be replaced and re-aligned using a microscope for a straighter alignment.

The H_2 tank should read a pressure of \sim 5 psi and the flame height was adjusted to \sim 1 cm from the torch-hole using a simple valve. The torch height should also be adjusted

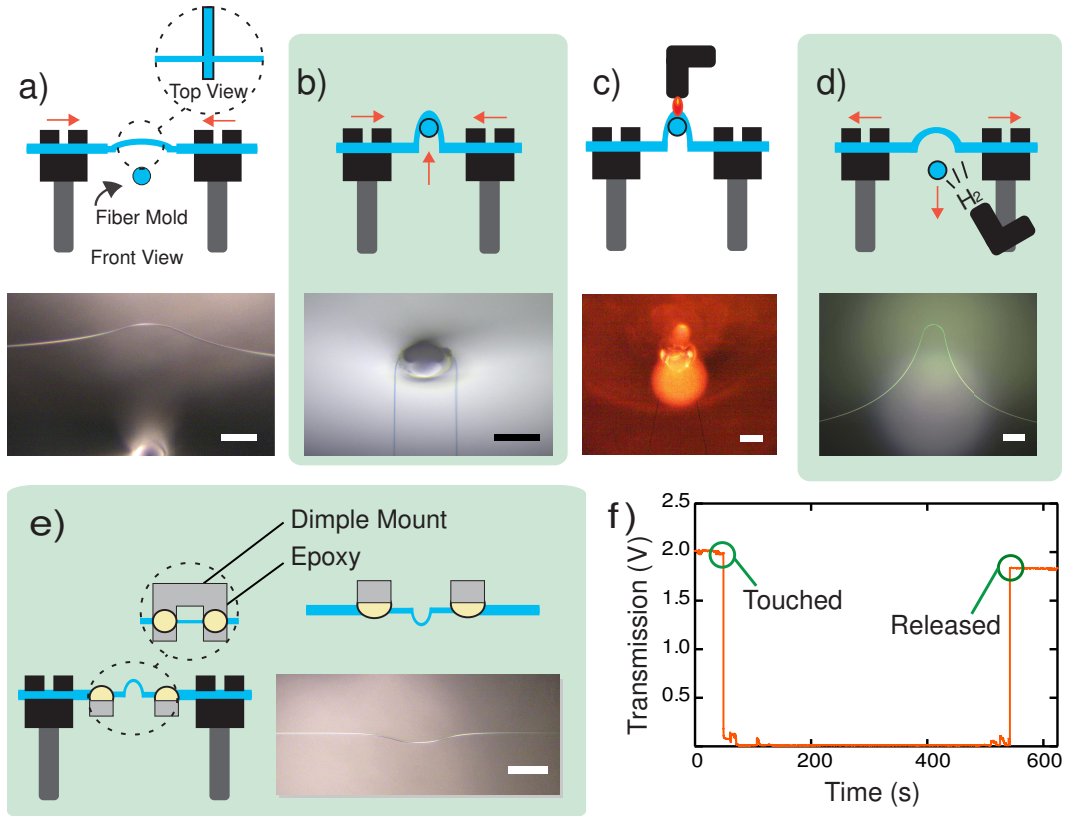


Figure 3.13: The overview of the dimpling process. First, the centre of the thinnest part of the taper is located in a) by retracting the clamps and the mould is positioned directly under it. Raising the mould while retracting the clamps is shown in b) where the bottom inset shows the ideal configuration for annealing. In c) I used a small flame upside down to mould the tapered fibre. After lowering the mould while simultaneously tensioning the fibre, the mould is brought to a point levelled with the rest of the tapered fibre. To release the mould from the tapered fibre, a small hydrogen flow from the torch was used. The mounting is depicted in e) where 5-minute epoxy was applied to attach the fibre to the fibre-holder. During the entire dimple process, the transmission was monitored in f) where 92 % was recovered after the dimple.

so that the stripped region is centred with a flame height, confirmed by a small glow in a dark room upon a flame touching the fibre - ready for pulling. The pull speed was $40 \mu\text{m}/\text{second}$ while the torch was periodically approached towards the fibre-taper in a small $1 \mu\text{m}$ increments ($\sim 50 \mu\text{m}$ in total) to compensate thinning of the fibre. Monitoring the optical transmission, a profile like Fig. 3.12b was obtained, where the pulling stopped when the transmission oscillation stopped to a single mode. Typical transmission after pulling with OX-1 is $\sim 75 \%$ with typical pull time ranging from two minutes to three minutes. If the final transmission is less than 50% of the initial transmission, which is often due to misalignment, the tapering process should be redone with realignment.

3.3.2 Dimpled fibre procedure

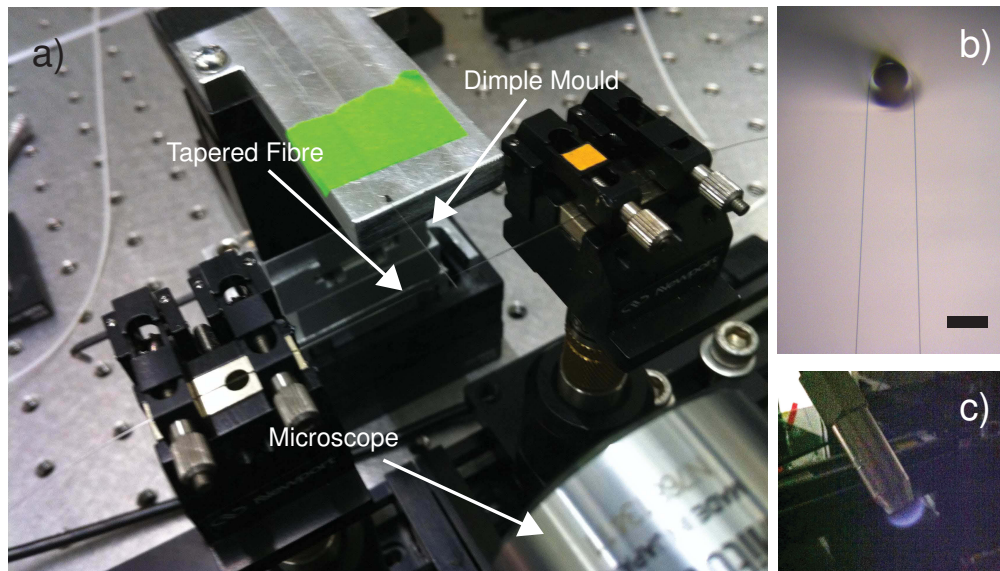


Figure 3.14: Zoomed picture of Fig. 3.11b. The setup in a) includes a dimple mould, or a cleaned stripped fibre, taped orthogonally to the tapered fibre. Raising this mould using manual positioner while detensioning the tapered fibre results in b) (with a scale bar of $125 \mu\text{m}$). Using a small flame, from the HT-1 torch-tip, the annealing process is done by dabbing the mould manually with a flame for 1 second as shown in c) and Fig. 3.13c.

After successfully tapering a fibre, a microscope is mounted, as shown in Fig. 3.11b, to proceed with the dimpling procedure - with an overview illustrated in Fig. 3.13. To prepare the mould used for dimpling, a stripped fibre was taped on a mount perpendicular to the fibre-taper with manual xyz -positioning stacks (Newport - DS25-XYZ). The stripped fibre of diameter $125 \mu\text{m}$, or the dimple-mould, should also be cleaned with acetone, IPA, and

methanol. An important step is to apply a graphite (Tube-O-Lube[®]) layer on the mould to avoid sticking after the annealing process. Graphite generally burns off with the hydrogen flame but excess graphite should be avoided because particles may still remain in a tapered fibre which is nearly impossible to remove. After applying the graphite, a Kim-wipe, or a gentle air blow, was used to brush off excess graphite.

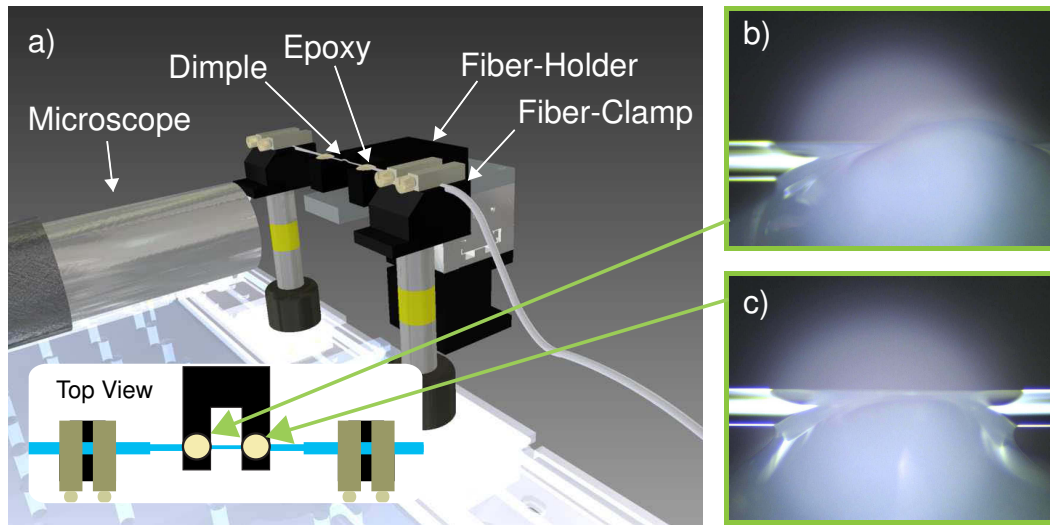


Figure 3.15: a) Rendered image of the gluing process with the 5-minute epoxy applied on the fibre-holder placed upside down. The inset show the top-view of the fibre-clamps, fibre-holder, and the dimpled tapered fibre in a simplified manner. Monitoring in real-time, the fibre-holder was raised until the epoxy touched the tapered fibre as shown in b) and c) [47].

I then retracted the clamps about $10\ \mu\text{m}$ in a single step, where the thinnest region can be spotted from the bending - and the mould is centred at this location shown in Fig. 3.13. Next the mould was raised to touch the tapered fibre in the thinnest region and continuously raised while the clamps are retracted simultaneously. During the manual process of raising and retracting, the tapered fibres should be fully tensioned at all times to wrap the tapered fibre tightly around the mould. After the mould is raised as much as possible, depicted in Fig. 3.14b, the torch-tip was replaced with the HT-1 and lit with a small flame portrayed in Fig. 3.14c upside down. The small flame is handled manually to touch the mould and the tapered fibre lightly (1 second) flashing a red glow. The reverse process of lowering the mould and tensioning the fibre-clamps are done until the mould is levelled with the tapered fibre to release the dimpled tapered fibre off the mould. This part of releasing is the most difficult part of the dimple process as it tends to break easily upon releasing. Starting with gentle H_2 gas from the torch, it is manually placed underneath the tapered fibre - where the

flow can be gradually increased until the dimpled fibre-taper separates from the mould. If a graphite was nicely coated without excess, this process should not be so difficult. Typically the overall process after the dimple recovers most of the transmission as seen in Fig. 3.13 f) with only 8 % loss in transmission. Recently I have gotten better with less than 1 % loss during the dimple procedure reported in the Appendix A.

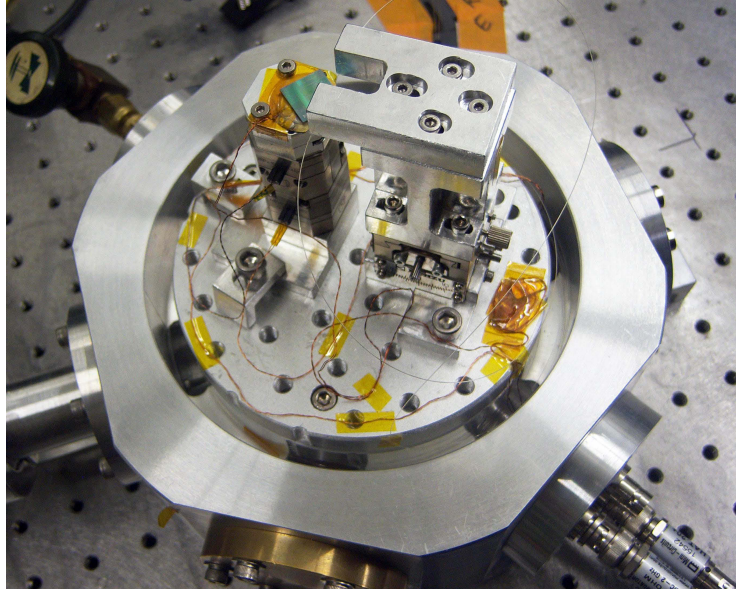


Figure 3.16: Image of the fully fusion spliced dimpled fibre assembled together with the commercially made chip awaiting pumping and optomechanical measurement.

After successfully making a dimple, as shown in Fig. 3.13d, a custom-machined adapter was placed to hold the fibre-holder upside down. A microscope was used to make sure that the fibre-holder is levelled with the tapered fibre, where additional layers of Kapton tape may be necessary for fibre-holder levelling. This step is also very important because the glue has to touch the fibre simultaneously. If the glue is touched on one side first, the uneven contact destroys the dimple by one-sided tensioning. A wooden applicator was used to mix the two components of the epoxy (Devcon 5-minute epoxy) and small droplets were applied on the inner corners of the fork. When the tapered fibre touches the glue by raising the fibre-holder, the tension in the fibre can be finally adjusted before it hardens. After waiting about 20 minutes, until fully hardened, a new mixture of the epoxy can be fully applied to the rest of the area to hold the fibre in place. I note one caution where the glue height must be shorter with respect to the dimple position. There were a few instances where the glue was taller than the dimple making it harder to couple. At this time, the goniometer was used to tilt the fibre-holder to have the dimple in a lowest spot. To avoid this problem of

glue touching the chip rather than the dimpled-fibre itself, it is important to use the wooden applicator, where excessive glue can be flattened before it hardens.

When all goes well with the above process, the dimpled fibre-taper can be transferred into OVC using the fusion-splicer (FSU 995 FA). The fusion-splicer uses two electrodes centred on the two cleaved ends of the fibre where high voltage is applied to fuse the two fibres together. This is an automated process where straight cleaved ends are required. After removing the mechanical splice from the fibre-puller apparatus, the ends of the fibre-taper are again cleaved and placed inside the fusion splicer with the other end coming from the chamber. The area provided from the fibre panel (Fig. 3.3) gives plenty of room for the fusion splicer. Losses of ~ 0.03 dB and 0.01 dB were achieved on each splice. After fully fusion spliced into the OVC, the excess fibres are wrapped around the circular plate with Kapton tape shown in Fig. 3.16. A final step is done by placing the aluminum cylinder back with appropriate vacuum grease to seal the chamber prior to pumping air out.

CHAPTER 4

Experimental Results and Discussions on Small Torsion Sensing

Work will win when wishy washy wishing won't.

- Thomas S. Monson

Having provided details of the post-processed chips (Chapter 2) and the custom-designed optomechanical vacuum chamber (Chapter 3), this chapter will now discuss the core results from the experiment, which resulted in a publication in 2013 highlighting the suitability of optomechanics in torsion sensors (36). The discussion will begin with the non-invasive calibration procedure used to accurately describe the thermally driven motions of torsion paddles. During this procedure, finite-element method (FEM) simulations were heavily used to provide the appropriate effective constants, mass (m_{eff}) and torsion spring constant (κ_{eff}), which were necessary for calibrating mechanical peaks in frequency space. Further FEM simulations were used to calculate the moment of inertia to confirm the torsion mode observed in each device. I have collected and compiled all the parameterized optomechanical devices from the commercially made chips to identify important optomechanical parameters such as disk diameter and gap size to design the next generation of optomechanical torsion devices.

4.1 Thermomechanical calibration procedure for torsion mechanics

There are diverse methods for probing different NEMS devices such as free-space optical (56), (57), tapered-fibre (58), capacitive (59), or piezoresistive measurements (60). In the

context of optomechanics where the sensitivities are enhanced by a high- Q_{opt} optical resonator, thermal motion of a chip-scale resonator are easily resolved without an external drive. Consequently the equipartition theorem, which relates the potential energy of the system to the bath temperature, is utilized to accurately extract the mechanical frequency (f_n), mechanical quality-factor (Q_{mech}), and the displacement noise-floor (z_0) of the mechanical device. The non-invasive and precise approach for thermomechanical calibration was followed from the paper by Hauer *et al* (55).

4.1.1 Johnson noise

I begin the discussion with the well-known thermal fluctuations in resistors, commonly known as Johnson noise or shot noise, derived as a special case of the fluctuation-dissipation theorem - relating the noise to the dissipation of the system (61):

$$V_{\text{rms}} = v\sqrt{\text{BW}} = \sqrt{4k_B T R \text{BW}}. \quad (4.1)$$

Here, the V_{rms} is the root-mean-square voltage noise density [V], v is the constant voltage white noise [$\text{V}/\sqrt{\text{Hz}}$] within the measurement bandwidth (BW) [Hz], k_B is the Boltzmann constant [J/K], T is the temperature [K], and R is the resistance [Ω]. Since the origin of the voltage fluctuations comes from the mechanical vibrations of electrons in resistors under thermal equilibrium, we will see that Eqn. 4.1 is highly analogous to the thermal forces in NEMS devices.

4.1.2 Equations of motion

The dynamics of mechanical resonators can be modelled from the damped harmonic oscillator equation. My devices, being a torsional one, I also include the angular version of the harmonic oscillator model:

$$\ddot{z}_n(t) + \frac{\Omega_n}{Q_{\text{mech},n}} \dot{z}_n(t) + \Omega_n^2 z_n(t) = \frac{F(t)}{m_{\text{eff},n}} \quad (4.2)$$

$$\ddot{\theta}_n(t) + \frac{\Omega_n}{Q_{\text{mech},n}} \dot{\theta}_n(t) + \Omega_n^2 \theta_n(t) = \frac{\tau(t)}{I_{\text{eff},n}} \quad (4.3)$$

where $z_n(t)$ ($\theta_n(t)$) is the linear (angular) displacement, Ω_n is the angular mechanical frequency, $Q_{\text{mech},n}$ is the mechanical quality factor, $F(t)$ ($\tau(t)$) is the force (torque) applied to the resonator, and $m_{\text{eff},n}$ ($I_{\text{eff},n}$) is the effective mass (moment of inertia) for a particular mechanical mode n . The $m_{\text{eff},n}$ used in Eqn. 4.2 is an actual mass weighted by a mechanical mode shape (n), which is an important parameter for calibration (Section 4.1.4.3). The same

goes for $I_{\text{eff},n}$ but later we will use the torsion spring constant $\kappa_{\text{eff},n}$ instead to be consistent with previously reported literature (14), (62). Applying a Fourier transform to Eqns. 4.2 and 4.3 in frequency space they become

$$-\Omega^2 z_n(\Omega) - \frac{\Omega\Omega_n}{Q_{\text{mech},n}} z_n(\Omega)i + \Omega_n^2 z_n(\Omega) = \frac{F(\Omega)}{m_{\text{eff},n}} \quad (4.4)$$

$$-\Omega^2 \theta_n(\Omega) - \frac{\Omega\Omega_n}{Q_{\text{mech},n}} \theta_n(\Omega)i + \Omega_n^2 \theta_n(\Omega) = \frac{\tau(\Omega)}{I_{\text{eff},n}}. \quad (4.5)$$

Rearranging Eqns. 4.4 and 4.5,

$$z_n(\Omega) = \frac{F(\Omega)}{m_{\text{eff},n}(\Omega_n^2 - \Omega^2 - i\Omega\Omega_n/Q_{\text{mech},n})} \quad (4.6)$$

$$\theta_n(\Omega) = \frac{\tau(\Omega)}{I_{\text{eff},n}(\Omega_n^2 - \Omega^2 - i\Omega\Omega_n/Q_{\text{mech},n})}, \quad (4.7)$$

we can relate the displacement to the forcing term by

$$z(\Omega) = \chi(\Omega)F(\Omega), \quad (4.8)$$

where the generalized susceptibilities are

$$\chi_z(\Omega) = \frac{1}{m_{\text{eff},n}(\Omega_n^2 - \Omega^2 - i\Omega\Omega_n/Q_{\text{mech},n})} \quad (4.9)$$

$$\chi_\theta(\Omega) = \frac{1}{I_{\text{eff},n}(\Omega_n^2 - \Omega^2 - i\Omega\Omega_n/Q_{\text{mech},n})}. \quad (4.10)$$

4.1.3 Power spectral densities

From the apparatus observed in Fig. 3.2, AC transmission collected from the photodiode provides an oscillating voltage transmission where the mechanics from the optomechanical system are embedded. Applying a frequency sweep function in a lock-in amplifier, or a spectrum analyzer, it provides a mechanical spectrum of the motions in terms of centre frequencies (f_0) and Q_{mech} with a measurement BW. The raw data of the spectrum, shown in Fig. 4.1, can be turned into power spectral density (PSD) voltage ($S_{\text{vv}}^{\text{exp}}$) by squaring the voltage spectrum (V_{exp}) normalized by the bandwidth (BW) (56):

$$S_{\text{vv}}^{\text{exp}} = \frac{V_{\text{exp}}^2}{\text{BW}}, \quad (4.11)$$

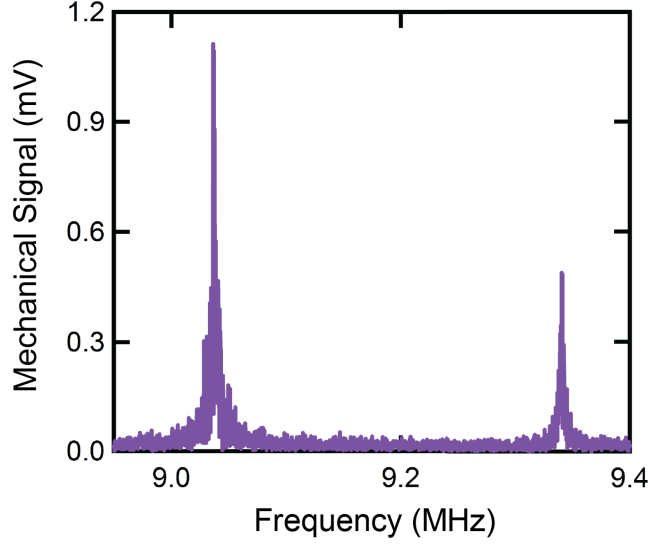


Figure 4.1: Raw data for the mechanical frequency spectrum observed for a torsional device using the optomechanical transduction obtained at the side of the optical resonance.

which provides a constant white thermal noise and the peak as

$$S_{\text{vv}}^{\text{exp}}(f) = S_{\text{vv}}^{\text{nf}} + \alpha S_{zz}(f) \quad (4.12)$$

$$S_{\text{vv}}^{\text{exp}}(f) = S_{\text{vv}}^{\text{nf}} + \beta S_{\theta\theta}(f). \quad (4.13)$$

Here, $S_{\text{vv}}(f)$ is the voltage power spectral density, $S_{\text{vv}}^{\text{nf}}$ is the constant noise-floor, α (β) are the conversion factors in unit $[\text{V}^2/\text{m}^2]$ ($[\text{V}^2/\text{rad}^2]$), and $S_{zz}(f)$ ($S_{\theta\theta}(f)$) is the linear (angular) displacement PSD. The expressions of displacement PSD's ($S_{zz}(f)$, $S_{\theta\theta}(f)$) are derived thoroughly in Hauer *et al.* (55). From the mean-square amplitude of the oscillator's motion,

$$\langle z_n^2(\Omega) \rangle = \frac{1}{2\pi} \int_0^\infty d\Omega S_{zz}(\Omega), \quad (4.14)$$

the PSD version of Eqn. 4.8 can be applied

$$S_{zz}(\Omega) = |\chi_z(\Omega)|^2 S_{\text{FF}}^{\text{th}}, \quad (4.15)$$

where the force PSD are assumed constant by thermal forces $S_{FF}(\Omega) = S_{FF}^{\text{th}}$. The integral in Eqn. 4.14 can be evaluated while the left term can be related to the equipartition theorem,

$$\langle U_n \rangle = \frac{1}{2} k_B T = \frac{1}{2} m_{\text{eff}} \Omega_n^2 \langle z_n^2(\Omega) \rangle, \quad (4.16)$$

providing the constant Brownian force as

$$S_{\text{FF}}^{\text{th}} = 4k_B T m_{\text{eff},n} \frac{\Omega_n}{Q_{\text{mech},n}}. \quad (4.17)$$

This is very similar to the Johnson noise expression in Eqn. 4.1, where R is replaced by the dissipation rate ($\sim \gamma = \Omega_n/Q_{\text{mech},n}$). Substituting the derived constant thermal force (Eqn. 4.17) back to Eqn. 4.15 results in a displacement PSD as the following:

$$S_{\text{zz}}(\Omega) = \frac{4k_B T \Omega_n}{m_{\text{eff},n} Q_{\text{mech},n} ((\Omega^2 - \Omega_n^2)^2 + (\Omega \Omega_n / Q_n)^2)} \quad (4.18)$$

$$S_{\theta\theta}(\Omega) = \frac{4k_B T \Omega_n}{I_{\text{eff},n} Q_{\text{mech},n} ((\Omega^2 - \Omega_n^2)^2 + (\Omega \Omega_n / Q_n)^2)}. \quad (4.19)$$

Expressed in terms of frequency, $f = \Omega/2\pi$, and effective torsion spring constant, $\kappa_{\text{eff}_n} = I_{\text{eff}_n} \Omega_n^2$, the equivalent expression can be found:

$$S_{\text{zz}}(f) = \frac{k_B T f_n}{2\pi^3 m_{\text{eff},n} Q_{\text{mech},n} ((f^2 - f_n^2)^2 + (f f_n / Q_{\text{mech},n})^2)} \quad (4.20)$$

$$S_{\theta\theta}(f) = \frac{2k_B T f_n^3}{\pi \kappa_{\text{eff},n} Q_{\text{mech},n} ((f^2 - f_n^2)^2 + (f f_n / Q_{\text{mech},n})^2)}. \quad (4.21)$$

Substituting Eqns. of 4.20 and 4.21 to 4.12 and 4.13, we arrive at the theoretical model used to fit the experimental PSD for torsional devices:

$$S_{\text{vv}}^{\text{exp}}(f) = S_{\text{vv}}^{\text{nf}} + \frac{A f_n}{Q_{\text{mech},n} ((f^2 - f_n^2)^2 + (f f_n / Q_{\text{mech},n})^2)} \quad (4.22)$$

$$S_{\text{vv}}^{\text{exp}}(f) = S_{\text{vv}}^{\text{nf}} + \frac{B f_n^3}{Q_{\text{mech},n} ((f^2 - f_n^2)^2 + (f f_n / Q_{\text{mech},n})^2)}, \quad (4.23)$$

where $S_{\text{vv}}^{\text{nf}}$, f_n , $Q_{\text{mech},n}$, $A = \alpha k_B T / 2\pi^3 m_{\text{eff}}$, $B = 2\beta k_B T / \kappa_{\text{eff}} \pi$ are the four fit-parameters. From the parameter A using the simulated effective mass (m_{eff}) of a particular mode, we can extract the conversion factor α and likewise with β using B and κ_{eff} :

$$\alpha = \frac{2\pi^3 m_{\text{eff}} A}{k_B T} \quad (4.24)$$

$$\beta = \frac{\kappa_{\text{eff}} \pi B}{2k_B T}. \quad (4.25)$$

These conversion factors, α and β , were used to calibrate linear and angular noise-floors

S_{vv}^{nf} .

$$S_{zz}^{\text{nf}} = \frac{S_{vv}^{\text{nf}}}{\alpha} \quad (4.26)$$

$$S_{\theta\theta}^{\text{nf}} = \frac{S_{vv}^{\text{nf}}}{\beta}. \quad (4.27)$$

The root-square displacement noise-floor, or minimum detectable signal, can be found by $\sqrt{S_{zz}(f)} = S_z(f)$ and $\sqrt{S_{\theta\theta}(f)} = S_\theta(f)$ in units $[\text{m}/\sqrt{\text{Hz}}]$ and $[\text{rad}/\sqrt{\text{Hz}}]$. Reported displacement sensitivities of torsional device were on the order of $\sim \text{fm}/\sqrt{\text{Hz}}$ (62), (63) where the purpose of this project was to demonstrate even better sensitivities on smaller torsional devices using thermally resolved optomechanical systems.

So far, I have included both expressions for spectral densities in the linear and angular case but they are related assuming the small angle approximation, $\theta \sim z/(w/2)$, by

$$S_{\theta\theta}(f) = \frac{4}{w^2} S_{zz}(f) \quad (4.28)$$

where w is the width of the simple torsion paddle (Fig. 2.1).

4.1.4 Simulation

Mode identification is important prior to any calibration. To achieve this, I have used *COMSOL* software to simulate the device's mechanical eigenfrequencies. Since torsional oscillators are intrinsically sensitive to moment of inertia, this was used to confirm the torsional mode, supporting the claim by the eigenfrequency simulations. After identifying the torsional mechanical mode, I have again used *COMSOL* to independently generate effective masses and torsion spring constants to calibrate each device - showing consistent results.

4.1.4.1 Mode identification

Using primarily the structural mechanics module in *COMSOL*, I have carefully constructed models to replicate the exact structures taken from SEM images. To accomplish this, I have magnified images of the paddle structures and scaled each dimensions of the paddles by pixel using *Adobe photoshop* software and compared it with the scale bar of the image. For example, the initially designed $10 \mu\text{m}$ disk diameter resulted in $9.67 \mu\text{m}$ showing slight deviation occurred in the fabrication process. The resolution of the exact dimensions were ultimately limited by the SEM resolution. I was able simulate mechanical modes that match accurately to the experimental data as a result. For simulations, I have used the built-in

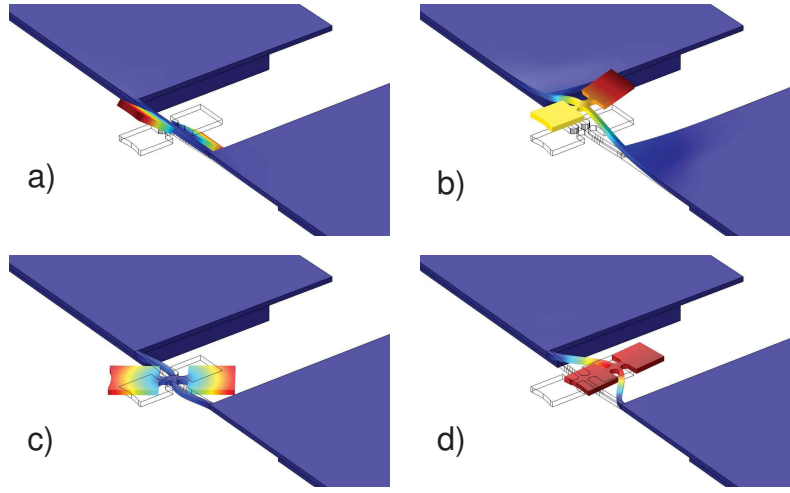


Figure 4.2: The first four eigenmodes of the torsion paddle system simulated from COMSOL with a) out-of-plane torsional mode, b) flexural mode, c) in-plane torsional mode, and d) in-plane mode with frequencies of 9.04 MHz, 13.62 MHz, 17.40 MHz, and 17.72 MHz respectively.

material of single crystal silicon with appropriate properties of the density (2329 kg/m^3) and Young's modulus (170 GPa) consistent with Ref. (64).

After using an extremely fine mesh for the simulation, I have found four fundamental frequencies of 9.04 MHz, 13.62 MHz, 17.40 MHz, and 17.72 MHz captured in Fig. 4.2. Comparing the simulated frequencies with real data in the nine optomechanical devices, the first two peaks near 9 MHz and 9.3 MHz were always observed and determined to be the torsional and the out-of-plane flexural mode, respectively. The discrepancy in the 13.62 MHz out-of-plane mode can be explained by an hybridization of two modes caused by an over-hang in the posts during the wet-etch process. I have tested these modes in another set-up, described in Section 4.3.2, to confirm this. There is also an additional third peak that appears inconsistently with the devices with a range of frequencies (11 MHz \sim 13 MHz) and relative amplitudes. Although I suspect that this third mode near 12 MHz is related to the in-plane motion (Fig. 4.2c,d), I was not able to confirm this due to discrepancies among devices. An example of this peak is included in Section 4.3.3. Before drawing any conclusions on the first peak's identity, additional simulations were done using the moment of inertia calculations.

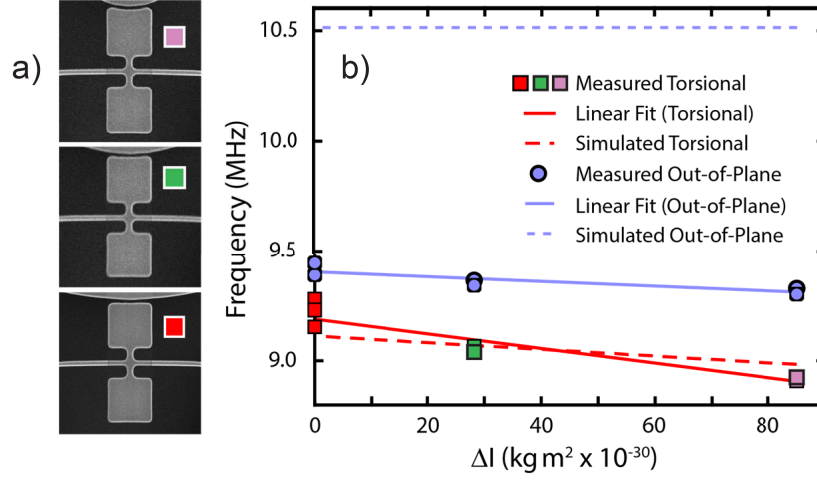


Figure 4.3: a) SEM images of the fabricated devices with 5 μm (purple), 10 μm (green), and 20 μm (red) diameter disks. b) The predicted frequencies calculated through FEM (dashed lines) and measured frequencies (markers, solid lines are linear fits) of devices with varying sized optical disks are plotted against the change in moment of inertia calculated from the modelled geometries.

4.1.4.2 Moment of Inertia

As mentioned earlier, the torsional mode should respond strongly to changes in the moment of inertia of the system. Due to the three different disk sizes used in this experiment, the evanescently coupled torsion paddles also have slightly different geometries from the curvature of the disk (recall Fig. 2.5). These caused slight changes in the moment of inertia, which were calculated from *COMSOL* using the general expression for the moment of inertia:

$$I = \int dV \rho (x^2 + y^2 + z^2). \quad (4.29)$$

From the moment of inertia calculations for the three different curvatures of the torsion paddles (Fig. 4.3), the experimental data followed the same trend as the simulations where the first peak was sensitive to the changes in the moment of inertia while the second peak stayed nearly the same. Now that the first experimental mode is properly identified as the torsional mode, the calibrations can now proceed.

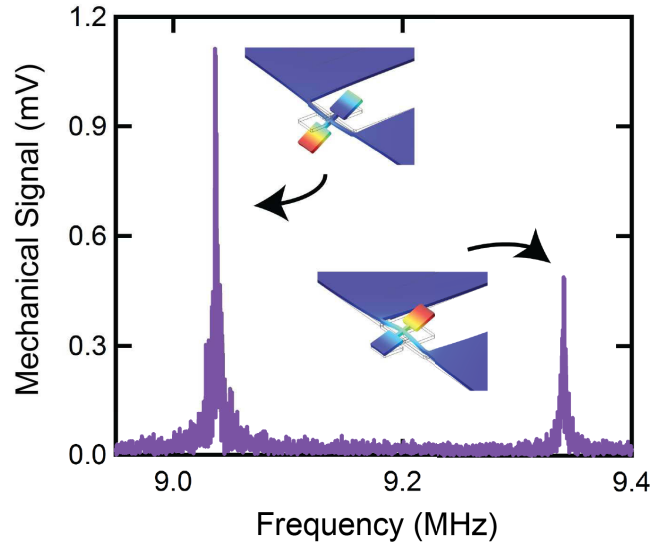


Figure 4.4: Based on the eigenfrequency and moment of inertia simulations, the peaks in Fig. 4.1 are identified as the torsional mode (left) and the flexural mode (right).

4.1.4.3 Effective constants

The effective torsion spring constants, κ_{eff} , and effective masses, m_{eff} , were each found through FEM simulations using the structural mechanics module but adding different physics to the simulations: stationary mode for κ_{eff} and eigenfrequency mode for m_{eff} . In the early stage of the experiment, I have simulated effective torsion spring constants for calibration (14), (62). Since the publication of Hauer *et al.* (55), the consistent effective mass approach became highly favourable - being simple and widely applicable for other mechanical modes.

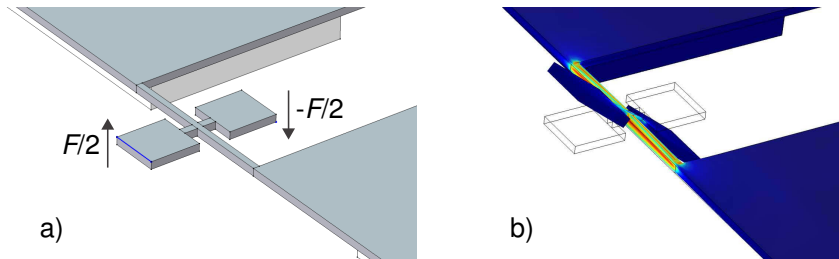


Figure 4.5: FEM simulations used to apply a torque to find the effective torsion spring constant. a) The edge load of $\pm F/2$ was applied at opposite ends of the paddle, b) resulting in a torque.

Starting with the effective torsion spring constant, I applied an edge load (under solid mechanics module) on both ends with equal and opposite forces in the stationary mode to torque the paddle. For this method, the geometries had to be simple and symmetric to apply the torque evenly to avoid complications to the simulation. Therefore, the GDS designed dimensions were used instead of the fabricated dimensions shown in Fig. 4.5. By applying a manual torque corresponding vertical displacements were obtained. Based on the definition of torque, $\boldsymbol{\tau} = \mathbf{r} \times \mathbf{F}$, and the angular form of Hooke's law, $\tau = \kappa\theta$, the torsion spring constant is expressed as

$$\kappa_{\text{eff}} = \frac{w^2 F}{4z}. \quad (4.30)$$

For example, I applied an edge load of $\pm 0.5 \mu\text{N}$ on both ends to make total force (F) of $1 \mu\text{N}$, width (w) was $4 \mu\text{m}$, and the simulated z was $0.404 \mu\text{m}$ resulting in $\kappa_{\text{eff}} = 9.91 \times 10^{-12} \text{ Nm/rad}$. Using this value, β in Eqn. 4.24 was found for further calibration.

The effective mass approach uses exact shapes of a device, providing more accurate simulation of these constants. All it requires is to evaluate a volume integral and maximum displacements after the mode simulation. The definition of effective mass has some freedom in its choice but the following normalized definition was used to generalize to all mechanical shapes and modes (55):

$$m_{\text{eff}} = \rho \int dV \frac{|\mathbf{r}_n|^2}{|\mathbf{r}_{n,\text{max}}|^2}, \quad (4.31)$$

where ρ is the uniform density, \mathbf{r}_n is the displacement for a particular mode n , and $\mathbf{r}_{n,\text{max}}$ is the maximum displacement. After doing the mode simulation shown in Fig. 4.2, the volume integral (Eqn. 4.31) was evaluated for each eigenmode to obtain its effective mass. The effective mass for the torsional device was 0.74 pg and for the flexural mode was 1.38 pg , which are smaller than the recently reported torsional device ($\sim 13.05 \text{ pg}$) (62). The calibration for all of the nine devices was done primarily using the effective mass, and they are shown in Section 4.2.2.

4.2 Experimental data

So far I have discussed the simulation and the calibration methods for a given optically transduced mechanical mode, as seen in Fig. 4.4, where I can accurately identify the mechanical modes and further calibrate the torsional mode using either effective constant (κ_{eff} or m_{eff}). In optomechanical experiments each mechanical resonance has a different sensitivity based on various factors, namely optical modes, optomechanical coupling, and Q_{opt} . This section describes the experimental procedure to optimize the optomechanical signals to obtain the best data possible in a device using a lock-in amplifier. Each of the nine

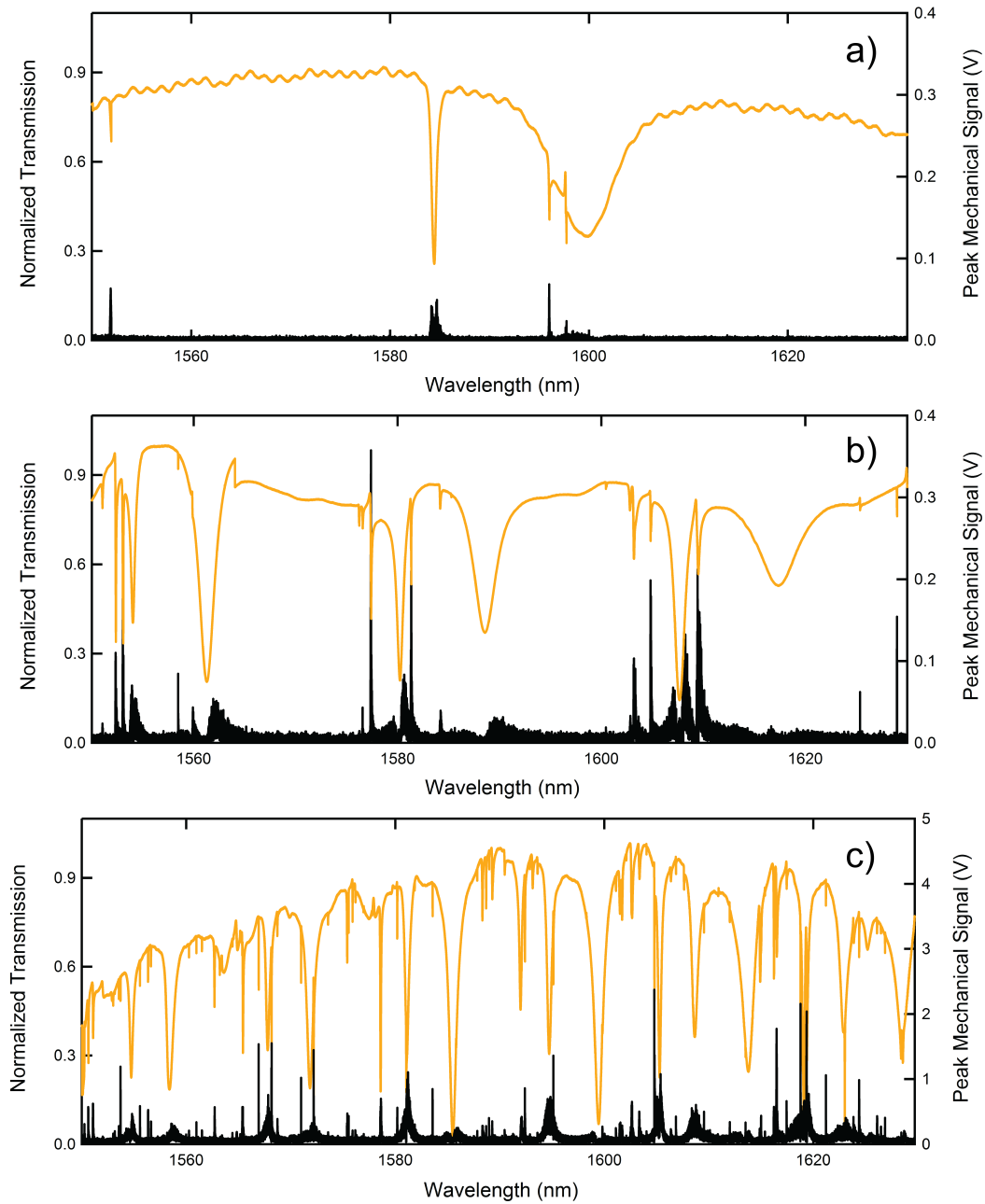


Figure 4.6: The data from the lock-in technique, where the wavelength is scanned over the whole tunable range (1550 nm \sim 1630 nm), with optical resonances shown as a dip in the transmission (orange) while the fundamental mechanical frequency is locked near 9 MHz with 100 Hz bandwidth (black). The optical data were normalized to the background scan (without coupling). The three plots correspond to a) 5 μm , b) 10 μm , c) and 20 μm diameter disks coupled to torsional oscillators with the smallest gap of \sim 130 nm. During the measurement, the dimpled tapered fibre was touching the optical disk.

devices were optimized and summarized in this section with accurate calibration of their noise-floors.

4.2.1 Optical resonator

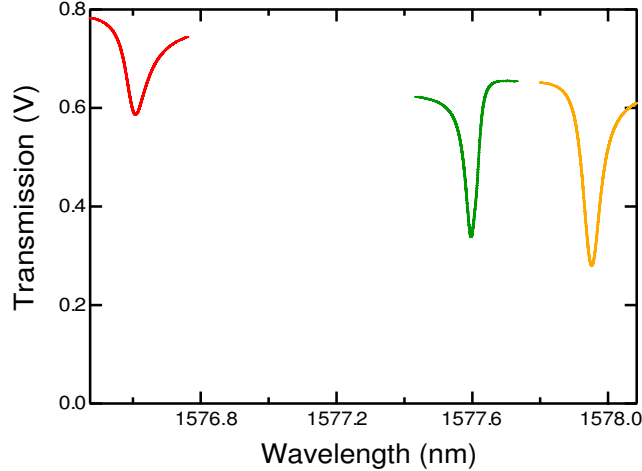


Figure 4.7: Three devices, each with a $10 \mu\text{m}$ diameter disk but with varying gaps between the disk and the mechanical structure, show the variation of the optical resonance near 1577 nm . The red resonance is the smallest gap (100 nm) with Q_{opt} of $19,990$, yellow having gap of 180 nm with Q_{opt} of $25,500$, and green resonance having the largest gap (230 nm) having $37,780$. Therefore we conclude that an increase in the gap between the optical and the mechanical resonator increases the Q_{opt} .

There are three different microdisk diameters, $5 \mu\text{m}$, $10 \mu\text{m}$, and $20 \mu\text{m}$, each of which have different optical profiles, as shown in Fig. 4.6. Since the mechanical detection is based on the optically enhanced detection through a WGM microdisk, the optical properties of these devices are highly important. The optical quality factor, in the high-Q limit, is defined as

$$Q_{\text{opt}} = \frac{\omega_0}{\Delta\omega} \quad (4.32)$$

where ω_0 is the optical resonance frequency and $\Delta\omega$ is the optical linewidth at full-width half-max. These two quantities, ω_0 and $\Delta\omega$, are found by fitting an optical resonance to the Lorentzian line-shape:

$$L(\omega) = \frac{\frac{1}{2}\Delta\omega}{(\omega - \omega_0)^2 + (\frac{1}{2}\Delta\omega)^2}. \quad (4.33)$$

Q_{opt} is simply a measure of a photon lifetime ($\sim 1/\Delta\omega$), or dissipation rate ($\sim \Delta\omega$), in an optical resonator. In principle a higher Q_{opt} will result in enhanced detection as other

groups have demonstrated using high quality optical resonators ($Q_{\text{opt}} > 10^6$) in Refs. (25), (65), and (66).

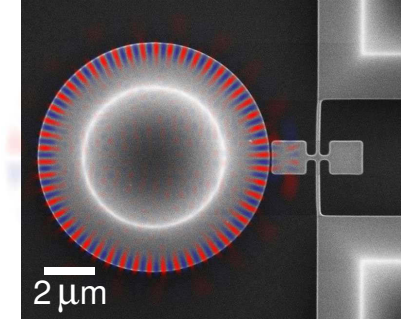


Figure 4.8: SEM micrograph of the optomechanical torsion designs overlaid with a simulation of the optical mode showing evanescent coupling between the two oscillators (optical and mechanical).

My devices, in comparison with the reported Q_{opt} of 5×10^6 in SOI bare-microdisks (65), have only moderate Q_{opt} for two main reasons: evanescently coupled torsion paddle and the fibre touching the disk scattering optical power in the cavity. Based on the three gaps presented, the smallest gap almost always resulted in a larger optical dissipation. For example for the $10 \mu\text{m}$ diameter disk, the three gaps of $\sim 130 \text{ nm}$, 180 nm , and 230 nm gave Q_{opt} of 19,990, 25,500, and 37,780, respectively, for the same optical resonance while keeping the laser power and the polarization the same as shown in Fig. 4.32. Therefore within the same mode volume, it is clear that torsional device dissipates the optical power based on the gap. I also touched the disk with the dimpled tapered fibre to avoid low frequency mechanical noise caused from the fibre. Hovering above the disk generally provides better Q_{opt} but is harder to perform experimentally. For the hovering configuration, the tapered fibre needs to be highly tensioned to avoid optical gradient forces pulling the fibre to the disk, but there are still added mechanical noise in the system. From the calibrated results, noise-floors are generally higher for the hovering case, where a particular device touched by a fibre (Fig. 4.8) shows the sensitivity is five times better when hovering. Although hovering is achievable in our setup, I preferred the touched configuration for mechanical stability at a cost of generating higher order optical modes and slightly lower Q_{opt} .

However Q_{opt} is just one parameter; the optomechanical coupling strength is equally important. Since the paddle dimensions are nearly the same in all nine devices, the smaller disk diameter should give the largest coupling due to the larger optical mode overlap with the mechanical mode than larger microdisks. However the Q_{opt} for $5 \mu\text{m}$ diameter disk is much lower in the order of $\sim 10^3$ due to surface effects and the higher curvature of the WGM disk.

The competing effects between the energy stored in the resonator and the optomechanical coupling is highly important.

From the optical properties point of view, my optomechanical devices may not seem as attractive as other optomechanical systems - cleverly designed to overlap optical and mechanical modes to achieve high Q_{opt} and large G devices (65),(67). However, there are some benefits to weakly coupled designs. First, the thermo-optic heating from the high Q_{opt} optical cavity does not affect the coupled mechanical structures due to the separation of these resonators. Second, the paddles can be functionalized and modified without contaminating the optical properties of the disk, which can be highly applicable in sensing applications. I have worked towards with a recipe to deposit patterned layers of gold onto a paddle for applications in molecule sensing (see Appendix C).

4.2.2 Optimization of mechanical data

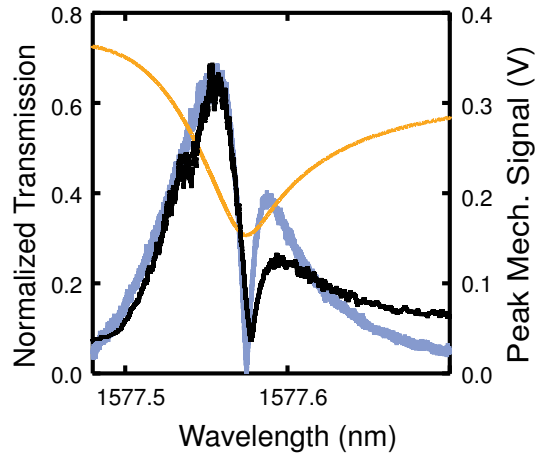


Figure 4.9: Fine wavelength scan (orange) of the optimized optical resonance near 1577 nm based on Fig. 4.6b. The numerically calculated slope (lavender) of the optical resonance qualitatively agrees well with the locked mechanical amplitudes (black).

For each of the nine devices, thermal motion of the first few peaks was easily observed without external actuation. Using any optical resonance present in a microdisk, I could always find mechanical peaks similar to these in Fig. 4.1. Locking the torsional mode frequency around a small bandwidth of 100 Hz using the lock-in amplifier, I can monitor the peak mechanical amplitude (at 9.03 MHz) while sweeping the laser wavelength. The data observed in Fig. 4.6, shows the mechanical peak amplitude with the corresponding optical resonances of

the 5 μm , 10 μm , and 20 μm diameter microdisks. The mechanical amplitude voltages were maximized to identify the best optical resonance that contains the largest peak, hence the best coupling. Scanning that optical resonance with finer resolution and further optimizing the FPC and the VOA, I found the best spot for the highest mechanical signal without introducing bistability of the optical resonance, as seen in Fig. 4.9. The numerical derivative, or the slope of the optical resonance, shows good qualitative agreement with the detected mechanical signal.

Device	Diameter (μm)	Q_{opt}	Gap (μm)	f_0 (MHz)	Q_{mech}	S_z^{nf} (fm/Hz ^{1/2})
C04	4.85	4310	0.12	8.91	3670	37
C05	4.80	7180	0.19	8.91	7180	80
C06	4.76	7960	0.24	8.92	3430	71
C10	9.67	14200	0.10	9.04	3750	7
C11	9.60	45700	0.19	9.06	3050	51
C12	9.63	15130	0.26	9.04	2810	75
C19	19.58	58620	0.10	9.15	3450	22
C20	19.24	30500	0.16	9.28	4660	64
C21	19.39	33230	0.24	9.24	3429	83

Table 4.1: Tabulated experimental results for all nine devices of the torsion paddle with torsion rod length of $\sim 5 \mu\text{m}$.

I have optimized the optomechanical signal from all the torsion paddle devices using the above lock-in technique, summarized in Table 4.1. Comparing these calibrated noise-floors, the best sensitivity of these devices was obtained with the 10 μm diameter microdisk with $\sim 100 \text{ nm}$ gap between the optical and the mechanical resonator, demonstrating noise-floor down to $7 \text{ fm}/\sqrt{\text{Hz}}$.

In addition to the table, Fig. 4.10 shows a comprehensive plot of the trends in the noise-floor with respect to the disk diameter and the gap between the optical and mechanical resonators. The trend in noise-floor with gap (Fig. 4.10b) is easy to understand as smaller gaps should result in better coupling due to greater overlap between the mechanical resonator and the evanescent optical field. This is limited by the feature resolution in nanofabrication with EBL techniques and stiction problems. As for the disk diameters, higher sensitivities occur at 10 μm due to trade-off between optical mode-volume and coupling strength. The smallest disk should have the largest coupling strength since the torsional resonator is comparable in size to the microdisk, however the large curvature in a small disk is more susceptible to the

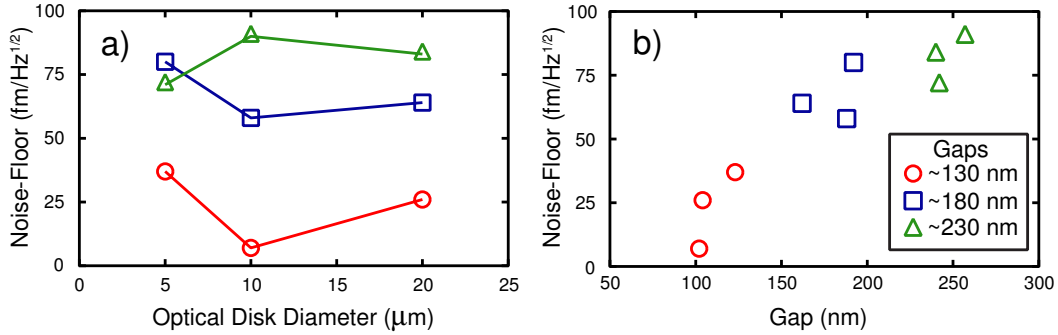


Figure 4.10: Comprehensive plots for all nine optomechanical torsion devices presented to show a trend in a) optical disk diameter and the b) gap between the optical cavity and torsional oscillator. Lines are guides to the eye and trends are explained in the text.

surface effects of the microdisk which can increase scattering as is evident from smaller Q_{opt} in Table 4.1. Also there a smaller number of resonances to work with, as seen in Fig. 4.1a and hence the 10 μm diameter seems to be the best cavity out of the nine optomechanical structures. Note that the noise-floor errors from the fit are too small ($\sim \pm 2 \text{ fm}/\sqrt{\text{Hz}}$) to display in Fig. 4.10.

4.2.3 Mechanical spectrum for the most sensitive device

The plots shown in Fig. 4.11 are the optimized and properly calibrated data for the best optomechanically transduced torsion device (36). The device has an angular sensitivity of $4 \text{ nrad}/\sqrt{\text{Hz}}$ and equivalent displacement sensitivity of $7 \text{ fm}/\sqrt{\text{Hz}}$, comparable to other optomechanical systems (35), (68), confirming that optomechanical platform is excellent for small mass torsional devices. From the benefit of the torsional motion, a lot of interesting magnetic systems and molecule dynamics can be probed using optomechanics.

The conversion factors, $\alpha = 1.24 \times 10^{16} \text{ V}^2/\text{m}^2$ and $\beta = 5.12 \times 10^4 \text{ V}^2/\text{rad}^2$, were found from independent calibration methods using m_{eff} and κ_{eff} , respectively, resulting in a consistent noise-floor result of $6.81 \text{ fm}/\sqrt{\text{Hz}}$ and $6.76 \text{ fm}/\sqrt{\text{Hz}}$. The published graph in Fig. 4.11a, shows the noise-floor above $10 \text{ fm}/\sqrt{\text{Hz}}$ in contrast to the calibrated noise-floor of $7 \text{ fm}/\sqrt{\text{Hz}}$ (36). This was simply due to the narrow range used for the sweep, where I have swept larger frequency ranges ($\sim 400 \text{ kHz}$ span) at a later date on the same device shown in Fig. 4.11b - showing the noise-floor reaching the reported sensitivity. I note that the figure was slightly smoothed to properly fit the PSD voltage. I will call this optimized device as C10, referring

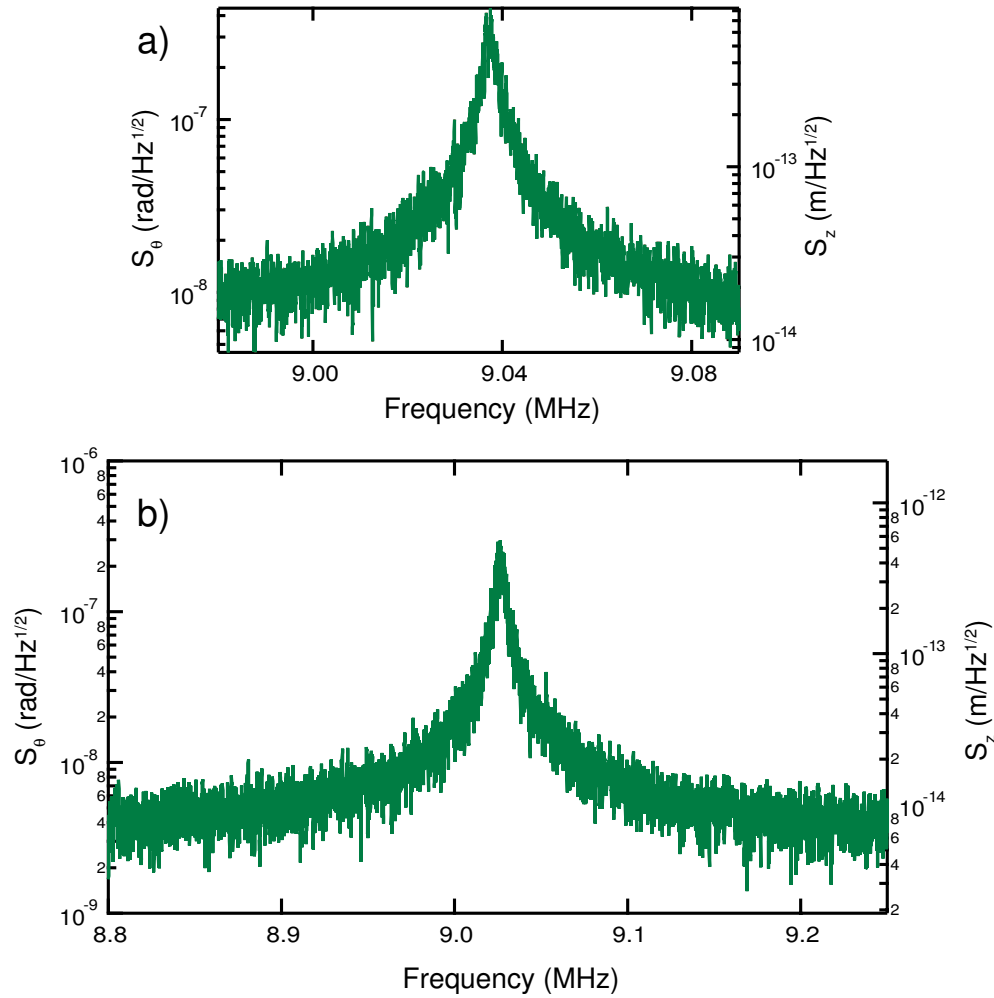


Figure 4.11: a) Calibrated plot of the most sensitive torsional mode (9.04 MHz) from the 10 μm diameter microdisk resonator coupled to the torsion paddle with 100 nm gap. The calibrated noise-floor obtained from the fit parameter (S_v^{nf}) translates to linear displacement sensitivity (S_z^{nf}) of 7 fm/ $\sqrt{\text{Hz}}$ and corresponding angular sensitivity (S_θ^{nf}) of 4 nrad/ $\sqrt{\text{Hz}}$ (36). b) Taken at a later date, plotting the same device but scanning at a wider frequency range confirms that the noise-floor does reach the calibrated values.

to its device number in the design, in further discussions of the torque sensitivities, coupling factors, and air measurements.

4.3 Discussion

From the angular and linear displacement sensitivities, further topics in torque sensitivity, other mechanical modes, and improved torsional designs will be discussed and summarized.

4.3.1 Torque sensitivity

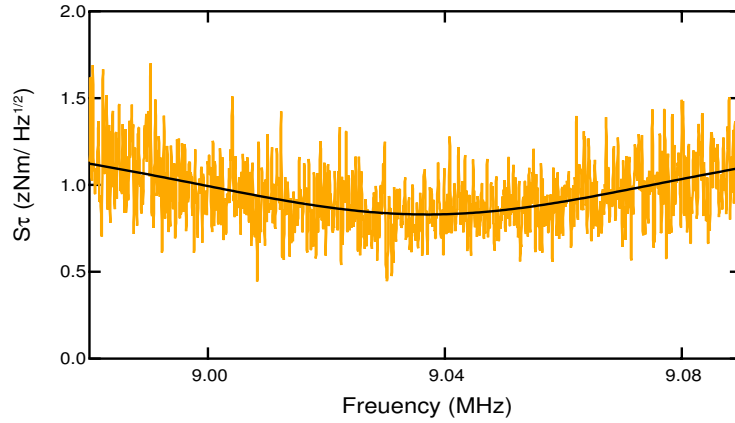


Figure 4.12: Torque sensitivity plot where S_τ was minimum near the torsional resonance.

From the definition of torque, $\tau = \kappa\theta$, the angular noise-floor multiplied by the effective torsion spring constant gives a torque sensitivity of $4 \times 10^{-20} \text{ Nm}/\sqrt{\text{Hz}}$. However this torque sensitivity occurs at the angular noise-floor (outside the resonance), but force sensitivities are enhanced near mechanical resonance, as demonstrated in Doolin *et al.* (31). The torque sensitivities should also be more sensitive near the torsional mode resonance shown in Fig. 4.12. The angular susceptibility, in Eqn. 4.10, was substituted in the relation, $S_{\tau\tau}(\Omega) = S_{\theta\theta}(\Omega)/|\chi_\theta(\Omega)|^2$, to expand the torque sensitivity as

$$S_{\tau\tau}(f) = S_{\theta\theta}(f) \frac{\kappa_{\text{eff}}^2}{f^4} \left((f^2 - f_0^2)^2 + \left(\frac{ff_0}{Q_{\text{mech}}} \right)^2 \right), \quad (4.34)$$

where $S_{\tau\tau}(f)$ is the torque PSD. Fig. 4.12 is a plot of $\sqrt{S_{\tau\tau}}$ as a function of mechanical frequency and the minimum dip in the sensitivity observed at the resonance is $0.8 \text{ zNm}/\sqrt{\text{Hz}}$. This enhancement of torque sensitivity near the mechanical resonance is also reported in

Losby *et al.* where the sensitivity increased by a factor of $\sim \sqrt{Q_{\text{mech}}}$ near its mechanical frequency (62).

I can use the other definition of the torque: $S_{\tau\tau} = (w/2)^2 S_{\text{FF}}$ to find the same result as above (Fig. 4.12). Using this definition, along with $S_{\text{FF}} = S_{\text{FF}}^{\text{th}}$ at the mechanical resonance (31), the resonantly enhanced sensitivity can be expressed as

$$S_{\tau} = \frac{w}{2} \sqrt{4K_{\text{B}}T m_{\text{eff}} \frac{\Omega}{Q_{\text{mech}}}} \quad (4.35)$$

resulting in the same result of 0.8 zNm/ $\sqrt{\text{Hz}}$. As long as the device is thermally resolved, better sensitivity results from smaller torsion width (w), m_{eff} , and larger Q_{mech} . In addition, cooling the device in a dilution refrigerator will result in a better torque sensitivity, where ~ 9 yNm/ $\sqrt{\text{Hz}}$ can be estimated at 30 mK. At this temperature, the equipartition theorem still holds ($k_{\text{B}}T \gg \hbar\Omega$) due to the low frequency device (9.03 MHz) ($10^{-25}\text{J} \gg 10^{-27}\text{J}$), hence the calibration method should still work in these temperature ranges.

4.3.2 Out-of-plane mode

To experimentally verify that mode near 9.3 MHz in Fig. 4.1 is indeed out-of-plane, I used a piezoelectric buzzer underneath the chip to see if it actuates efficiently. At first, I was puzzled that the actuation was not as expected. Rather than actuating in amplitude, the shape of the resonance changed such that broad sidebands appeared. Since the fibre was touching the chip and the buzzer actuates the whole chip, the buzzer might have actuated the fibre and the disk together. I have moved to another setup, pictured in Fig. 4.13 the interferometric apparatus, to see out-of-plane the actuation. With this apparatus, the thermal peaks were not resolved near 9 MHz and 9.3 MHz, but using the buzzer, I was able to see the driven peaks (50 mV), shown in Fig. 4.13. The driven torsional peak was oddly actuated in both amplitude and phase; however, the second mode did look like a typical driven resonance. From this data I am able to conclude that 9.3 MHz is the out-of-plane mode. The effective mass of the out-of-plane mode for C10 was 1.3 pg, resulting in a calibrated displacement noise-floor of 38 fm/ $\sqrt{\text{Hz}}$ and a Q_{mech} of 7180.

4.3.3 Third mode

For completeness, I include the third peak observed in C10 but I was not able to discern any trend from all nine devices. The peak of this third mode is shown in Fig. 4.14 without a calibration as this cannot be done without mode confirmation. A shear piezo could be used

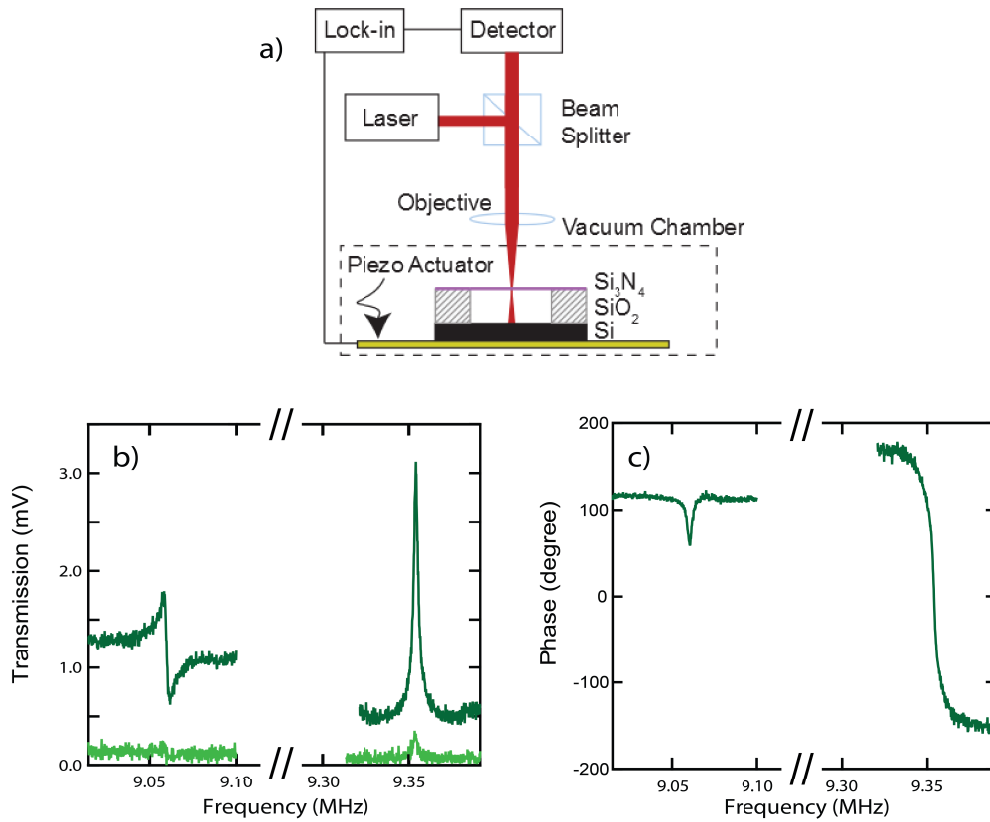


Figure 4.13: The experimental apparatus in a) (56) was used to test the out-of-plane actuation. These mechanical peaks were not thermally resolved, where small peaks only start to appear with piezo-buzzer driving at 10 mV (light green). The dark green in b) is driven at 100 mV and the corresponding phase is observed in c) showing the efficient driven mode at 9.3 MHz in contrast to the 9 MHz peak.

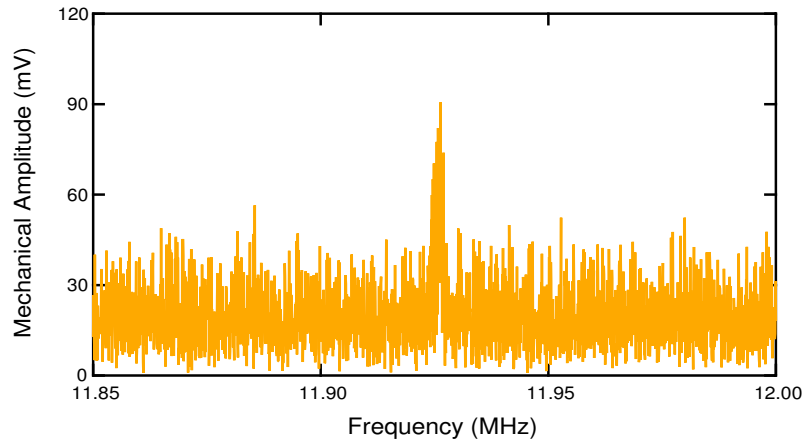


Figure 4.14: The third peak (suspected in-plane mode) appearing near 12 MHz on a linear scale for the 10 μm diameter disk with 100 nm gap.

to investigate this further but I did not pursue this route as the peak was small and I was more interested in the torsional mode.

4.3.4 Second order coupling

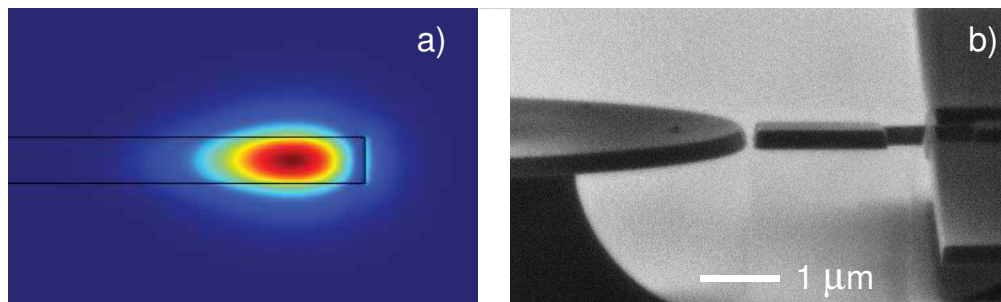


Figure 4.15: a) Optical FEM simulation of the straight side wall and its uniform field for second order coupling. b) An angled image of the optomechanical torsion design with sidewall angles of 10 degrees from vertical.

Based on the planar geometry, seen in Fig. 4.15a, I at first thought that twice the frequency should be seen and not the resonant frequency itself due to symmetry in the optical profile and mechanical motion. However from the angled view of the SEM micrograph, the sidewalls had an angle of $\sim 10^\circ$ from vertical direction breaking this symmetry. The asymmetry caused the experimental peaks to agree with the simulations and not twice the frequency as expected from torsion and out-of-plane modes. Second harmonic peaks were observed in a cantilever device still on the same chip, in which the nonlinear $2f$ signal was investigated thoroughly

(69).

4.3.5 Experimental calculation for G

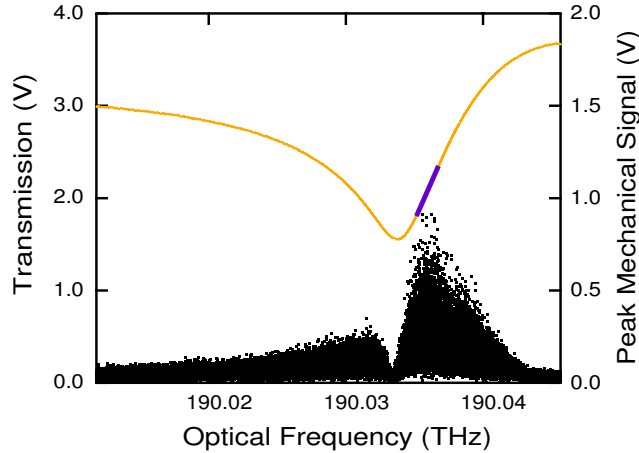


Figure 4.16: The plot is similar to Fig. 4.9 where orange is the optical transmission showing the cavity resonance but plotted against optical frequencies to determine the slope ($\Delta V/\Delta\omega$) at the location of the highest mechanical amplitude of a torsional mode (black). This slope is found by a linear fit (purple line) and is an important quantity to determine the experimental G based on the optomechanical transduction mechanism tuned at the side of an optical resonance.

The side-of-fringe optomechanical transduction, shown in Fig. 4.9, demonstrates that the slope of the resonance plays an important role to the optomechanical coupling coefficient, G . Following the discussions in Refs. (31) and (70), G can be determined experimentally using the known conversion factor, α , and the slope. The chain rule is applied to obtain the derivative of voltage with respect to displacement,

$$\frac{\partial V}{\partial z} = \frac{\partial V}{\partial \omega} \frac{\partial \omega}{\partial z} \quad (4.36)$$

where the latter part ($\partial\omega/\partial z$) is the optomechanical coupling factor for linear displacements. The equation can be rearranged to

$$G = \frac{\partial V}{\partial z} \left(\frac{\partial V}{\partial \omega} \right)^{-1} \quad (4.37)$$

where $\partial V/\partial z$ is the conversion factor, $\sqrt{\alpha}$, and the second term is the inversed slope of the DC transmission with respect to laser frequency at the optimized optical frequency (Fig. 4.16). The C10 device, for example, has α of $1.242 \times 10^{16} \text{ V}^2/\text{m}^2$ and slope of 3.375×10^{-10}

V/Hz. Accounting the AC and DC gains in the PD (40 V/mA and 10 V/mA), G was found to be 82 MHz/nm for the device C10.

4.3.6 Air data

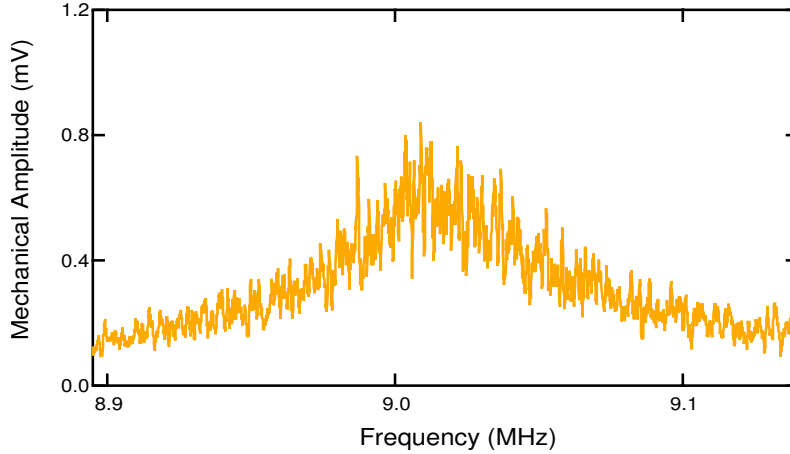


Figure 4.17: Thermally resolved raw data for the optimized torsional device in air with Q_{mech} of 150.

To conclude the discussions of these devices, I also took thermomechanical data in air. This thermomechanical data was observed in the C10 device, but was more difficult to see in other devices. The Q_{mech} suffers significant dissipation from air damping the mechanical system as observed in Refs. (31), (71). For my device (C10), the Q_{mech} was 150 in air.

4.4 Smaller moment of inertia devices

As mentioned in Section 2.1.2, second-year optomechanical designs are parameterized based the successful devices in the first-year, which included trimmed torsion paddles (from ~ 25 pg to 0.7 pg in geometrical mass - designed by C. Doolin). With these devices, I saw slight improvements in displacement sensitivities over our published data.

4.4.1 SEM

The geometry in the second batch was mainly focused on 10 μm diameter disks with evanescently coupled gaps of 130 nm where the mechanical structures were varied via coupling length illustrated in Fig. 4.18). The effective mass of the torsional mode was ~ 0.3 pg,

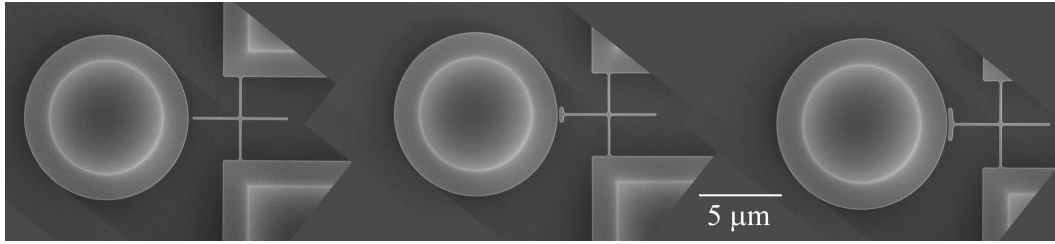


Figure 4.18: SEM images of three small mass torsion paddles with increasing coupling length towards the right ($0.13 \mu\text{m}$, $1 \mu\text{m}$, and $2 \mu\text{m}$, respectively).

slightly smaller than the previous designs (0.7 pg). The right-most device, T677, in Fig. 4.18 gave the best noise-floor and maximum signal, but higher asymmetry is apparent in the torsion paddle with larger changes in the moment of inertia.

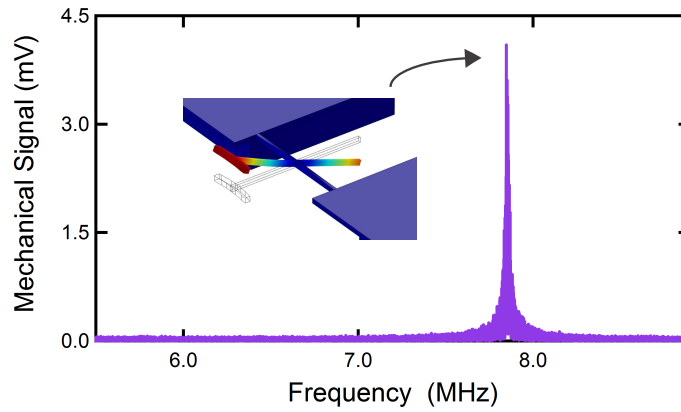


Figure 4.19: From the skinny torsion paddle structure (T677), one major torsional peak was observed near 8 MHz. Other mechanical resonances have very small amplitudes due to the asymmetry in the torsion paddle where the weight is primarily on one end.

4.4.2 Simulations and optimizations

For all three devices in Fig. 4.18, FEM simulations were performed to identify their mechanical modes. The change in the geometrical shapes, meant to increase the optomechanical coupling, resulted in non-trivial mechanical modes from the asymmetric design. One interesting feature of these trimmed torsion paddles is that the simulated frequencies are far apart, hence there are no hybrid modes with the flexural mode like the C10 device. The torsional mode, which is the mode of interest, agreed well with the simulated frequency.

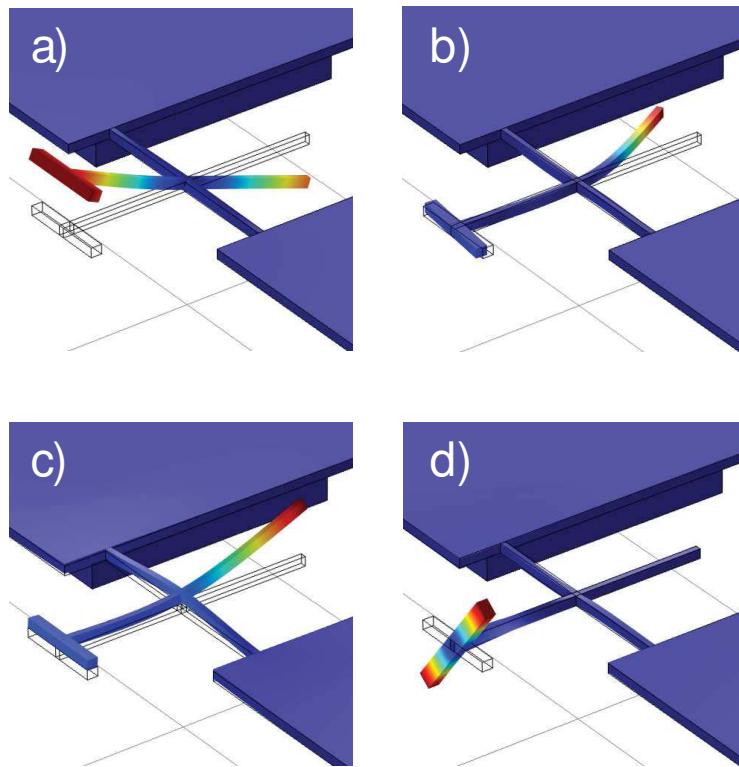


Figure 4.20: FEM simulations of the T677 device showing some of the structural modes in a) 6.61 MHz, b) 17.97 MHz, c) 20.61 MHz, and d) 27.64 MHz. Due to the added mass on the paddle close to the microdisk, it has smaller mechanical amplitudes for modes b), c), and d), compared to the torsional mode a). From the experimental data, shown in Fig. 4.19, a single large torsion peak near 8 MHz was observed.

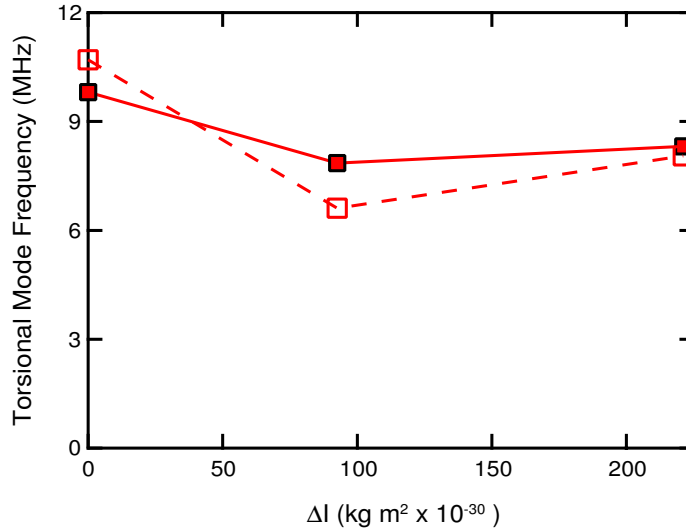


Figure 4.21: The change in the moment of inertia plotted for the three different devices in Fig. 4.18 where the drastic changes in the moment of inertia was observed compared to Fig. 4.3. The simulation (hollow squares) agrees well qualitatively with the experimental data (solid red squares). Lines are guides to the eye.

To confirm this mode I have used the same approach as Section 4.1.4.2 to calculate moment of inertia for all three devices using exact geometries. As shown in Fig. 4.21, large changes in the moment of inertia were demonstrated in comparison to the Fig. 4.3. The experimental results qualitatively agrees with the simulations, or has a similar trend, illustrated in Fig. 4.21.

Applying the same procedure for optimizing the mechanical data using a lock-in amplifier, I have found the best spot near the 1587 nm to take the mechanical data shown in Fig. 4.22.

4.4.3 Best device from the trimmed paddles

Fig. 4.23 shows the optimized scan of the T677 device with calibrated noise-floor of $6 \text{ fm}/\sqrt{\text{Hz}}$ and $2 \text{ nrad}/\sqrt{\text{Hz}}$, slightly better than C10 device. Although it is not a significant increase in its sensitivities, the purpose was to reduce the size of this torsion paddle. On the other hand the resulted torque sensitivity was twice the C10 device ($1.6 \text{ zNm}/\sqrt{\text{Hz}}$ near the torsional resonance), mainly due to the lower Q_{mech} . From Eqn. 4.35, the torque sensitivity is dependant on $\sim \sqrt{Q_{\text{mech}}}$ and the T677 has lower mechanical quality factor (625) compared to C10 device (3750). The next generation of torsional device, therefore, should be designed to have large Q_{mech} as well as the displacement sensitivities by parameterizing the torsion rods.

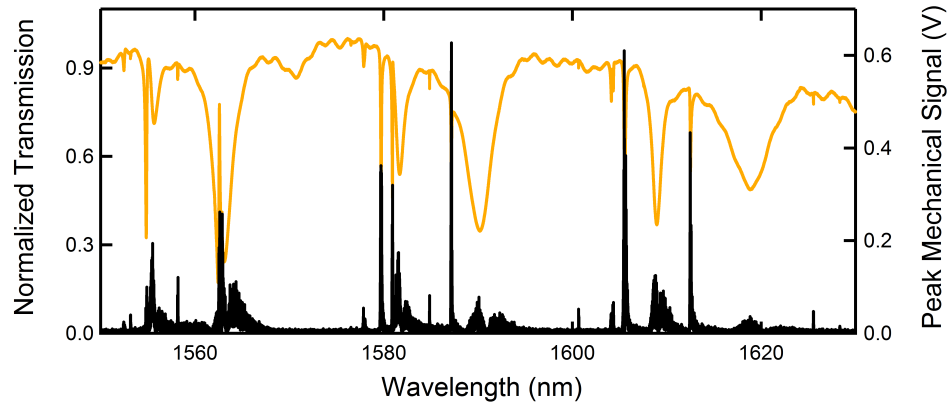


Figure 4.22: Optimization process to maximize the peak mechanical amplitude at 7.85 MHz (the torsional mode), where the optical resonance near 1587 nm was used.

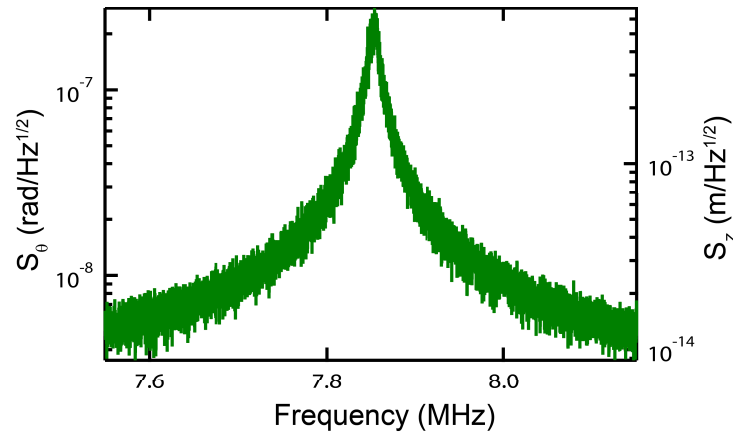


Figure 4.23: The frequency spectrum of the device T677 of the torsional mode in log scale. This device is slightly better in sensitivity compared to the C10 device but has lower Q_{mech} of 625.

CHAPTER 5

Conclusion and Outlook

If I have seen further it is by standing on the shoulder of Giants.

- *Sir Isaac Newton*

V. B. Braginsky is one of the distinguished figures in cavity optomechanics who predicted that the radiation pressure from a high- Q_{opt} cavity can affect a coupled mechanical oscillator via cooling and amplification, which was demonstrated in a torsion-balanced coupled to a Fabry-Pérot cavity (72). The radiation pressure effect, or the back-action of measurements, ultimately sets the lower-bound as the SQL where I gave an exceptional example of LIGO in Chapter 1 - whose sensitivity was limited by the Johnson noise in low power, and radiation pressure in high power. To utilize the radiation pressure effect more fully - optomechanical devices were constructed in a sideband resolved regime, which the optical linewidth ($\Delta\omega$) is comparable to the mechanical frequency (Ω_n), to demonstrate mechanical cooling (26) for mechanical modes down to its quantum ground state (73), (74) using a pump-probe method.

The possibilities to observe quantum effects in a macroscopic NEMS system with radiation pressure assisted cooling certainly caught my attention; however, my optomechanical devices are not sideband resolved since my torsion frequency is much lower (few MHz) compared to the optical linewidth of a microdisk (GHz). Recently rather than focusing on a single mechanical mode cooling, there are also ways to couple two distinct mechanical modes in a system to parametrically amplify and damp the modes, opening up doors for mechanical entanglement (75), (76). Engineering my single torsion paddle to multiple paddles, using optomechanics, I should be able to observe and control more effectively for coupled torsion modes. Also rather than relying on the back-action cooling, we are developing a new low-temperature optomechanical apparatus - where I could passively cool the mechanical device to study quantum systems in experiments.

Although I will follow the similar trend in the cavity-optomechanics community for pump-probe methods, there are also advantages to my published work. For sensing applications, the resolved-sideband regime is discouraged since we want to simply enhance the detection while not affecting the mechanical device from measurements. There are many applications in sensing nanoscale magnetic systems, studying macroscopic quantum phenomena, and probing material properties. So far I have given an overview of the current topics in cavity optomechanical systems towards quantum measurements using sideband cooling; however, there are many other applications to be made in non-sideband resolved devices.

5.1 Summary

The motivation for this project was to demonstrate the usefulness of the optomechanical platform for torsion oscillators as they are reduced in scale. I have successfully characterized a set of optomechanical torsion designs to probe thermomechanical motion very sensitively, much improved over previously reported devices (14), (62). Some important parameters for enhancing the sensitivity, or noise-floor, in a optomechanical system was the Q_{opt} of the optical cavity, the gap between the optical and mechanical resonators, and the microdisk diameters - where I implemented a dimpled tapered fibre for efficient optical coupling. The mechanical data was optimized using a lock-in amplifier, which allowed identification of the best optical resonance for data acquisition. Using the most optimized device I have obtained displacement noise-floor sensitivities of $7 \text{ fm}/\sqrt{\text{Hz}}$ and $4 \text{ nrad}/\sqrt{\text{Hz}}$, which correspond to torque sensitivities of $0.8 \text{ zNm}/\sqrt{\text{Hz}}$ near the torsional resonance frequency of 9.03 MHz . Further improvements were made, where the mass of these torsional devices was reduced (from 25 pg to 7 pg), while the sensitivities were increased slightly to $6 \text{ fm}/\sqrt{\text{Hz}}$ and $2 \text{ nrad}/\sqrt{\text{Hz}}$. My project successfully showed that this optomechanical platform increases the sensitivity of nanoscale torsional oscillators.

5.2 Outlook

One of the immediate future prospects for torsional optomechanics is to test in real sensing applications. An example of studying molecule dynamics will be possible if the molecules are bonded to a functionalized paddle by sensing the change in the moment of inertia and the shifted frequencies. Therefore a controlled deposition technique using a patterned resist, required for the functionalizing the non-reactive silicon paddle, is listed in Appendix C. Moving to magnetic materials deposited on the paddle will open up doors for numerous magnetism-related studies in nanoscale regime. Simultaneously I am also currently working

on a recipe to fabricate devices myself for the next generation of torsional devices without having to rely on commercially fabricated products. I have been optimizing an EBL recipe using a hydrogen silsesquioxane (HSQ) resist, while optimizing plasma etch for silicon. Once these nanofabricated torsional devices are improved and functionalized, they will be incorporated into a dilution cryostat to improve torque sensitivity and explore macroscopic quantum effects such as superconductivity, superfluidity, and the de Haas-van Alphen effect.

5.2.1 Exploring other materials for optomechanical systems

From the available commercial fabrication, I was provided with a SOI platform having both excellent mechanical and optical properties. However there are other robust materials to be considered in optomechanics.

Material	Young's Modulus (GPa)	Index of Refraction
Si	190	3.48
SiC	700	2.59
SiO ₂	73	1.46
Si ₃ N ₄	380	1.98
AlN	308	2.12
Diamond	2035	2.39

Table 5.1: List of Young's modulus for various robust materials (38) and corresponding index of refraction near 1550 nm (77).

Table 5.1 shows various materials listing two basic properties of Young's modulus and index of refraction as a measure of their mechanical and optical properties (38), (77). Both properties should be high for ideal optomechanical systems resulting in high Q_{opt} and Q_{mech} ; however, there seems to be a trade-off between the choice of optical material or mechanical material. GaP is another optical material recently implemented in an optomechanical system (78), which is optically comparable to silicon but the Young's modulus is lower than silicon (~ 103 GPa). SiC, a diamond-like crystal, has been nanofabricated recently as a circular torsion paddle using a similar smart-cut technology to produce SOI wafers (79) - nevertheless patterning and etching this material is extremely difficult for optomechanical structures. The best way to implement both of the best worlds is to use a hybrid system using different materials for optical and mechanical resonators. Such hybrid system was used in a force sensor developed by Gavartin *et al* using Si₃N₄ nanostrings and SiO₂ wedge-disks. Although the index of refraction of SiO₂ is low, fabricating very smooth sidewall is possible (33). Such a hybrid system is desirable, but requires a lengthier and more complex fabrication procedure. Another interesting material is AlN, where this material is also piezoresistive making it possible to have an opto-electro-mechanical platform (80).

Among the different possibilities, my realistic choice for the next optomechanical material would be Si_3N_4 concentrating more on the elasticity of the material. The high stress Si_3N_4 has exceptional mechanical properties (56) and is also a good photonic material that is relatively easy to fabricate.

5.2.2 Upgrades on the apparatus

The schematic used in this project (Chapter 2) for optomechanical transduction is beautifully simple and simply beautiful and yet it is highly sensitive in a small scale device. However there is room for improvement in the apparatus. Since there are slow drifts in the laser, a Pound-Drever-Hall (PDH) technique can be employed for laser frequency stabilization. This technique uses a phase-modulated laser locked in an external stable Fabry-Pérot in a feed-back loop to adjust the drifted laser frequency (81).

We can also add another laser to the system in order to parametrically drive (pump) the mode while doing the measurement (probe). A balanced homodyne detection technique is also being considered to do a phase-sensitive detection instead of the amplitude-sensitive detection (47).

5.2.3 Low temperature apparatus

From the specialty of our lab, we are planning to implement the optomechanical apparatus in a dilution refrigerator to observe quantum phenomena using optomechanical sensors. There are a lot of technical details, omitted in this section, to reach mK temperature ranges mostly dealing with thermalizing the wires, sample, and the fibre. The setup resembles the room temperature OVC as shown in Fig. 5.1 with essential parts such as the objective, positioning stages, and the fibre holder. There is still a lot more work to be done, which we are working hard on as a team.

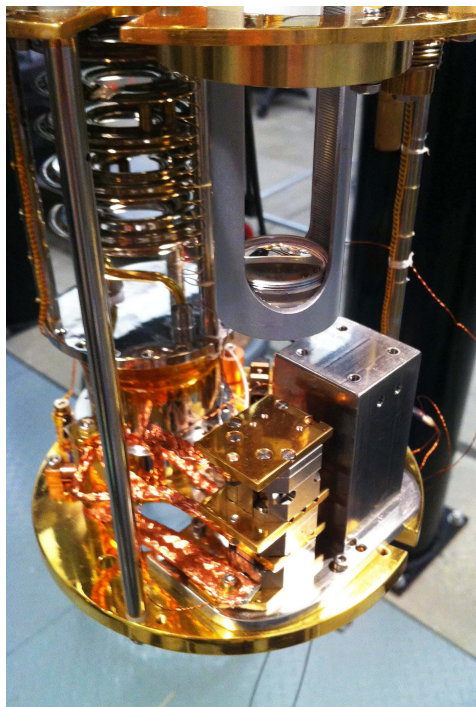


Figure 5.1: A photograph of our current progress with the low-temperature optomechanical apparatus. The components are similar as the room temperature OVC where a microscope, nan positioning stages, and a fibre holder are present.

APPENDIX A

Smaller dimpling procedure

I always do that, get into something and see how far I can go.

- Richard Feynman

At times, the optical cavities were hard to couple into with our standard dimpled tapered fibres, in particular when there are other structures too close to the device. De-tensioning the fibre-dimple to narrow the lowest spot did not help as it adds mechanical instability to align properly, similar to the case of the u-shaped fibre. A simple idea to make the dimple even smaller was achieved using the same procedure as described in Section 3.3 but using a tapered fibre as a mould instead of the bare stripped fibre. The tapered fibre mould should not be pulled to a single mode, stopping half way through the rapid oscillations of Fig. 3.12, to maintain its rigidity as a mould. The tapered fibre mould tends to be easily fused with the dimpled tapered fibre during the dimple-annealing process than the bare stripped fibre. Therefore I had to clean the mould surface well and applied more graphite than usual and nearly all transmission was maintained (99.5 %) when finished (see Fig. A.1b). A summary of the smaller dimple fabrication is shown in Fig. A.1 including the tapered fibre profile, dimpling procedure, and the photograph of the final result.

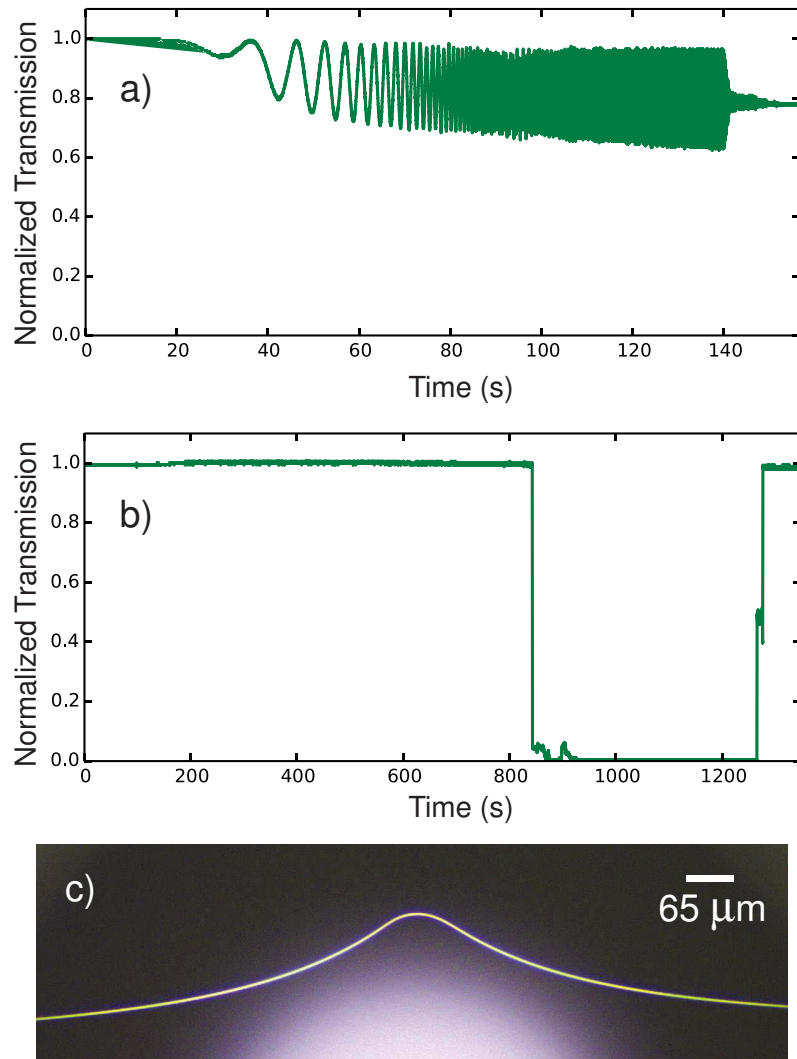


Figure A.1: The same procedure from Section 3.3 was used to produce smaller dimpled tapered fibres where a half-tapered fibre is used as a mould with diameter $\sim 65 \mu\text{m}$. a) The typical tapering profile with 78 % efficiency down to a single mode fibre near $1 \mu\text{m}$ in diameter. b) After the dimple procedure, the transmission was recovered (99.5 %) where the optical image of a fully fabricated tapered fibre is shown in c).

APPENDIX B

New optomechanical torsion design

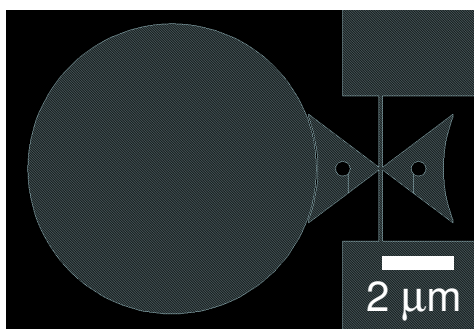


Figure B.1: An example of a possible design for the next generation of torsional device. The gaps are drastically reduced to ~ 35 nm and the coupling length are increased by a triangular paddle to increase G . The holes are inserted to reduce the mass of the torsion device and the device is highly symmetric. This design is currently used to optimize the recipes for EBL patterning and plasma etching (ICP-RIE).

Although EBL patterning is not a cost-efficient process, it provides better resolution than the commercial options using the state-of-the-art photolithography patterning (< 100 nm). Based on a two-year project general parameters to consider in the design process are minimizing the gap between the two resonators, increasing the coupling strength, maximizing the intrinsic Q_{opt} , and Q_{mech} , reducing the paddle width w , and decreasing the effective masses. A preliminary design, aimed at achieving better angular or torque sensitivity, is shown in Fig. B.1. I am still in the process developing optimized torsion designs for device fabrication.

APPENDIX C

Deposition

C.1 Magnetic nanoparticles

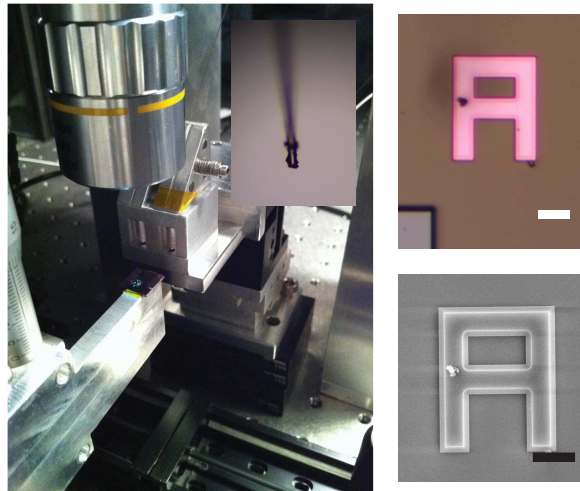


Figure C.1: Depositing small magnetic nano-particles (maghemite) on the chip using the pick-and-place method in the fibre-puller setup. The spot on the letter *A* (right) shows the deposited particle, placed from the tip of the tapered fibre. Due to a floppy tapered fibre, I was not able to aim and deposit precisely. The scale-bar is $10\ \mu\text{m}$.

In order to drive the torsional mode efficiently with an AC magnetic field I have attempted to place small magnetic nano particles on the paddles. The nanoparticle used was a maghemite (superparamagnetic) core with silica in a dH_2O solution. I tried to use the pick-and-place method using the tip of the tapered fibre to deposit this particle on a chip. After some tests, this method could not accurately deposit particles at a desired location for number of

reasons but the main issue was that the apparatus was built lego-like, where I have gathered and assembled various parts of the experiment shown in Fig. C.1. The micrometer did not have the precision I need for accurate deposition using a broken tapered fibre. The best I could do was shown in Fig. C.1 where I aimed for the centre of the middle line in the letter *A* but was clearly off by $\sim 20 \mu\text{m}$. Implementing a small dimple could work, being more rigid, but it destroys both the dimple and the device for each trials. Rather than pick-and-place method, depositing small magnetic films seems to be a much elegant method. The problem with this method, however, is that depositions usually occur prior to releasing the device with wet-etchant - where BOE does etch most magnetic materials. There is a new technique recently developed by Diao *et al.* where the patterned magnetic films can be deposited after the structure is released (82). This technique involves placing released structures in a solvent (IPA), and slowly introducing organic resists in the solution, which fills all the gaps and surface with the resist. After baking the resist, the chip can be patterned with EBL. This method seems more promising and is a current work in progress.

C.2 Pt dots

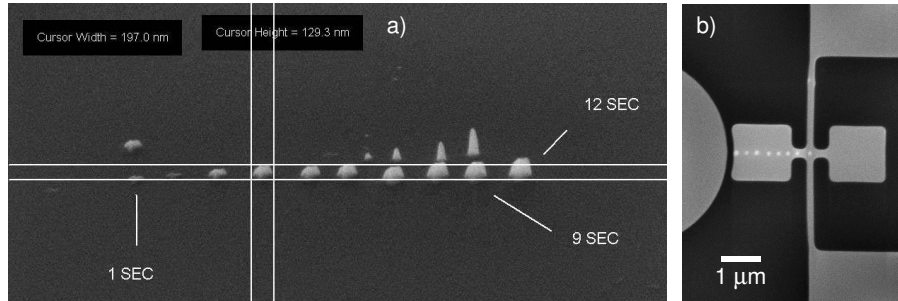


Figure C.2: a) Exposure test of Pt dot depositions with varying exposures from 1 to 9 seconds. b) Throughout the devices we have exposed ~ 4 seconds on each dots giving dots of ~ 100 nm in size.

I also attempted to deposit of Pt dots on the torsion paddle. The purpose was to see the effects of tiny metal dots deposited on dielectric paddles on the optomechanical coupling. The depositions were operated using the focused ion beam (FIB) located at NINT, where Pt gas was introduced into the chamber and the electron gun is spotted in areas of interest for deposition. During this process Pt dots were successfully transferred to the paddles as shown in Fig. C.2 but from experimental data, I have seen significant degradation in all optomechanical parameters including both Q_{opt} , Q_{mech} and the noise floor. This could be the effect of metals on an optomechanical system, however I note that being able to observe anything through the FIB deposits small amounts of Pt - possibly on the disk as

well (Fig. C.2b). It is possible that the degraded optical disk lowered all the optomechanical parameters. Optical structures need to be masked, or unaffected, by the deposition in the torsional resonator - introducing the next appendix to pattern metal on the paddles.

C.3 Gold Deposition

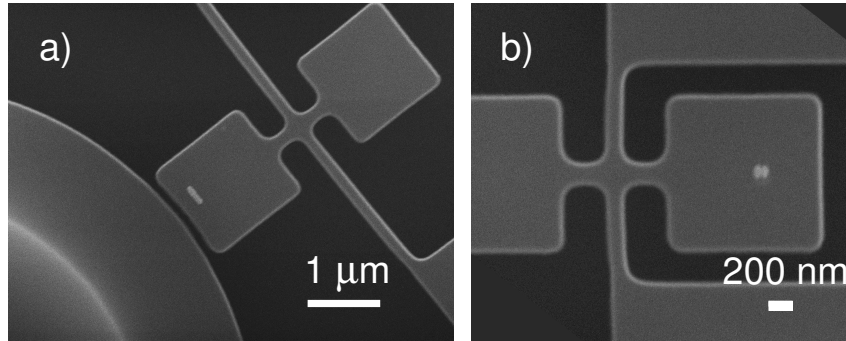


Figure C.3: Successful patterned gold film (~ 15 nm thickness) deposited on the paddles as shown in a) and b) with smallest feature size of ~ 80 nm in b).

The best way to mask an optical disk while simultaneously pattern windows on the paddle for deposition is done with EBL (Raith150-Two). Photolithography is not suited for this post-patterning mainly due to the feature resolution and the alignment resolution. I have optimized the EBL recipe to align the already designed structures using alignment marks and create openings for thermal deposition of metals. Successful examples of gold deposited torsion paddles are shown in Fig. C.3 with potential applications in molecular sensing. The gold-functionalized surface allows thiol bonds to molecules containing sulphur, facilitating the study of the dynamics of molecules.

C.3.1 Post-alignment recipe for EBL

I have used EBL to pattern windows for thermal deposition while all other structures are successfully masked. The EBL process is essentially the same as scanning-electron imaging with an added pattern generator to deflect the electron beam in a small area (write-field of $100 \mu\text{m} \times 100 \mu\text{m}$) to pattern the organic resist. This procedure is typically very slow, depending on the doses, but produces highly accurate patterns. It takes some effort to optimize exposure doses on a specific resist thickness, aperture, and voltage. I have mainly used EBL to post-pattern the already fabricated IMEC chips, where aligning the structures on a nm-scale raised the difficulty significantly. Each trial took a long time because of

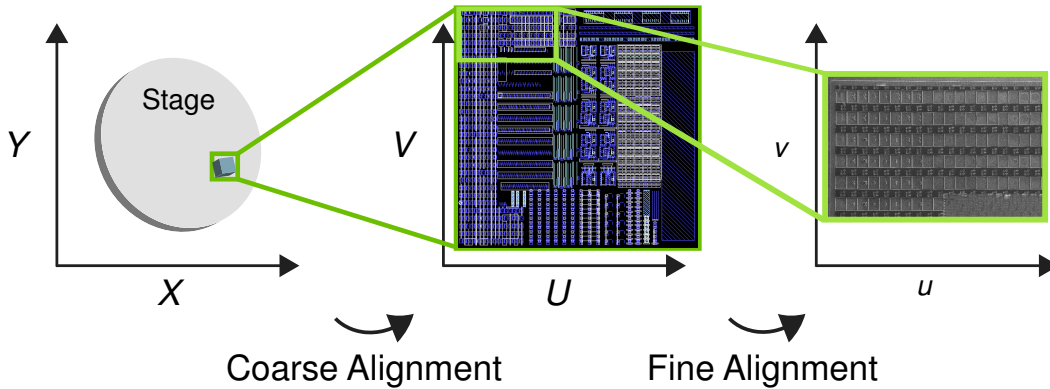


Figure C.4: Post-alignment includes aligning all three different coordinate systems in the equipment. The stage movement (X, Y) should first be aligned with the design coordinates (U, V) (coarse alignment) and the electron beam should be adjusted (fine alignment) to account for the actual coordinates in a real chip (u, v).

lengthy steps required: piranha cleaning, resist spinning, EBL patterning, and SEM imaging. While waiting for the second batch of IMEC chips, I have optimized the post-patterning process to align the fabricated structures with the design quite well allowing me to pattern any shapes on the torsion paddle shown in Fig. C.3. The complete recipe for the EBL alignment process will be listed in this section, where I skipped all the of the basic training steps for proficient EBL users. The difficulty in alignment comes from the three different coordinate systems, the stage, design, and the device coordinates, that must be synced prior to electron beam exposures. Fig. C.4 shows the simplified procedure as the coarse, dealing with stage alignment to the designed GDS file, and fine alignment, controlling the beam deflection within the write-field to account for the discrepancies from the design and the actual fabrication.

I specifically chose polymethyl methacrylate organic resist (PMMA), which is available in different molecular weights. For example using 495K and 950K PMMA, the different molecular weight causes different exposures with the same dose, allowing the lighter bottom layer to expose more than the top layer creating a window such that the gold on the chip does not touch the resist during deposition. In this configuration shown in Fig. C.5, a very thin deposition layer can be achieved where a single PMMA layer resist often removes the deposited metal together when the layer is thin (~ 20 nm).

I will present the recipe in a step-by-step form, trying to avoid confusion. The following recipes are for trained EBL users for those that are interested. One important rule of thumb is to never look at device during the EBL process, where the user should only look at the

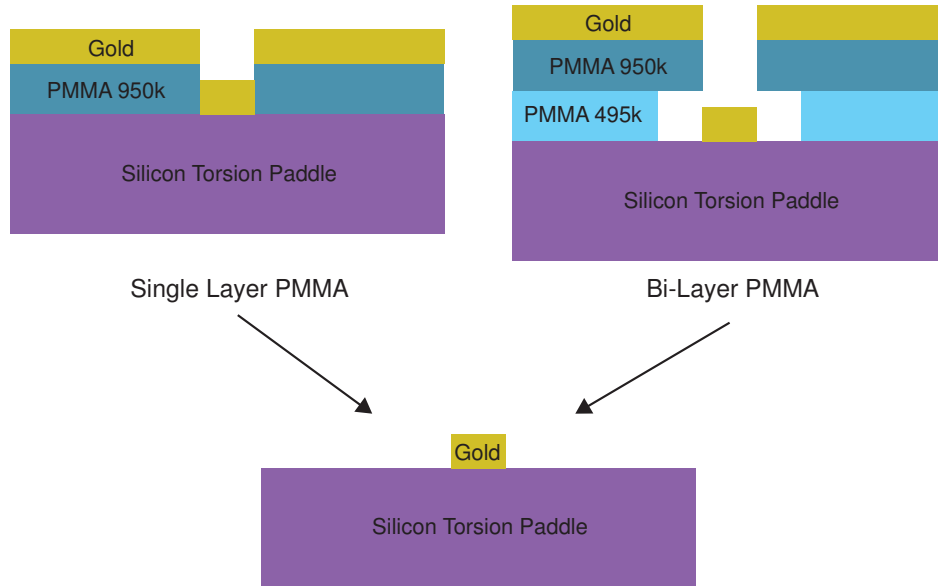


Figure C.5: Illustration of the bilayer structure of PMMA. The lighter PMMA 495k is underneath the heavier PMMA exposing more with the same dose, where it creates a nice contact-less window compared to the single layer case. Bilayer method is required for very thin layer or a small feature size.

alignment marks. Hence, the coordinates of your devices with a custom-chosen origin should be pre-determined before proceeding with the post-alignment process.

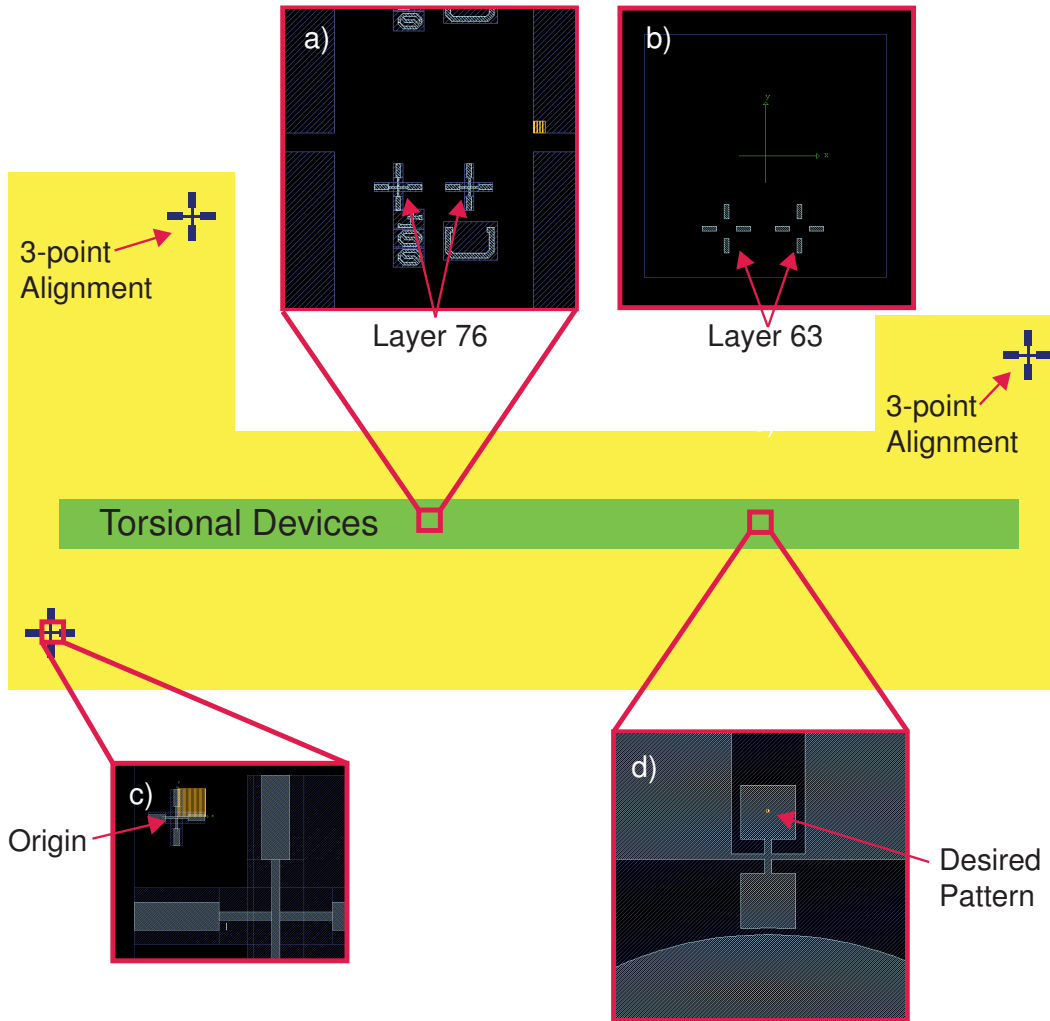


Figure C.6: A layout of the IMEC chip where the green area is the location of optomechanical torsional devices. Based on the alignment marks as shown in a), a separate layer (63) having eight rectangles inside the $100\ \mu\text{m} \times 100\ \mu\text{m}$ write-field box was prepared to do fine-alignment as shown in b). Coarse alignments were done by a 3-point alignment, where the origin in c) and the other two alignment marks (marked by arrows in the layout) were used. I have made patterns on torsional paddles as shown in gold colour (layer 92) with an example demonstrated in d). Note in a), a gold box in the corner was also patterned to confirm how well the alignment was done after the exposure of bi-layer PMMA.

• Preparation

1. A new gds file must be prepared with the desired exposed pattern overlaid on top of the existing device features in a different layer. An example illustrated in

Fig. 2.9 defines the layer 92 (gold colour) as exposed area. The resist being used is a positive resist PMMA, in which the exposed area will provide a window for metal deposition. Layer 76 is the existing pattern fabricated by IMEC and an arbitrarily chosen layer 92 (gold) is the desired overlaid design. The Raith150-Two software, used in EBL, always defines the left bottom corner of the structure to be the centre the write-field. I made a small box (layer 92), where bottom-left corner is forced to be the origin $(U, V) = (0, 0)$ as shown in Fig. C.6c. I have also made small boxes at a corner near a device to inspect the alignment as seen in Fig. C.6a.

2. The Layer 63 is specifically reserved in the Raith150-Two software for the automatic write-field alignment. A separate design should be patterned with the same alignment marks in this layer as shown in Fig. C.6b. Note that these structures should be simple geometries such as squares or rectangles. Complex geometries made by boolean operation in layer 63 did not scan properly with the software. The sample alignment features I used are shown in Fig. C.6b (layer 63). Designs in layer 63 should not exceed the write-field area, which is typically $100 \mu\text{m} \times 100 \mu\text{m}$.
3. Piranha-clean the sample before spinning the resist on the sample.
4. Using the Brewer Spinner and Hotplate equipment, coat the IMEC chip with first the PMMA 495K A2 resist followed by PMMA 950K A2 resist. I have programmed the spinning recipe in *PK_PMMA_BILAYER* that should resulting in $\sim 120 \text{ nm}$ thickness. The hotplate should be preheated to 180°C .
 - Place the chip on the smallest chuck holding it with vacuum.
 - Run a test spin using the programmed recipe *PK_PMMA_BILAYER*. It should spin 500 RPM for 10 seconds with ramp speed of 100 RPM/s and 4000 RPM for 40 seconds with ramp speed of 350 RPM/s.
 - Apply plenty of drops (> 4 drops) with a pipette to cover the whole chip with PMMA 495K A2 resist and wait 10 seconds prior to spinning for consistency.
 - Run the recipe (*PK_PMMA_BILAYER*) and bake the sample at 180°C for 10 minutes.
 - Repeat the spinning for PMMA 950k A2 resist on top of the 495k layer with the same recipe. Note that prior to spinning 950k resist, the sample should be completely cooled down by waiting ~ 1 minute after the baking.
 - The resist usually coats partially on the back-side of the chip in the four corners. Simply remove them using plastic tweezers and acetone applied Q-tips for better thermal contact in the Raith150-Two sample holder.

5. Scratch the corner of the chip (non-important area) using a diamond scribe to obtain a small particle for focusing.
6. When mounting the chip on the sample holder, the chip should have good thermal contact with the sample holder for optimal results. Simply wiggle the chip using a plastic tweezers after clamping.
7. After clicking the *load sample* button the automated processes will place the chip inside the chamber. Turn on the SEM controller and activate the accelerating voltage to 10 kV (EHT) with 10 μm aperture. Raise the Z-axis to 19 mm using the *XYmode* in the software. under the Raith150-Two stage controller.
8. Locate a particle of size ~ 200 nm near the scratched corner and perform the typical SEM operation to obtain a good image by adjusting the focus, stigmatism, and aperture. Skip the write-field alignment, typically done at this step, until the end. In post-alignment EBL, the fine alignment using layer 63 will overwrite any existing write-field alignment hence it is not necessary at this point.
9. Measure the current by driving the stage to the *Faraday Cup* position and click *Measure*. Set the experimentally determined optimized exposure dose to 144 $\mu\text{C}/\text{cm}^2$ (it may vary).

• Coarse Alignment

1. First, locate the origin of the chip using the SEM live image. Only work with the patterned alignment features and never image directly the devices through the SEM as it will expose the resist. In the example (Fig. C.6c), the origin is at the inside corner of the alignment mark shown in Fig. 2.9. Under the *Adjust UVW - origin correction* click *Adjust* and make sure that Global mode is selected.
2. Either use the centre of the cross-hairs in a live SEM scans or scan a new image (*File* \rightarrow *New image* in the Raith150-Two software) and place the flag on the SEM to find the exact coordinates in the stage (X, Y) and press *adjust origin*. The latter method is highly preferred as the live image always drift slightly and the scanned image is actually how the pattern generator is going to write the pattern. Therefore, scanned images should be the basis for any alignment.
3. In the angle-alignment, keep the origin as one of the coordinates and move the sample along X direction until the last alignment mark is found. Be careful not to expose actual devices at this point by controlling the zoom and the stage movement. Flag the position on the alignment mark using the scanned image and click *Adjust*. Note that these two alignment marks, used in angle-alignment, should be perfectly horizontal in the GDS design.

4. Change the mode to *Local* and do a 3-point alignment. Click *Drive* under the angle correction menu to move to the origin and define this point as one of the 3-points. Drive to the other alignment mark locations as shown in Fig. C.6. If the origin- and the angle-alignment was done properly in the global mode, the alignment marks at a far location should be easily found without exposing much of the area nearby. While the stage is driving the beam is blanked, or covered, automatically to avoid exposures along the way. The procedure is the same as the origin and the angle correction using the flag to find the three points in the scanned image. Note that the three-points should not be on the same axis as illustrated in Fig. C.6. After clicking *Adjust*, the design coordinates should now be synced with the stage movement with good accuracy. Navigate through different alignment marks to check the coarse alignment.

- Fine Alignment

1. The fine alignment is done by the write-field alignment, which aligns the beam to the exact features of the devices. The layer 63 described above was used to align the 8 rectangles to the alignment marks. Note again that the complex geometries sometimes does not scan properly, so I used simple rectangles from the software.
2. Move the stage to the smaller alignment mark (Fig. C.6) near the device of interest. The centre location with respect to the alignment marks should be precisely the same with the origin created in layer 63.
3. Create a new position list (*File* → *New positionlist*) and add the layer 63 designs to the list.
4. Scan layer 63 by clicking (*Scan* → *All*) and a scanned image will appear with one rectangle overlaid with the one of the alignment block with some mismatch. Hold Ctrl key and move the box such that they are perfectly aligned and click *Accept*. All the 8 boxes designed in layer 63 will be scanned consecutively and separately and the alignment results will be based on these scans.
5. The devices near this write-field aligned area are ready for exposure but the exposed area should be kept at minimum for best results. It will be at best within the same write-field, but in my case the devices one write-field box away. Exposing structures far away from this alignment (\gg write-field area) will cause large deviation from the desired pattern. Therefore, write-field alignment should be over-written again in the next area of interest. This can be a long process where creating a new position-list is a great idea with repeating sequences of write-field alignment and small area exposure. The exposed area should be chosen carefully because the left bottom corner of the desired area will be considered as the origin in u, v coordinates. Therefore the U, V coordinates should be manually filled to

displace the exposure area to the desired location. For example, if I desired the working area to be $200\ \mu\text{m} \times 200\ \mu\text{m}$ at the location (1 mm, 1 mm), then the U, V coordinates should be (1.05 mm, 1.05 mm) with working area defined by two points (1 mm, 1 mm) to (1.2 mm, 1.2 mm). The $50\ \mu\text{m}$ is added to each U and V to account for the write-field of $100\ \mu\text{m} \times 100\ \mu\text{m}$ (if different write-field sizes are used, the (U, V) should be added to the half-length of these coordinates).

- **Fine Alignment without Layer 63**

1. There is a quicker way to produce decent results without the layer 63 if there are only handful of structures to post-pattern. However, the former method using layer 63 is preferable. This quick method requires a typical write-field alignment in step 8 under "Preparation".
2. After the coarse alignment, navigate to the alignments marks near the interest area for exposure. Make sure the location is equally displaced between multiple alignment marks (Fig. C.6a for example).
3. Blank the beam and drive manually within the write-field using relative coordinates in (U, V) and obtain a scanned image. If the location is not exact, manually input the U -shift and the V -shift based on the scanned image and click send (box under *write-field Alignment*). The input should be inverted with respect to the image. For example, if the image was shifted 100 nm in U -direction to the right, then input $-0.1\ \mu\text{m}$ in the U -shift column. Go back to the exact original location as shown in Fig. C.6.
4. Test various corners starting from the same location to map each points to correct U -shift and V -shift. After satisfactory alignment, expose the desired area nearby and remember to add $50\ \mu\text{m}$ to the design (U, V) coordinates.

The results from these alignment procedures are shown in Fig. C.3 using both methods. They are not perfect because I have used slightly larger exposure area centred around the write-field alignment, but they were very satisfactory to pattern various shapes on the torsion paddles. After properly shutting down the system clicking *unload* button, the PMMA layer was developed for one minute in MIBK:IPA (1:3) and 20 seconds in IPA after a thorough rinse with water. After drying the chip with an air-gun, the sample is now ready for metal deposition.

C.4 Thermal evaporation for thin film deposition

The post-patterned device is now ready for deposition, where I used a custom-built thermal evaporator system at the thin-film lab (UAlberta) as shown in Fig. C.7. The automated

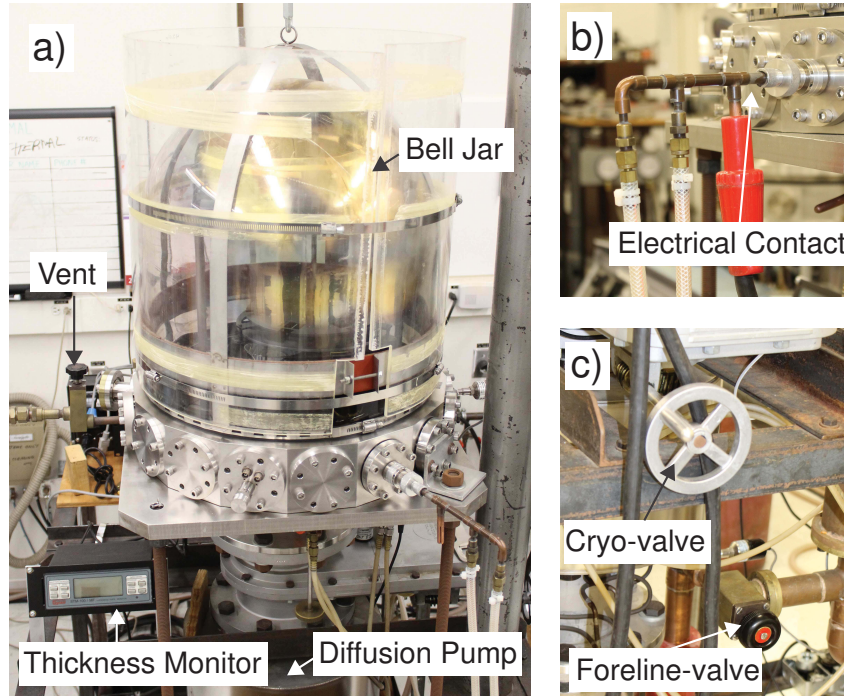


Figure C.7: A high-vacuum evaporator system located at the thin film lab (UALberta). a) A photograph of the bell jar used for thermal deposition of chrome and gold. Some of the components are displayed such as b) an electrical contact used to pass high-current to heat the deposition material and c) valves used to pump out the bell jar using a diffusion pump.

sputtering system (Floyd) at the Nanofab also works well with a large exposed area ($> 1 \mu\text{m}$), but it is not suited for thin layer deposition on a small area (Fig. C.3). I have successfully deposited 5 nm Cr and 15 nm Au, where Cr is the adhesion layer for Au (typically $1/3 \sim 1/4$ of the desired Au thickness). The recipe for thermal deposition is simple and easy but I have listed them for completeness. Prior to deposition, liquid nitrogen (LN_2) must be prepared in a small dewar (40 L).

• Deposition

1. The first step is to vent the chamber and mount the sample upside down. The quartz crystal should be on the same level as the sample. Cover the sample using the shutter by rotating the knob at the bottom of the chamber. The shutter can be tricky to use so practice until the shutter can be covered and opened efficiently. The desired deposition material should also be prepared on a tungsten boat, which was Cr (wire) and Au (scraps).
2. Fill the tank with LN_2 , which is located in the bottom of the diffusion pump

(metallic tube), until LN_2 comes out at the other end of the tank (latex tube). It is important to have this tank filled with LN_2 before opening the cryo-valve to trap contaminations from the diffusion pump. Also fill the rough-pump trap with LN_2 at the back, which is optional.

3. Seal the bell jar and close the foreline-valve. Then open the rough-valve, located at the back, to pump out the bell jar to 60 mTorr. The pressure gauges are displayed at the back panel where the bell jar pressure should not go lower than 50 mTorr during the roughing stage.
4. Close the rough-valve and open the foreline-valve.
5. With the foreline-valve open, it is ready to open the cryo-valve (diffusion pump). Do this step very slowly such that if the pressure starts to rise stop opening the cryo-valve and wait till the pressure drops again. After the valve is completely open, turn on the ion gauge.
6. Pump the chamber for two hours to have base pressure near 10^{-6} Torr $\sim 10^{-7}$ Torr.
7. Mechanically touch the electrical rod to the desired deposition container by rotating the rod clock-wise (Fig. C.7b). Watch the pressure and obtain a good electrical contact (it should fit nicely with the counter-sink).
8. Increase the current until a glow appears in the material and calibrate the quartz thickness monitor. Start the deposition using the shutter for desired layer thickness with low deposition rate.
9. Undo the electrical contact and rotate the material inside using the knob under the chamber to deposit other materials (repeat steps of 7 and 8).
10. Turn off procedure is the reverse-order where the ion gauge must be turned off first, then the cryo-valve is slowly closed, and the bell jar is finally vented. After taking out the deposited sample, rough the bell jar by closing the foreline-valve, and opening the rough-valve. After reaching 60 mTorr, close the rough-valve and open the foreline-valve.

After depositing a small layer of Cr and Au, an ultrasonic acetone liftoff procedure was used to remove the organic resist layer (PMMA) leaving the gold patterns on the paddles. Finally cleaning the chip with piranha solution, the device is now ready for post-processing as shown in Fig. 2.8 resulting in Fig. C.3. Note that the piranha solution does not etch Au but it slowly etches Cr, which the cleaning time was kept to a minimum (\sim ten minutes) instead of thirty minutes.

Bibliography

- [1] H. Cavendish. Experiments to determine the density of the earth. *Philosophical Transactions of the Royal Society of London*, 88(0):469–526, 1798.
- [2] G. Luther and W. Towler. Redetermination of the Newtonian gravitational constant G . *Physical Review Letters*, 48(3):121–123, 1982.
- [3] S. Schlamminger, K.Y. Choi, T. Wagner, J. Gundlach, and E. Adelberger. Test of the equivalence principle using a rotating torsion balance. *Physical Review Letters*, 100(4), 2008.
- [4] R. Beth. Mechanical detection and measurement of the angular momentum of light. *Physical Review*, 50(2):115–125, 1936.
- [5] D. Bishop and J. Reppy. Study of the superfluid transition in two-dimensional ^4He films. *Physical Review Letters*, 40(26):1727–1730, 1978.
- [6] E. Kim and M. H. W. Chan. Probable observation of a supersolid helium phase. *Nature*, 427(6971):225–227, 2004.
- [7] R. D. Biggar and J. M. Parpia. High-Q oscillator torque magnetometer. *Review of Scientific Instruments*, 69(10):3558, 1998.
- [8] D. Antonio, M. I. Dolz, and H. Pastoriza. Micromechanical magnetometer using an all-silicon nonlinear torsional resonator. *Applied Physics Letters*, 95(13):133505, 2009.
- [9] J. Condon and J. Marcus. Fermi surface of calcium by the de Haas-van Alphen effect. *Physical Review*, 134(2A):A446–A452, 1964.
- [10] C. Lupien, Brett Ellman, P. Grütter, and L. Taillefer. Piezoresistive torque magnetometry below 1 K. *Applied Physics Letters*, 74(3):451, 1999.
- [11] J. A. J. Burgess, A. E. Fraser, F. F. Sani, D. Vick, B. D. Hauer, J. P. Davis, and M. R. Freeman. Quantitative magneto-mechanical detection and control of the Barkhausen effect. *Science*, 339(6123):10511054, 2013.

- [12] M. D. Chabot, J. M. Moreland, L. Gao, S.-H. Liou, and C.W. Miller. Novel fabrication of micromechanical oscillators with nanoscale sensitivity at room temperature. *Journal of Microelectromechanical Systems*, 14(5):1118–1126, 2005.
- [13] P. A. Crowell, A. Madouri, M. Specht, G. Chaboussant, D. Mailly, and L. P. Lévy. Torsional oscillator magnetometer for high magnetic fields. *Review of Scientific Instruments*, 67(12):4161, 1996.
- [14] J. P. Davis, D. Vick, D. C. Fortin, J. A. J. Burgess, W. K. Hiebert, and M. R. Freeman. Nanotorsional resonator torque magnetometry. *Applied Physics Letters*, 96(7):072513, 2010.
- [15] M. L. Roukes and A. N. Cleland. A nanometre-scale mechanical electrometer. *Nature*, 392(6672):160–162, 1998.
- [16] G. Zolfagharkhani, A. Gaidarzhy, P. Degiovanni, S. Kettemann, P. Fulde, and P. Mohanty. Nanomechanical detection of itinerant electron spin flip. *Nature Nanotechnology*, 3(12):720–723, 2008.
- [17] H. B. Chan. Quantum mechanical actuation of microelectromechanical systems by the Casimir force. *Science*, 291(5510):1941–1944, 2001.
- [18] J. P. Davis, D. Vick, J. A. J. Burgess, D. C. Fortin, P. Li, V. Sauer, W. K. Hiebert, and M. R. Freeman. Observation of magnetic supercooling of the transition to the vortex state. *New Journal of Physics*, 12(9):093033, 2010.
- [19] X. Sun, J. Zheng, M. Poot, C. W. Wong, and H. X. Tang. Femtogram doubly clamped nanomechanical resonators embedded in a high- Q two-dimensional photonic crystal nanocavity. *Nano Letters*, 12(5):2299–2305, 2012.
- [20] M. Eichenfield, R. Camacho, J. Chan, K. J. Vahala, and O. Painter. A picogram- and nanometre-scale photonic-crystal optomechanical cavity. *Nature*, 459(7246):550–555, 2009.
- [21] S. Gröblacher, K. Hammerer, M. R. Vanner, and M. Aspelmeyer. Observation of strong coupling between a micromechanical resonator and an optical cavity field. *Nature*, 460(7256):724–727, 2009.
- [22] B. P. Abbott, R. Abbott, R. Adhikari, P. Ajith, B. Allen, G. Allen, R. S. Amin, S. B. Anderson, W. G. Anderson, M. A. Arain, and et al. LIGO: the laser interferometer gravitational-wave observatory. *Reports on Progress in Physics*, 72(7):076901, 2009.
- [23] J. Aasi, J. Abadie, B. P. Abbott, R. Abbott, T. D. Abbott, M. R. Abernathy, C. Adams, T. Adams, P. Addesso, R. X. Adhikari, and et al. Enhanced sensitivity of the LIGO

- gravitational wave detector by using squeezed states of light. *Nature Photonics*, 7(8):613–619, 2013.
- [24] J. Abadie, B. P. Abbott, R. Abbott, T. D. Abbott, M. Abernathy, C. Adams, R. Adhikari, C. Affeldt, B. Allen, G. S. Allen, and et al. A gravitational wave observatory operating beyond the quantum shot-noise limit. *Nature Physics*, 7(12):962–965, 2011.
- [25] T. Kippenberg, H. Rokhsari, T. Carmon, A. Scherer, and K. Vahala. Analysis of radiation-pressure induced mechanical oscillation of an optical microcavity. *Physical Review Letters*, 95(3), 2005.
- [26] A. Schliesser, R. Rivière, G. Anetsberger, O. Arcizet, and T. J. Kippenberg. Resolved-sideband cooling of a micromechanical oscillator. *Nature Physics*, 4(5):415–419, 2008.
- [27] A. H. Safavi-Naeini, S. Gröblacher, J. T. Hill, J. Chan, M. Aspelmeyer, and O. Painter. Squeezed light from a silicon micromechanical resonator. *Nature*, 500(7461):185–189, 2013.
- [28] A. Szorkovszky, G. A. Brawley, A. C. Doherty, and W. P. Bowen. Strong thermomechanical squeezing via weak measurement. *Physical Review Letters*, 110(18), 2013.
- [29] M. Aspelmeyer, T. J. Kippenberg, and F. Marquardt. Cavity optomechanics. arXiv:1303.0733.
- [30] M. Eichenfield, J. Chan, A. H. Safavi-Naeini, K. J. Vahala, and O. Painter. Modeling dispersive coupling and losses of localized optical and mechanical modes in optomechanical crystals. *Optics Express*, 17(22):20078, 2009.
- [31] C. Doolin, P. H. Kim, B. D. Hauer, A. J. R. MacDonald, and J. P. Davis. Multidimensional optomechanical cantilevers for high-frequency force sensing. *New Journal of Physics*, 16(3):035001, 2014.
- [32] A. G. Krause, M. Winger, T. D. Blasius, Q. Lin, and O. Painter. A high-resolution microchip optomechanical accelerometer. *Nature Photonics*, 6(11):768–772, 2012.
- [33] E. Gavartin, P. Verlot, and T. J. Kippenberg. A hybrid on-chip optomechanical transducer for ultrasensitive force measurements. *Nature Nanotechnology*, 7(8):509–514, 2012.
- [34] S. Forstner, S. Prams, J. Knittel, E. D. van Ooijen, J. D. Swaim, G. I. Harris, A. Szorkovszky, W. P. Bowen, and H. Rubinsztein-Dunlop. Cavity optomechanical magnetometer. *Physical Review Letters*, 108(12), 2012.

- [35] K. Srinivasan, H. Miao, M. T. Rakher, M. Davanço, and V. Aksyuk. Optomechanical transduction of an integrated silicon cantilever probe using a microdisk resonator. *Nano Letters*, 11(2):791–797, 2011.
- [36] P. H. Kim, C. Doolin, B. D. Hauer, A. J. R. MacDonald, M. R. Freeman, P. E. Barclay, and J. P. Davis. Nanoscale torsional optomechanics. *Applied Physics Letters*, 102(5):053102, 2013.
- [37] S. Franssila. *Introduction to Microfabrication*. John Wiley & Sons, Ltd, Wiley, 2010.
- [38] K. E. Petersen. Silicon as a mechanical material. *Proceedings of the IEEE*, 70(5):420–457, 1982.
- [39] S. K. Selvaraja. *Wafer scale fabrication technology for silicon photonic integrated circuits*. PhD thesis, Ghent University, Belgium, 2010.
- [40] A. Spott, Y. Liu, T. Baehr-Jones, R. Ilic, and M. Hochberg. Silicon waveguides and ring resonators at 5.5 μm . *Applied Physics Letters*, 97(21):213501, 2010.
- [41] X. Wang, S. Grist, J. Flueckiger, N. A. F. Jaeger, and L. Chrostowski. Silicon photonic slot waveguide Bragg gratings and resonators. *Optics Express*, 21(16):19029, 2013.
- [42] C. P. Michael, M. Borselli, T. J. Johnson, C. Chrystal, and O. Painter. An optical fiber-taper probe for wafer-scale microphotonic device characterization. *Optics Express*, 15(8):4745, 2007.
- [43] S. Gröblacher, J. T. Hill, A. H. Safavi-Naeini, J. Chan, and O. Painter. Highly efficient coupling from an optical fiber to a nanoscale silicon optomechanical cavity. *Applied Physics Letters*, 103(18):181104, 2013.
- [44] K. R. Williams and R. S. Muller. Etch rates for micromachining processing. *Journal of Microelectromechanical Systems*, 5(4):256269, 1996.
- [45] K. R. Williams, K. Gupta, and M. Wasilik. Etch rates for micromachining processing—part ii. *Journal of Microelectromechanical Systems*, 12(6):761–778, 2003.
- [46] B. A. Grigoryev, B. V. Nemzer, D. S. Kurumov, and J. V. Sengers. Surface tension of normal pentane, hexane, heptane, and octane. *International Journal of Thermophysics*, 13(3):453–464, 1992.
- [47] B. D. Hauer, P. H. Kim, C. Doolin, A. J. R. MacDonald, H. Ramp, and J. P. Davis. On-chip cavity optomechanical coupling. *EPJ Techniques and Instrumentation*, 1:4, 2014.

- [48] F. Ramiro-Manzano, N. Prtljaga, L. Pavesi, G. Pucker, and M. Ghulinyan. Thermo-optical bistability with Si nanocrystals in a whispering gallery mode resonator. *Optics Letters*, 38(18):3562, 2013.
- [49] M. Fujiwara, K. Toubaru, and S. Takeuchi. Optical transmittance degradation in tapered fibers. *Optics Express*, 19(9):8596, 2011.
- [50] J. C. Knight, G. Cheung, F. Jacques, and T. A. Birks. Phase-matched excitation of whispering-gallery-mode resonances by a fiber taper. *Optics Letters*, 22(15):1129, 1997.
- [51] M. Pollinger, D. O'Shea, F. Warken, and A. Rauschenbeutel. Ultrahigh-Q tunable whispering-gallery-mode microresonator. *Physical Review Letters*, 103(5), 2009.
- [52] D. K. Armani, T. J. Kippenberg, S. M. Spillane, and K. J. Vahala. Ultra-high-q toroid microcavity on a chip. *Nature*, 421(6926):925928, Feb 2003.
- [53] C. Grillet, C. L. C. Smith, D. Freeman, S. Madden, B. Luther-Davies, E. Magi, D. Moss, and B. Eggleton. Efficient coupling to chalcogenide glass photonic crystal waveguides via silica optical fiber nanowires. *Optics Express*, 14(3):1070, 2006.
- [54] L. Ding, P. Senellart, A. Lemaitre, S. Ducci, G. Leo, and I. Favero. GaAs micro-nanodisks probed by a looped fiber taper for optomechanics applications. *Proceedings of SPIE7712*, Nanophotonics III:771211, 2010.
- [55] B. D. Hauer, C. Doolin, K. S. D. Beach, and J. P. Davis. A general procedure for thermomechanical calibration of nano/micro-mechanical resonators. *Annals of Physics*, 339:181–207, 2013.
- [56] A. Suhel, B. D. Hauer, T. S. Biswas, K. S. D. Beach, and J. P. Davis. Dissipation mechanisms in thermomechanically driven silicon nitride nanostrings. *Applied Physics Letters*, 100(17):173111, 2012.
- [57] S. Lane, J. Chan, T. Thiessen, and A. Meldrum. Whispering gallery mode structure and refractometric sensitivity of fluorescent capillary-type sensors. *Sensors and Actuators B: Chemical*, 190:752–759, 2014.
- [58] O. Basarir, S. Bramhavar, G. Basilio-Sanchez, T. Morse, and K.L. Ekinici. Sensitive micromechanical displacement detection by scattering evanescent optical waves. *Optics Letters*, 35(11):1792, 2010.
- [59] J. Bay, S. Bouwstra, E. Laegsgaard, and O. Hansen. Micromachined AFM transducer with differential capacitive read-out. *Journal of Micromechanics and Microengineering*, 5(2):161–165, 1995.

- [60] Mo Li, H. X. Tang, and M. L. Roukes. Ultra-sensitive nems-based cantilevers for sensing, scanned probe and very high-frequency applications. *Nature Nanotechnology*, 2(2):114–120, 2007.
- [61] P. Horowitz and W. Hill. *The Art of Electronics*. Cambridge University Press, 1989.
- [62] J. Losby, J. A. J. Burgess, Z. Diao, D. C. Fortin, W. K. Hiebert, and M. R. Freeman. Thermo-mechanical sensitivity calibration of nanotorsional magnetometers. *Journal of Applied Physics*, 111(7):07D305, 2012.
- [63] I. Tittoonen, G. Breitenbach, T. Kalkbrenner, T. Müller, R. Conradt, S. Schiller, E. Steinsland, N. Blanc, and N. de Rooij. Interferometric measurements of the position of a macroscopic body: Towards observation of quantum limits. *Physical Review A*, 59(2):1038–1044, 1999.
- [64] J. J. Wortman and R. A. Evans. Young’s modulus, shear modulus, and poisson’s ratio in silicon and germanium. *Journal of Applied Physics*, 36(1):153, 1965.
- [65] M. Borselli, T.J. Johnson, and O. Painter. Beyond the Rayleigh scattering limit in high-Q silicon microdisks: theory and experiment. *Optics Express*, 13(5):1515, 2005.
- [66] A. M. Jayich, J. C. Sankey, B. M. Zwickl, C. Yang, J. D. Thompson, S. M. Girvin, A. A. Clerk, F. Marquardt, and J. G. E. Harris. Dispersive optomechanics: a membrane inside a cavity. *New Journal of Physics*, 10(9):095008, 2008.
- [67] M. Eichenfield, J. Chan, R.M. Camacho, K.J. Vahala, and O. Painter. Optomechanical crystals. *Nature*, 462(7269):78–82, 2009.
- [68] G. Bahl, M. Tomes, F. Marquardt, and T. Carmon. Observation of spontaneous Brillouin cooling. *Nature Physics*, 8(3):203207, 2012.
- [69] C. Doolin, B. D. Hauer, P. H. Kim, A. J. R. MacDonald, H. Ramp, and J. P. Davis. Nonlinear optomechanics in the stationary regime. arXiv:1402.3596.
- [70] H. Li, Y. Chen, J. Noh, S. Tadesse, and M. Li. Multichannel cavity optomechanics for all-optical amplification of radio frequency signals. *Nature Communications*, 3:1091, 2012.
- [71] S. Epstein and M. R. Paul. The stochastic dynamics of a nanobeam near an optomechanical resonator in a viscous fluid. *Journal of Applied Physics*, 114(14):144901, 2013.
- [72] V. B. Braginsky and A. B. Manukin. Ponderomotive Effects of Electromagnetic Radiation. *Soviet Physics Journal of Experimental and Theoretical Physics*, 52:986, 1967.

- [73] J. D. Teufel, T. Donner, D. Li, J. W. Harlow, M. S. Allman, K. Cicak, A. J. Sirois, J. D. Whittaker, K. W. Lehnert, and R. W. Simmonds. Sideband cooling of micromechanical motion to the quantum ground state. *Nature*, 475(7356):359–363, 2011.
- [74] R. Rivière, S. Deléglise, S. Weis, E. Gavartin, O. Arcizet, A. Schliesser, and T. J. Kippenberg. Optomechanical sideband cooling of a micromechanical oscillator close to the quantum ground state. *Physical Review A*, 83(6), 2011.
- [75] S. Cho, M. Cho, S. Shim, and Y. D. Park. Electrical field gradient pumping of parametric oscillation in a high-frequency nanoelectromechanical resonator. *Japanese Journal of Applied Physics*, 51:074003, 2012.
- [76] H. Okamoto, A. Gourgout, C. Chang, K. Onomitsu, I. Mahboob, E. Y. Chang, and H. Yamaguchi. Coherent phonon manipulation in coupled mechanical resonators. *Nature Physics*, 9(8):480–484, 2013.
- [77] M. Bass, C. DeCusatis, J. Enoch, V. Lakshminarayanan, G. Li, C. MacDonald, V. Mahajan, and E. Van Stryland. *Handbook of Optics, Third Edition Volume I: Geometrical and Physical Optics, Polarized Light, Components and Instruments(set)*. McGraw-Hill Professional, 2009.
- [78] M. Mitchell, A. C. Hryciw, and P. E. Barclay. Cavity optomechanics in gallium phosphide microdisks. arXiv:1309.6300.
- [79] R. Yang, Z. Wang, J. Lee, K. Ladhane, D. J. Young, and P. X.-L. Feng. 6H-SiC microdisk torsional resonators in a "smart-cut" technology. *Applied Physics Letters*, 104(9):091906, 2014.
- [80] C. Xiong, W. H. P. Pernice, X. Sun, C. Schuck, K. Y. Fong, and H. X. Tang. Aluminum nitride as a new material for chip-scale optomechanics and nonlinear optics. *New Journal of Physics*, 14(9):095014, 2012.
- [81] E. D. Black. An introduction to pound-drever-hall laser frequency stabilization. *American Journal of Physics*, 69(1):79, 2001.
- [82] Z. Diao, J. E. Losby, J. A. J. Burgess, V. T. K. Sauer, W. K. Hiebert, and M. R. Freeman. Stiction-free fabrication of lithographic nanostructures on resist-supported nanomechanical resonators. *Journal of Vacuum Science and Technology B*, 31(5):051805, 2013.